SCALABLE PROCESSING AND INTEGRATION OF 2D MATERIALS AND DEVICES

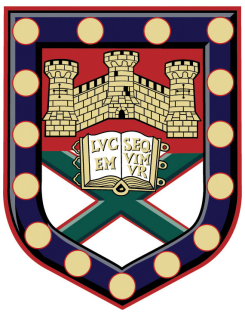

Submitted by Elías Torres Alonso to the University of Exeter as a thesis for the degree of Doctor of Philosophy in Engineering April 2018

This thesis is available for library use on the understanding that it is copyright material and that no quotation from the thesis may be published without proper acknowledgement.

I certify that all material in this thesis which is not my own work has been identified and that no material has previously submitted and approved for the award of a degree by this or any other university.

Elías Torres Alonso

Elías Torres Alonso: *Scalable processing and integration of 2D materials and devices,* Submitted by Elías Torres Alonso to the University of Exeter as a thesis for the degree of Doctor of Philosophy in Engineering, © April 2018.

ABSTRACT

Due to its truly two dimensional (2D) character and its particular lattice, single-layer graphene (SLG) possesses exceptional properties: it is semimetallic, transparent, strong yet flexible... Complementary features such as the insulating character of hexagonal boron nitride (h-BN) and semiconducting properties of transition metal dichalcogenides (TMDs) enable the whole spectrum of electronic devices to be built with combinations of these 2D materials. Due to this and the ease of exfoliation with a sticky tape, a vast amount of research was sparked. The mechanical exfoliation method, however, is only suitable for novel or proof-of-concept devices.

The trend nowadays in electronics is towards transparent, lightweight, flexible, embedded smart devices and sensors in everyday objects such as windows and mirrors, garments, windshields, car seats, parachutes...These demands are already met inherently by these new materials, thus the challenges remaining are within their synthesis, deposition and processing, where more scalable ways of production and device fabrication need to be developed.

This thesis explores innovative approaches using established techniques that aim to bridge the gap between proof-of-concept devices and real applications of 2D materials in future commercial level technologies. Methods to create graphene and engineer its properties are employed with a special focus on scalability and adaptability towards the industry. These graphene materials have been processed using pioneering schemes to create different optoelectronic devices and sensors. The techniques employed here for synthesis, transfer and deposition, device processing and characterization of graphene and derivatives, are suitable for their use in large manufacturing and mass-production. Depending on the application envisaged, different materials are used and optimize in order to balance good performance, cost-effectiveness and suitability/scalability of the process for the specific target the device was designed for.

ACKNOWLEDGEMENTS

First of all, I would like to thank my supervisors Monica and Saverio, for their confidence on me and my skills throughout all my PhD; it has been great to work alongside you. The combination of physics and engineering that you have, together with your talent and the great working atmosphere that exists within the group, have enriched me not only professionally and academically but personally.

I would like to thank all the Russo-Craciun lab present and past members. Gareth, Matt, Muk and Adolfo are, beside excellent scientists and researchers, exceptional persons who I am proud of calling friends. They taught me pretty much everything that I needed to know about graphene when I landed in the group, and they have been and unvaluable source of help and knowledge. They are capable of enjoying a conversation about physics or economy, but also of engaging with a good gig at Glastonbury, Cavern or Cellar Door, or eat some pizzas in Firehouse. It has also been a pleasure to work with Domi, Saad, Jake, Agnes, Kieran, Gopika, Shin, Janire, George, Freddie, Namphung, Ana, Mohzin, Nicola, Iddo, Connor, Liping, Peng, Selim, Dimitar, Tobby, Giannis and Konstantinos, and learned a lot of things from you guys too, and wish you all the very best.

Thanks to all the staff from physics and engineering for keep things running smoothly. Special thanks to the cleanroom manager, Mark Heath, whose countless hours of training, exceptional scientific background and even better sense of humour definitely helped me to get through the cleanroom. Special mention too to Christ Forrest for his massive patience and kind assistance when my computer just decided not to obey me. Paul, Adam and the rest of the workshop, thank you too.

I would like to thank all the teachers, from kindergarten to university, that helped me to reach this, in special Pablo, Alfredo and Restituto in high-school, and Sebastian, Kimberly and Sepideh during my time in Sweden, who gave me the opportunity do

to real nanoscience. To my music teachers, and to my sport teachers, and to my painting teachers, and to everyone I ever learned anything from; I feel very thankful from everything you have taught me.

To all the friends that have made my years in Exeter unforgettable. Lauren, Helena, Rhys, Lily, Ebba, Ed, Elliot and Scarlet, Hal, Francesca, Justin, Angus and Finn, you guys were great, letting me tag along with you in the beggining, having great dinner parties, going to Phoenix and being fun and weird my first two years. I truly feel lucky that I met you and I love you all. In my second year, Annabel, Suzie, Sam, Josh, Frasier, Kirk, Tommy D and Joe were the guys and girls to have fun with, and I enjoyed every single second with you guys. To Ada, Alfonso, Clara, Elena, Ziggy, Virginia and Valentina, the lodge fellas Pippo, Tommy, Emra and Giovanni who threw the best parties, and Lele and Gonzalo for continuing their legacy. I love you. To my housemate Eden, whose dj lessons are much appreciated and laughs have been vital this last year, I'm gonna miss you pal; to my b2b bro Louie and to my neighbours Greta, Ollie, Ollie, Mathilde, Martin, Emily, Jessica and Jake, where best pres and memories have been made (unforgettable snow fight!). I love you. My favourite islander Lucas and his great housemates Oli, Phoebe and Arianne, dinner parties and pres at yours where absolutely phenomenal. I love you guys. To the guys at the 82 and the cool boys and gurlz Johnny, Robbie, Lucy Luz, Joe, Ralph, Calum, Shawn, George, Julian, Chloe and Rachel, I am blessed to have met you all and to have exchanged opinions, music (Mount Kimbie yooo) and laughs with all of you. I love you guys too. To Isaac, Ollie, Robin, Adam, Ana and Julia, for some good laughs. To Santi, Joaquin and Carlota for the laughs in the cleanroom. To the french gang Cesar, Margaux and Allegra. To Tess, for making me want to excel and for this last year with you.

To all the friends I met in Sweden too: Andreas, Tommy, Olivier, Heather, Matias, Cris, Shun and the architecture boys, Erin, Pablo, Lluc, Elisa, Marc, Julia, Aniol, Laura, Eduardo, Lachie and Jimbo, Vee, Karen, Jeff... To Josje, for all the amazing days we spent together.

To my brothers Alvaro and Borja, and for all the support and laughs from Bermejo, Comino, Luismi, Alex, Aitor, Juan, Carmen, Rixi, Laura, Erenxu, Mario, Chui, Dani P, Juan's sisters and Kay. To my Madrid brothers Mare, Jaco, Alberto, Benito, Jimmy y Gallego. To my fellow physicists (and a lawyer) Miguel, Ade, Jacobo, Isa, Armesto, Llamas, Felix, Arrieta, Brother, Kacper and JM. To my band-mates Griffon and Yuyu.

To Ines, for the time we shared.

Finally, to my parents Miguel and Tita, whose love and unconditional support have been crucial throughout all my life: I could not have made it without you. You are my example. I love you. And to my family Mari, Luis, Pela, Lourdes, Laura, Manu, Rafa, Pelayo, Elena y Daniela. To my beloved Titi and Deme. I love you all.

And to everyone I crossed paths with that helped me to be where and who I am. Thank you very much.

CONTENTS

Publications 111

LIST OF FIGURES

ACRONYMS

2D two dimensional.

ACEL alternating-current electroluminescence.

AFM atomic force microscopy.

$AuCl_3$ gold chloride (III).

$BaTiO_3$ barium titanate.

BEPL back-end production line.

BLG bilayer graphene.

CMOS complementary metal oxide semiconductor.

CNT carbon nanotubes.

CVD chemical vapour deposition.

DIW de-ionised water.

DOS density of states.

E_F Fermi energy.

$FeCl_3$ iron chloride (III).

$FeCl_3$-FLG iron-chloride intercalated few-layer graphene.

FET field-effect transistor.

FLG few-layer graphene.

FWHM full-width half maximum.

GO graphene oxide.

h-BN hexagonal boron nitride.

IPA isopropanol.

ITO indium tin oxide.

LED light-emitting diode.

LEG liquid-exfoliated graphene.

LPE liquid-phase exfoliation.

MFC mass-flow controller.

NaC sodium cholate.

NMP n-methyl-2-pyrrolidone.

NW nanowires.

OL optical lithography.

OLED organic light-emitting diodes.

PC polycarbonate.

PDMS polydimethylsiloxane.

PEDOT:PSS poly(3,4-ethylenedioxythiophene) polystyrenesulfonate.

PEN polyethylene naphthalate.

PET polyethylene terephthalate.

PMGI polymethylglutaramide.

PMMA poly(methyl methacrylate).

PP polypropylene.

PR photoresist.

PS polystyrene.

PTFE polytetrafluoroethylene.

PV photovoltaics.

r-GO reduced graphene oxide.

R_s sheet resistance.

R2R roll-to-roll.

RF radio-frequency.

RH relative humidity.

RIE reactive ion etching.
RMS root mean square.
SEM scanning electron microscope.
SiO_2 silicon dioxide.
SLG single-layer graphene.
TCF transparent conductive film.
TLG trilayer graphene.
TMAH tetramethyl-ammonium hidroxide.
TMDs transition metal dichalcogenides.
ZnS zinc sulphide.
ZnS:Cu copper-doped zinc sulphide.

1

INTRODUCTION

Graphene, a single atom thick layer of carbon atoms arranged in a honeycomb fashion, has been often referred as the material of superlatives, given its exceptional properties: high transparency, high conductivity and high flexibility just to name a few.[1;2;3;4] The possibility of using not only pristine graphene but functionalised-graphene materials and the ease of exfoliation with a simple sticky tape triggered much research in the field.[5;6] These factors have produced an exponential increase in graphene publications from its first report in 2004.[7]

Nevertheless, graphene is only the first of many two dimensional (2D) materials that have been discovered in the last 10 years. Complementary features such as the insulating character of hexagonal boron nitride (h-BN) and semiconducting properties of transition metal dichalcogenides (TMDs) enable the whole spectrum of electronic devices to be built with combination of these 2D materials, from basic field-effect transistor (FET) to p-n junctions and quantum well structures.[8;9;10;11;12;13;14] Moreover, the truly bi-dimensional character of the materials gives rise to new physical phenomena, that could be seized to produce novel and unforeseen device concepts and technologies that were simply unimaginable a few years ago, such as 10-atom-thick light-emitting diodes, chiral light-emitting transistors or even the possibility of establishing graphene as the new standard for resistivity metrology.[14;15;16;17]

Remarkably, their planar nature made the techniques employed in the ubiquitous complementary metal oxide semiconductor (CMOS) processing readily available for these novel materials.[18;19] Moreover, being as close to the end of Moore's Law as we are, these novel 2D materials represent a new paradigm within the semiconductor technology, capable of further miniaturization down to truly nanometre-sized devices,

which Si CMOS technology would not be capable of due to short-channel effects and processing constrains.[20;21] An introduction to graphene, to some functionalised forms of graphene and their physical properties most relevant to this thesis is done in Chapter 2.

The current industry demands of transparency, good conductivity and flexibility are already met inherently by these new materials, thus the remaining challenges are their synthesis, deposition and processing; scalable ways of production and device fabrication have been developed, but may not be adapted to the industry requirements.[7;22;23;24] Despite producing the highest quality of graphene possible, mechanical exfoliation could not satisfy the volume of demand and automation that is needed currently.

However, advances in material synthesis by chemical vapour deposition (CVD), liquid-phase exfoliation (LPE), and transfer to arbitrary substrates, have opened up ways for these materials to be introduced into the semiconductor processing workflows and emerging roll-to-roll (R2R) schemes.[25;26;27] They can provide much larger areas with acceptable homogeneity and electronic properties (comparable to those of mechanically exfoliated samples) in the case of CVD, and high scalability and low-cost in the case of LPE. The successful transfer to arbitrary substrates, such as polyethylene terephthalate (PET) and polyethylene naphthalate (PEN), which are fully flexible and highly transparent, expanded its range of uses, specially within the optoelectronics and printed electronics field;[28;29] new paths have been opened too with the inclusion of graphene in wearable technologies.[22;30;31] In conclusion, now a wide range of properties can be met by these different ways of graphene synthesis, transfer and processing methods. These methods are introduced in Chapter 2, whereas the actual techniques used in this thesis will be explained in Chapter 3.

This thesis has investigated scalable techniques and approaches to produce and fabricate 2D materials and devices towards potential commercial applications. Methods to create graphene and engineer its properties are employed, with a special focus on adaptability to the industry, which has strict demands and standards. For instance, while graphene possesses very high electronic mobility, resulting in high conductivity (for a single-atom thick material), this conductivity is still not sufficient for large-area transparent electrodes in flexible display applications; they would suffer from inhomogeneous brightness due to the voltage drop across the electrode.[32]

To overcome this problem, CVD-grown few-layer graphene (FLG) was function-

alised through intercalation with $FeCl_3$. This process dramatically reduces the resistance of the material via p-doping with minimal change in its transparency. This allows to build much larger optoelectronic devices if it is used as transparent conductive film (TCF).[33;34] The performance of these electrodes was tested by making alternating-current electroluminescence (ACEL) devices with iron-chloride intercalated few-layer graphene ($FeCl_3$-FLG) electrodes for the first time; ACEL is a very mature technology for illumination which renders flexible and large area screens. I demonstrate that using this material, much larger sizes and with more homogeneous illumination ACEL devices can be made, whilst retaining its extreme flexibility and foldability.[34;35;36] This is shown in Chapter 4.

Building upon this work, I also incorporated CVD-grown FLG as transparent electrodes into polymeric textile fibres, and by combining them with ACEL materials, flexible light-emitting devices embedded in such fibres were created for the first time. Despite that a few light-emitting devices have been created before with wearable purpose, they all lack some of the needs that the industry demands;[22] the use of graphene allows for a combination of electrical and mechanical properties in such devices that present interesting characteristics for textile electronics, where light-emitting devices will represent a key element in both leisure and sponsored clothing, automobile applications, military garments...[22;37;38;39] Their properties were extensively analysed, and different arrays and architectures were employed to show their potential for consumer applications. These results are shown in Chapter 5.

These graphene-based conductive textiles also allowed me to pioneer touch-sensors embedded in these fibres. Touch-sensing is used in many electronic devices as an interface between the user and the device itself; importantly, most of the applications in consumer electronics require high transparency, since usually the sensors are embedded within displays and the screens.[40] Furthermore, to fulfil the requirements of the textiles industry market, these devices will need to be flexible and durable, adaptable to body shapes, capable of being woven or knitted and their processing needs to be compatible with the organic and polymeric materials employed as substrates.[22] However, the current touch-sensing technology does not allow for all these features to be present simultaneously.[41;42;43;44] The devices presented in this thesis here take advantage of the inherent transparency, conductivity and flexibility of graphene to create woven touch sensors; they span from single fibre finger- and glove-like devices to fully transparent

and foldable sensing fibre arrays with spatial resolution. Moreover, we used different types of graphene (CVD and LPE) to demonstrate that properties such as conductivity and transparency can be tailored to match the desired specifications. These results are shown in Chapter 6.

So far the attention has been focused specially on devices where a graphene of the highest quality is necessary. These are applications where excellent conductivity and transparency are required, and CVD-grown graphene is still the best option for such purposes. Nevertheless, there are applications where high conductivity is not crucial, transparency may or not be of importance and where in general, a high-quality graphene is not needed. Furthermore, it might be even beneficial to introduce defects or dangling bonds; this is of special relevance in sensing and energy-storage purposes.[45;46;47;48] For these purposes, LPE materials are of great interest, due to the large scalability of their production, their great cost-effectiveness and advances on the material synthesis and deposition. Also, almost the whole range of 2D materials can be dispersed and prepared in different solvents.[49;50;51] These will be the materials which will have the most immediate applications in for instance composites, with products already in the shops such as graphene incorporated in tennis rackets.[52;53;54] Using liquid-exfoliated graphene (LEG), I developed a novel process to create well-defined patterns over an ultra-large area, and combined LEG and graphene oxide (GO) films to create all-carbon humidity sensors for the first time. These sensors were created with only LPE of 2D materials, on both a 4' Si wafer and PET substrates, with a workflow compatible with those in the established CMOS and the emerging R2R processing. These findings are reported in Chapter 7.

BIBLIOGRAPHY

[1] A. K. Geim et al. The rise of graphene. *Nature Materials*, 6, 2007.

[2] A. H. Castro Neto et al. The electronic properties of graphene. *Review Modern Physics*, 81, 2009.

[3] C. Lee et al. Measurement of the elastic properties and intrinsic strength of monolayer graphene. *Science*, 321, 2008.

[4] R. R. Nair et al. Fine structure constant defines visual transparency of graphene. *Science*, 320, 2008.

[5] K. S. Novoselov et al. Electric field effect in atomically thin carbon films. *Science*, 306, 2004.

[6] M. F. Craciun et al. Properties and applications of chemically functionalized graphene. *Journal of Physics: Condensed Matter*, 25, 2013.

[7] E. P. D. Randviir et al. A decade of graphene research: production, applications and outlook. *Materials Today*, 17, 2014.

[8] C. R. Dean et al. Boron nitride substrates for high-quality graphene electronics. *Nature Nanotechnology*, 5, 2010.

[9] K. Watanabe et al. Direct-bandgap properties and evidence for ultraviolet lasing of hexagonal boron nitride single crystal. *Nature Materials*, 3, 2004.

[10] A. Pospischil et al. Optoelectronic devices based on atomically thin transition metal dichalcogenides. *Applied Sciences*, 6, 2016.

[11] Q. H. Wang et al. Electronics and optoelectronics of two-dimensional transition metal dichalcogenides. *Nature Nanotechnology*, 7, 2012.

[12] Z. Fei et al. Gate-tuning of graphene plasmons revealed by infrared nano-imaging. *Nature*, 487, 2012.

[13] C. O. Kim et al. *Nature Communications*, 5, 2014.

[14] F. Withers et al. Light-emitting diodes by band-structure engineering in van der waals heterostructures. *Nature Materials*, 14, 2015.

[15] F. Lafont et al. Quantum hall resistance standards from graphene grown by chemical vapour deposition on silicon carbide. *Nature Communications*, 6, 2015.

[16] Y. J. Zhang et al. Electrically switchable chiral light-emitting transistor. *Science*, 344, 2014.

[17] C-H. Liu et al. Graphene photodetectors with ultra-broadband and high responsivity at room temperature. *Nature Nanotechnology*, 9, 2014.

[18] S. Goossens et al. Broadband image sensor array based on graphene-cmos integration. *Nature Photonics*, 11, 2017.

[19] C. Chuantong et al. Monolithic optoelectronic integrated broadband optical receiver with graphene photodetectors. *Nanophotonics*, 6, 2017.

[20] Y. Taur. CMOS design near the limit of scaling. *IBM Journal of Research and Development*, 46, 2002.

[21] S. B. Desai et al. MoS_2 transistors with 1-nanometer gate lengths. 354, 2016.

[22] A. K. Yetisen et al. Nanotechnology in textiles. *ACS Nano*, 10, 2016.

[23] A. K. Geim. Graphene: Status and prospects. *Science*, 324, 2009.

[24] F. Bonaccorso et al. Production and processing of graphene and 2d crystals. *Materials Today*, 15, 2012.

[25] K. E. Whitener et al. Graphene synthesis. *Diamond and Related Materials*, 46, 2014.

[26] Y. Hernandez et al. High-yield production of graphene by liquid-phase exfoliation of graphite. *Nature Nanotechnology*, 3, 2008.

[27] S. Bae et al. Roll-to-roll production of 30-inch graphene films for transparent electrodes. *Nature Nanotechnology*, 5, 2010.

[28] F. H. L. Koppens et al. Photodetectors based on graphene, other two-dimensional materials and hybrid systems. *Nature Nanotechnology*, 9, 2014.

[29] F. Torrisi et al. Inkjet-printed graphene electronics. *ACS Nano*, 6, 2012.

[30] A. I. S. Neves et al. Transparent conductive graphene textile fibers. *Scientific Reports*, 5, 2015.

[31] N. Karim et al. All inkjet-printed graphene-based conductive patterns for wearable e-textile applications. *J. Mater. Chem. C*, 5, 2017.

[32] T.H. Bointon et al. Is graphene a good transparent electrode for photovoltaics and display applications? *IET Circuits Devices and Systems*, 9, 2015.

[33] I. Khrapach et al. Novel highly conductive and transparent graphene-based conductors. *Advanced Materials*, 24, 2012.

[34] E. Torres Alonso et al. Homogeneously bright, flexible, and foldable lighting devices with functionalized graphene electrodes. *ACS Applied Materials & Interfaces*, 8, 2016.

[35] T. H. Bointon et al. Large-area functionalized CVD graphene for work function matched transparent electrodes. *Scientific Reports*, 5, 2015.

[36] D. J. Wehenkel et al. Unforeseen high temperature and humidity stability of $FeCl_3$ intercalated few layer graphene. *Scientific Reports*, 5, 2015.

[37] H. Yang et al. Light-emitting coaxial nanofibers. *ACS Nano*, 6, 2012.

[38] S. Choi et al. Highly flexible and efficient fabric-based organic light-emitting devices for clothing-shaped wearable displays. *Scientific Reports*, 7, 2017.

[39] K. Cherenack et al. Woven electronic fibers with sensing and display functions for smart textiles. *Advanced Materials*, 22, 2014.

[40] G. Barrett et al. Projected-capacitive touch technology. *SID Information Display*, 2010.

[41] H. Tian et al. A graphene-based resistive pressure sensor with record-high sensitivity in a wide pressure range. *Scientific Reports*, 5, 2015.

[42] Y. A. l. Samad et al. Novel graphene foam composite with adjustable sensitivity for sensor applications. *ACS Applied Materials & Interfaces*, 7, 2015.

[43] S-E. Zhu et al. Graphene based piezoresistive pressure sensor. *Applied Physics Letters*, 102, 2013.

[44] C. Hou et al. Highly conductive, flexible, and compressible all-graphene passive electronic skin for sensing human touch. *Advanced Materials*, 26, 2014.

[45] B. Sanyal et al. Molecular adsorption in graphene with divacancy defects. *Physical Review B*, 79, 2009.

[46] Y. Hajati et al. Improved gas sensing activity in structurally defected bilayer graphene. *Nanotechnology*, 23, 2012.

[47] B. Kumar et al. The role of external defects in chemical sensing of graphene field-effect transistors. *Nano Letters*, 13, 2013.

[48] W. Yuan et al. The edge- and basal-plane-specific electrochemistry of a single-layer graphene sheet. *Scientific Reports*, 3, 2013.

[49] J. N. Coleman et al. Two-dimensional nanosheets produced by liquid exfoliation of layered materials. *Science*, 331, 2011.

[50] V. Nicolosi et al. Liquid exfoliation of layered materials. *Science*, 340, 2013.

[51] K. R. Paton et al. Scalable production of large quantities of defect-free few-layer graphene by shear exfoliation in liquids. *Nature Materials*, 13, 2014.

[52] Head. Graphene XT.

[53] S. Stankovich et al. Graphene-based composite materials. *Nature*, 442, 2006.

[54] X. Qi et al. Amphiphilic graphene composites. *Angewandte Chemie International Edition*, 49, 2010.

2

THEORETICAL BACKGROUND

2.1 SCOPE

Graphene, still a novel material that is not even 15 years old, attracted great interest from the very beginning and has been a subject of intense research since then. While the particular electronic properties of graphite were well known as early as 1947, a single layer of graphite (coined graphene) was itself thought to be impossible to occur in nature due to thermal fluctuations.[1;2]. The pioneering experiments carried out at Manchester demonstrated otherwise, mechanically exfoliating graphite to produce stable graphene, opening the door to a new field of research in physics, chemistry and materials science.[3] The scope of this chapter is to review some of the theoretical concepts of graphene, with a focus on the properties and characteristics that are key for the understanding of the results presented in the following chapters.

Graphene´s characteristic band structure will be shown and briefly discussed, since it is the origin of many of graphene´s remarkable electronic and optoelectronic properties. The exceptional mechanical properties of graphene will also be reviewed. Attention will turn then onto the experimental techniques related to graphene´s production, doping and characterization. Firstly, methods to create graphene, focusing on methods of large-area and/or with high yields and scalability for mass-production are presented. Functional materials used along the thesis, such as graphene oxide (GO) and iron-chloride intercalated few-layer graphene ($FeCl_3$-FLG), are also introduced. Throughout this section, graphene will be considered as single-layer graphene (SLG) unless indicated otherwise.

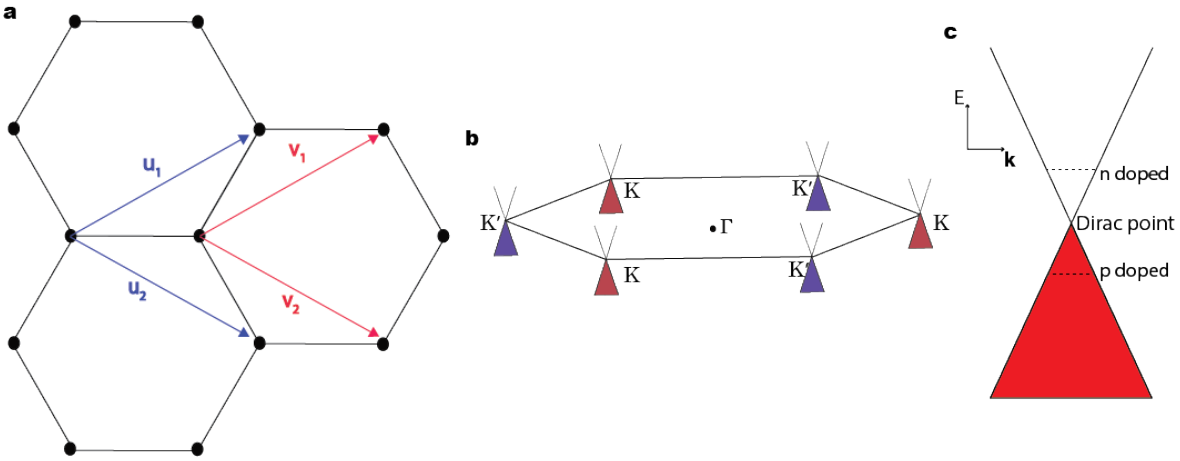

Figure 2.1: a) Lattice of graphene, showing its hexagonal lattice with two base vectors. b) Sketch of the first Brillouin Zone. c) Sketch of the band structure of graphene at the vecinity of the Dirac point.

2.2 GRAPHENE LATTICE AND BAND-STRUCTURE

Graphene's lattice consists of a double two-carbon-atom base, which resembles a honeycomb structure (see Figure 2.1a). The truly-two dimensional nature of the material renders a particular electronic band structure, which is modeled using the tight-binding formalism; usually a nearest-neighbours approach is enough to obtain good results. [3;4;5;6]

In the low-energy regime, the Brillouin zone has 6 points where conduction and valence band meet (see the Figure 2.1b), the so-called Dirac point; above (below) the Dirac point, electrons (holes) are the charge carriers. There are two sets of 3 K and K' valleys (due to the two sublattices) around the Dirac points where the band-structure forms a cone, with a linear dispersion with wavenumber: $E = \hbar v_F |k|$, where $\hbar$ is the reduced Planck constant, v_F is the Fermi velocity and $|k|$ is the modulus of the wavenumber vector, as shown in Figure 2.1c. [4] This resembles the photon dispersion, $E = c|p|$, where c is the speed of light and $|p|$ is the modulus of the linear momentum.

This makes graphene a gapless semiconductor or semi-metal (see again the Figure 2.1c), and has one main advantage and one main drawback: it makes graphene capable of absorbing virtually any wavelength but also turns it useless for logic applications in electronics due to its lack of bandgap and thus the impossibility of being switched off. [7;8] This lack of band-gap is a consequence of the equivalence between the energy of the

graphene sublattices; breaking this symmetry through hydrogenation and fluorination for instance has been accomplished and insulating and luminescent properties have been achieved, but their applicability is still very limited due to inestability of the materials and difficulty for process scaling. However, GO presents stable properties and luminescence and band-gap opening have been achieved.[9;10;11] A perpendicular electric field in bilayer graphene (BLG) opens up a band-gap which is gate-tunable;[12] creating graphene nanoribbons breaks the translational symmetry, allowing for band-gap opening in the range of few meV.[13;14]

The density of states (DOS) of graphene, unlike other well-known two-dimensional electron gases in Si, GaAs and so forth, is linearly proportional to Fermi energy (E_F) and is zero at the Dirac point. Its charge density is usually in the range of $n = 10^{11} - 10^{12}\ cm^{-2}$ for undoped SLG. This low charge density can be continuosly tuned through electrostatic gating in a straightforward way, enabling quantum transport and optoelectronic response in different charge density regimes.[3;4;5]. Indeed, electrons in graphene behave as if they were massless even though they are not; they do have a small collective effective mass (m^*).[15;4;3]

2.3 RELEVANT PROPERTIES

2.3.1 *Transport properties*

There are a few features, related with the lattice and band-structure of graphene, behind the exceptional electron transport characteristics of graphene. First one is the absence of back-scattering: certain angles of incidence with respect a potential barrier would produce no scattering at all and perfect tunneling or Klein tunneling.[4] Another important property is the massless behaviour of their carriers, which turns in high v_F of $10^6\ ms^{-1}$.[4] These properties make graphene a material with very high mobilities ($\mu \propto 1/m^*$, where μ is the mobility and m^* is the effective mass). The high mobility is one of the main advantages of not only graphene but other two dimensional (2D) materials, especially in flexible electronics, where usually organic materials are used but their low-mobilities limit their uses for displays or touch-sensors.[4;16;17] Applications such as high-speed radio-frequency (RF) transistors (where no band-gap is needed) and ultra-fast optoelectronics would also benefit from high mobilities, allowing signals to be rapidly transmitted.[7;8]

These mobilities are highly dependent on scattering events: adatoms in the surface, ripples and wrinkles and substrate impurities can all behave as scattering sources.[4;18] The substrate on which graphene is deposited has a significantly influence its transport properties. In silicon dioxide (SiO_2), dangling bonds interact with graphene´s electrons resulting in mobilities in the range of 1000s cm^2/Vs,[3] which are still one order of magnitude better than conventional Si devices. However, hexagonal boron nitride (h-BN)-encapsulated graphene devices have reported mobilities over 200000 cm^2/Vs; this is translated into very large mean free paths, enabling truly ballistic devices to be built even in the millimeter scale.

Despite such high mobilities, the conductivity ($\sigma = ne\mu$) is still not very high, resulting in sheet resistance (R_s) of 1 kΩ/sq for SLG. This is due to the small carrier concentration of graphene because of its reduced dimensionality. For this, electron scattering must be minimised and more importantly, carrier concentration increased to meet certain specifications, especially regarding transparent conductive film (TCF)s.[18;19].

A way to increase carrier concentration is to increase the number of layers. The charge density in graphene is augmented with the number of layers; this can vary easily an order of magnitude from SLG to few-layer graphene (FLG). This however would reduce transparency.

Another option to achieve a higher carrier concentration in graphene, but without sacrificing transparency, is to dope it. Doping in graphene has been achieved by two methods: electrostatic gating, which is not permament so of very limited applicability in real life applications; the other way is chemical doping, which can be realised through exposure to iron chloride (III) ($FeCl_3$), ammonia plasma, gold chloride (III) ($AuCl_3$) and several other compounds, some of which are stable.[20] These compounds attach to or intercalate in between the graphene layers; this interaction produces a charge transfer that increases the net carrier density.

To conclude, due to the reduced dimensionality of graphene, it has truly 2D transport properties. The resistance R of a material is defined by $R = \rho\frac{l}{wt}$, where R is the total resistance of the material given by the resistivity ρ, the length l, the width w and thickness t. However, the thickness of graphene and other 2D materials can be that of a single atom; so it is more convenient to define resistance in terms of R_s as $R = \frac{\rho l}{wt} = R_s\frac{l}{w}$. Then $R_s = \frac{\rho}{t}$ has units of Ohms because it is multiplied by a dimensionless quantity, although usually R_s is expressed as Ohms/square (Ω/sq); this

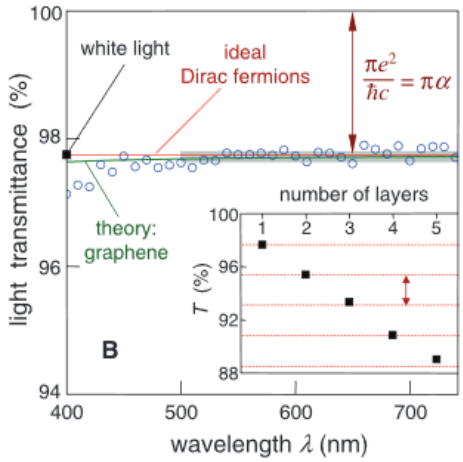

Figure 2.2: Transmittance vs wavelenght for graphene. The inset shows transmittance for different number of graphene layers. Adapted with permission from [27].

is interpreted as the resistance to any current passing from side to side of a square of the material.

2.3.2 *Optical properties*

As a potential substitute for indium tin oxide (ITO), poly(3,4-ethylenedioxythiophene) polystyrenesulfonate (PEDOT:PSS) or metallic nanowires (NW) as TCF, transparency is of major importance in addition to conductivity. An important feature of the two-dimensional massless electrons is their strong light absorption, consequence of the strong light-matter interactions in graphene: for a single-atom-thick material as graphene, 2.3% of adsorption is very large. However, for uses such as TCF this transparency is excellent. Such high transparency would make it almost invisible to the naked eyed, or by using the microscope; interference effects with SiO_2 and Si are then needed to make graphene visible through optical contrast measuremens. Usually graphene is deposited on 300 nm or 90 nm thick SiO_2/Si chips, which maximise graphene contrast.[8;21;22]

As previously mentioned before, the gapless band-structure of graphene means that light absorbed generates carriers over a very wide energy spectrum; this spans from near-infrared to terahertz regimes. This property is unmatched by any other material.[8;23] Remarkably, this light absorption relationship is universal and it is quantised

and given by $T \sim 1 - \pi\alpha \sim 97.7\%$, where α is the fine structure constant and T is the transmittance.[24] Therefore,the absorption for SLG is 2.3 %, BLG is 4.6%, trilayer graphene (TLG) is 6.9% and so on.

This light absorption is flat along a wide range of wavelengths including the visible, as seen in Figure 2.2, which is of much advantage for optoelectronic devices.[8;24] Usually, TCF such as PEDOT:PSS do not present such flatness in their transmittance, and metallic NW present peaks and valleys in their absorption spectra due to plasmon excitations, and haze due to different agglomeration densities, which makes achieving homogeneous transparency and requires of complex power feedback loops to produce homogeneity.[25]

As pointed out in the previos section, the trade-off is clear: an increase in the number of layers would increase conductivity but reduce transparency. For example, chemical vapour deposition (CVD)-grown FLG has a R_s in the order of a few 100s Ω/sq at ∼80% transparency (T) and CVD-grown SLG is at $T = 97.7$ % for a R_s of ∼1000 Ω/sq in the best samples without substrate engineering.[19;26;27] However this is still far away from the ITO standard for rigid optoelectronics (∼10s of Ω/sq for ∼80% transparency for most common devices), although it is acceptable for the current flexible electronic market where device technology has not matured enough to produce very large-area displays (in part due to the lack of a better flexible TCF).[19]

After light is adsorbed through excitation of an electron-hole pair, hot carrier (hot here means above the E_F) relaxation or cooling in graphene is done by phonon-mediated lattice interactions (which are very inefficient in graphene) in the range of 100 fs, and electron-electron scattering events where hot electrons would scatter with another electron (secondary hot electrons), in the ps range.[28;29;18] This quenched phonon cooling enhances the chances for these hot electrons to be collected, improving photodetection or photovoltaics (PV) efficiency.[29].

In terms of light emission, pristine graphene does not produce excitonic luminescence due to its lack of band-gap. However this band-gap can be engineered breaking the lattice symmetry, and bandgaps in the meV range can be tuned with nanoribbon width (which breaks translational symmetry) as cited previously.[30] Luminescence can be achieved through funcionalisation too, as GO possesses strong excitonic luminescence (with applications in biology), or defect creation through mild O_2 plasmas which act as recombination centers.[31;32;33].

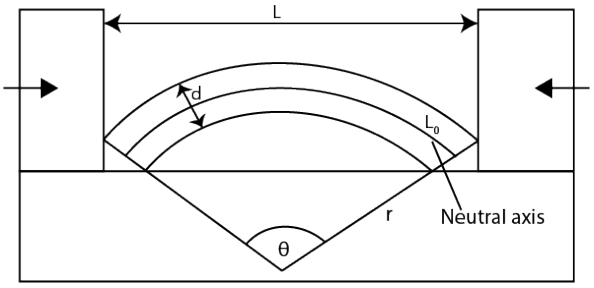

Figure 2.3: Diagram showing a device under strain. The inner side would undergo compression and and the outer side would undergo elongation.

Interestingly, given graphene's exceptional mechanical strength and high-temperature stability, one can achieve visible thermal radiation in suspended graphene devices, with 1000-fold enhancement in thermal radiation efficiency compared with other thermal sources.[34] In addition, through interference effects with the substrate, one can tune the emitted wavelenght, creating ultra-small on-chip light sources.[34;22]

2.3.3 *Mechanical properties*

One of the main attributes of graphene is its great flexibility, which is a very important feature especially regarding opto- and electronic devices requiring flexible TCF. In real life applications, bending rather than stretching will be the most common source of strain. This strain caused by flexural bending (ϵ) decreases linearly on the surface of a material with the substrate thickness. If a material of thickness d and length $L_0 = r\theta$ in the neutral axis is strained as shown in Figure 2.3 down to a length L, the strain is given by $\epsilon = z - 2d/2r$, where z is the distance of the surface from the neutral axis of the substrate and r is the bending radius.[35;36]

This is the reason why some materials (even metals) are flexible when deposited as thin-films, whereas their bulk counterparts are not (as it is the case of graphene and graphite too): because the strain is proportional to the thickness of the material. So the device flexibility is limited by the intrinsic material strength and device thickness and geometry. Additionaly, the single-atom nature of graphene may be highly relevant when the device thickness is optimised to minimise the distance from the neutral axis, in order to reduce strains in the device.[17]

The breaking strength of a material is the maximum stress that can be supported

by the material prior to failure in a pristine material without defects. Due to the high crystalinity of graphene, this breaking strength has the large value of 42 Nm^{-1}, where steel has an average value of 0.04 Nm^{-2}.[37;38] The Young modulus of graphene (the strain induced due to a certain stress) is 1 TPa, which makes it the stiffest material ever known, and it is capable of sustain strains up to 8 %. These values however are for pristine, high-quality exfoliated graphene flakes; they are expected to be lower for CVD graphene due to existence of grain boundaries and defects which would weaken the structure.[38]

The physical origin of these outstanding mechanical properties is the strong in-plane σ bonds resulting from the sp^2 hybridisation of the s, p_x and p_y orbitals; the remaining out-of-plane p_z orbitals form weaker π bonds which determine the electronic behaviour. Due to this weak out-of-plane interaction (graphite layers remain together due to van der Waals forces), graphite exfoliation is achievable with simple sticky tape.[4] On the other hand, the strong σ covalent bond in graphene's lattice prevents any chemical wet-etching, so usually O_2 or Ar reactive ion etching (RIE) are used for pattern transfer.[38;17]

2.4 METHODS OF LARGE AREA PRODUCTION

The mechanical exfoliation of graphite provides a reliable method to obtain high-quality single-crystaline micron-sized graphene.[3] However, this method is not scalable for the necessary large areas and high yields that current workflows in the semiconductor industry need.

Not only at a research level but also in modern semiconductor processing, CVD is an ubiquitous technique for the growth of high-quality materials. The electronic characteristics of CVD-grown graphene samples are now, after extensive study, comparable to those obtained by mechanical cleavage.[39] This, together with the encapsulation of graphene with h-BN and contact engineering, are behind the exceptional electron mobilities shown in graphene field-effect transistor (FET)s which would allow for ultra-fast electronics.[40]

Furthermore, CVD is a technique compatible with roll-to-roll (R2R) processes. R2R allows for the continuous production/deposition/processing of a flexible material; the original material is rolled and re-reeled in another roll after the desired treatment is

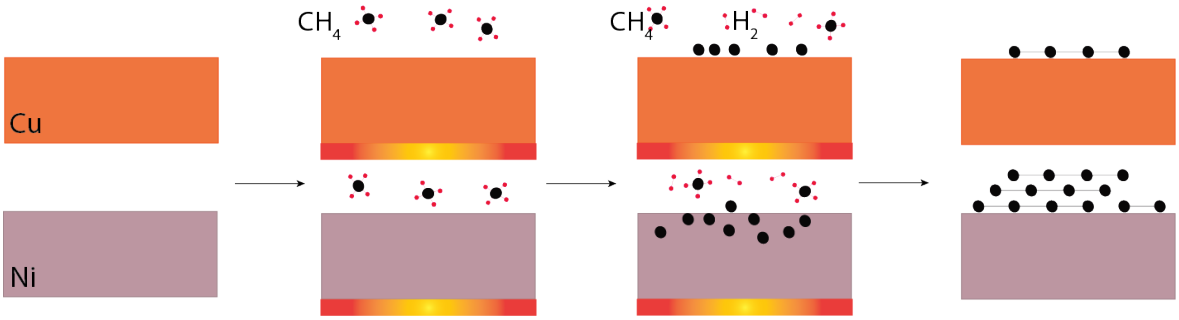

Figure 2.4: Stages in a graphene CVD process. Two different processes, Cu- (for SLG growth) or Ni- (for FLG growth) assisted, are shown.

carried out. Despite it limits the applicability of certain processes (vacuum deposition, high temperatures), this high and continuous throughput has a dramatic impact in the cost of production, which is dramatically reduced. This approach is being increasingly established within thin-film devices and solar cells. There have been examples already of CVD growth of graphene by R2R and nanoimprint lithography that employ this technique; this makes R2R the most likely process to be adopted for production and processing of flexible electronics using 2D materials.

Nevertheless, many applications do not need such quality or large-area. The introduction of graphene to polymers and matrices for different composite applications benefits from superior strength, as well as improved thermal and electronic conductivities.[41;42;32]

Due to this, liquid-exfoliated graphene (LEG) has become the most suitable method to produce SLG and FLG in a large-scale with acceptable qualities and yields.[43;44;45] Moreover, a whole range of 2D materials may now be exfoliated by this method, and together with the recent advances regarding quality and the possibility of creating thin-films by vacuum filtering or even ink-jet printing, they make these 2D solutions of great interest for a plethora of applications.[46;47]

2.4.1 *CVD*

The process of CVD is a well-known technique widely employed not only in research but in semiconductor foundries. The process was developed for graphene around 2008.[26;48] The summarised process, as seen in Figure 2.4, is the following: a substrate is heated

up, a molecule with carbon atoms is introduced into the chamber (carbon precursor), the substrate catalyzes the decomposition of the molecules, carbon is adsorbed on the surface forming graphene and remaining volatile compounds are pumped out, the furnace is then cooled down and growth is finished.

Graphene can be grown at both low-pressure (∼10 mTorr) and atmospheric pressure. It may be grown on many metals; however, the preferred ones are Cu and Ni. Cu is preferred for SLG growth: C solubility in Cu is very low, so it is mainly a surface mediated reaction, rendering SLG with coverages of ∼98% over large areas.[49] This process is also self-limiting: when all the Cu substrate is covered with graphene, growth is stopped. On the other hand, C atoms have a much higher solubility in Ni, which facilitates C diffusion within Ni; upon fast cooling/quenching, these C atoms precipitate on the surface, forming FLG.[50;51]

Usually, an annealing step under an inert gas flow such as Ar is performed prior to growth to remove native oxides, increase grain size and clean the surface of the substrate.[50] H_2 is usually introduced into the chamber during the growth stage to allow the formation of volatile compounds that can be easily vented. The choice of carbon precursor, with different binding energies, changes growth thermodynamics and thus its parameters.[50;51] In general, pressure, chamber type and volume, total gas flows, ratios and substrate annealing have a key (and in many cases not well-known) role in graphene growth in terms of sample size, layer number, grain size, mobility, doping, etc..[26;48;50]

2.4.2 *Liquid-phase exfoliation*

Solutions of LEG in the form of SLG and FLG can be produced by dispersion and subsequent exfoliation of graphite flakes; this enables these materials to be vacuum filtered or ink-jet printed, producing continuous large-area thin-films. Usually, graphite powder is exfoliated down to SLG and FLG through a combination of ultrasonication and shear exfoliation, although the latter has probably been adopted as the standard due to the ease of process scaling.

Since graphite is hydrophobic, dispersion in water is achieved through surfactants such as sodium cholate (NaC) ($C_{24}H_{39}NaO_5$), or in appropiate solvents as in the case of n-methyl-2-pyrrolidone (NMP).[44;45]

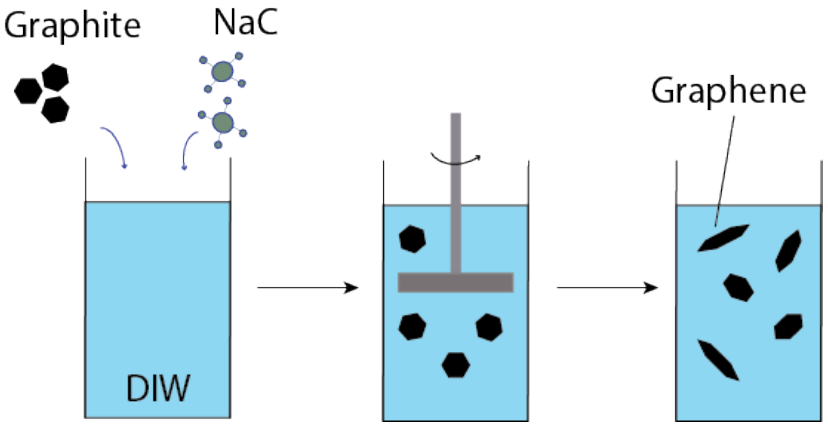

Figure 2.5: Schematic of an aqueous liquid exfoliation process. Firstly, graphite and NaC are introduced in water. Then, a high-shear mixer produces the final flakes of graphene.

Previous exfoliation processes have involved intercalated graphite; interaction with the intercalant through thermal shock or acid treatment enabled graphite exfoliation.[52;53] In liquid-phase exfoliation (LPE), the exfoliation occurs due to the strong interaction between the solvent and graphite nanowall, which overcomes the energetic cost required for exfoliation (this is the intralayer van der Waals energy per surface area).

Specifically, this process depends on the difference in the surface energy between the graphite surface and the solvent as follows from equation $\frac{\Delta H_{mix}}{V_{mix}} \sim \frac{2}{T_{flake}}(\delta_G - \delta_{Sol})^2\phi$, where $\frac{\Delta H_{mix}}{V_{mix}}$ is the entalpy of mixing per volume, T_{flake} is the flake thickness, δ_G is the square root of the surface energy of graphite and δ_{Sol} is of the solvent, and ϕ is the graphite volume fraction.[43] From this equation one can infere that the cost of exfoliation is minimised when solvent and graphite have similar surface energies, and then exfoliation occurs at an optimum rate. Usually, this process is assisted by a high shear blender, which provides a strong shear force in the mixture helping the exfoliation.[43;46;47]

This technique cannot compete with CVD in terms of quality of large area films; applications where electronic properties are fundamental cannot be carried out with this technique. Nevertheless, LPE is able to produce relatively high quantities of SLG and FLG with great scalability for mass-production and at low production costs. This LEG can be used to cover substrates by spraying or drop casting to create conductive

coatings, make conductive inks suitable for ink-jet printing of circuits and devices, or vacuum filtered films for TCFs for electrodes in light-emitting diode (LED) and PV devices.

Recently, exfoliation of other 2D materials has been realised too. The posibility of combining the complementary properties of such materials, together with the ease of processing of liquids and solutions, make them extremely attractive for low-cost electronics.[46;47]

2.5 GRAPHENE FUNCTIONALISATION

The properties of graphene can be engineered through functionalization or doping. The aim of the process is always to modify one or more features for a target, for instance increase or reduce conductivity, change its intrinsic hydrophobic nature or its reactivity to a certain compound. In this section, the two graphene-based materials that have been employed in this thesis will be introduced.

2.5.1 *Graphene oxide*

The material known as GO is a graphene sheet with O_2, hydroxide (-OH) and carboxylic acid (-COOH) groups (among other possible organic compounds) attached to its basal plane and edges, as seen in Figure 2.6. These functional groups change the sp^2 bonding and together with the additional electron clouds, increase electron scattering and thus reduce the conductivity.[54]

However, as benefits one can mention that GO is hydrophilic and readily dispersible in water. It is produced by the well-known Hummer´s method, which is a scalable method to produce massive quantities of GO in a cost-effective way, although electrodeposition is another scalable method which is emerging.[55;56] Also, due to band-gap opening, GO oxide possess luminescent properties that are useful for drug delivery and cell imaging.[32]

Due to its dispersability, vacuum filtration can be easily performed to achieve continuous large-area films of a few tens of nm in thickness. These films can be tuned by varying the concentration of GO filtered, which makes it a straightforward and very versatile method for producing layers of various thicknesses and good mechanical properties.[57] This technique has been used to create ultra-large are films producing

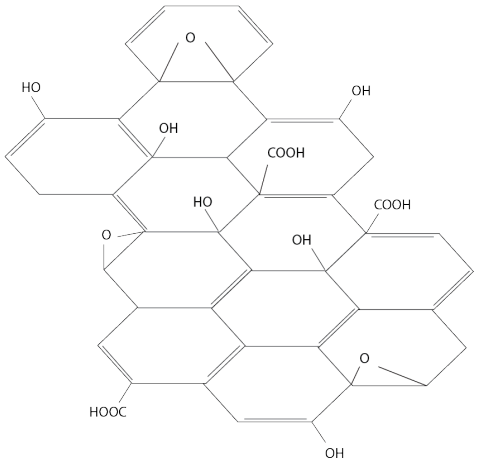

Figure 2.6: Graphene oxide structure.

GO paper-like structures.[58]

In addition, GO can be reduced with thermal annealing, photonic sintering or chemical treatments (such as hydrazine) to remove O_2 content and increase conductivity, creating what is known as reduced graphene oxide (r-GO). This is needed when used as TCF, since its conductivity can change by orders of magnitude.[57] A a very interesting route for large-scale production of high-quality graphene is the microwave reduction of solution processed GO, rendering films of comparable quality to those grown by CVD techniques.[59]

Moreover, GO possesses exceptional sensing properties, especially for humidity, due to the enhanced interaction of its basal plane with water and O_2-rich environments. This interaction is also amplified due to the large surface/volume ratio characteristic of the 2D materials (2630 cm^2g^{-1} for graphene). This results in a large change in the conductance of the material which is used as sensing parameter.[60;61;62;57]

2.5.2 *$FeCl_3$ intercalation*

The process of intercalation is generally understood as the introduction of molecules by the edge of a material, and their subsequent diffusion in between the layers . Intercalation of $FeCl_3$ in graphite had been achieved a few decades ago, and Li and Ca intercalations would result in a superconducting phase in graphite.[63;64;65] While Li intercalation has been achieved, but its fast degradation and limited environmental

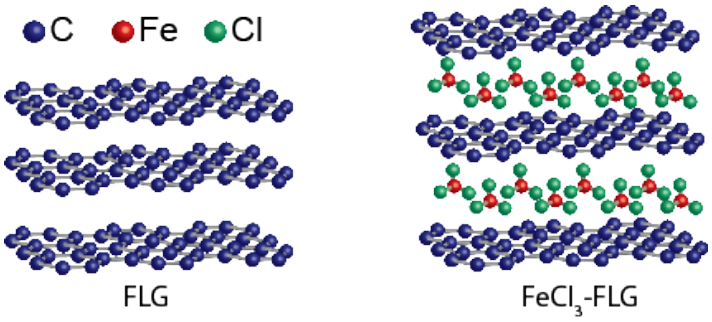

Figure 2.7: Schematic of the FLG and $FeCl_3$-FLG structures.

stability make it unsuitable for TCF applications.[66] As was mentioned before, the intrinsic values of resistivity of graphene make it unsuitable for TCFs applications, hence the necessity of doping.

To overcome this problem, in this thesis charge density of graphene is augmented through $FeCl_3$ intercalation. When molecules of $FeCl_3$ diffuse between graphene layers (see Figure 2.7), electron transfer occurs from the graphene sheets to the $FeCl_3$ molecules, effectively p-doping the material. The nature of this interaction is not well-known, but it is likely that the Fe atoms interact with graphene producing withdrawal of electrons through the very electronegative Cl atoms, which will be electron deficient when bonding to graphene.[67] This reduces the R_s down to ∼8 Ω/sq for mechanically exfoliated samples and ∼20 Ω/sq for Ni CVD-grown samples. The difference in R_s between the two materials is due to the larger number of defects and grain boundaries of the CVD samples, which are not present in mechanically exfoliated samples.

The reduced R_s are consequence of the increase in the charge density, up to $n = 9 \times 10^{14}\ cm^2$.[20;68] This shifts the E_F below the Dirac point down to ∼0.7-0.9 eV which results in a work-function of about ∼5.1 eV, which is of great interest for PVs, LEDs and organic electronics where a precise band-alignment is needed for efficient hole injection or extraction.

Remarkably, the mobility of the samples is in the same order of magnitude of pristine graphene samples, and it barely changes when transferred from a SiO_2 to a polyethylene terephthalate (PET) substrate.[20] This implies two things: that electron scattering arising from $FeCl_3$ is very low, and that substrate scattering is screened by the highly doped bottom $FeCl_3$-FLG layers. Also, transparency is just slightly

decreased, which indicated little $FeCl_3$ light absorption.[20]

BIBLIOGRAPHY

[1] P. R. Wallace. The band theory of graphite. *Physical Review*, 71, 1947.

[2] R. Peierls. Quantum theory. *Annales de l'institut Henri Poincaré*, 1935.

[3] K. S. Novoselov et al. Electric field effect in atomically thin carbon films. *Science*, 306, 2004.

[4] A. H. Castro Neto et al. The electronic properties of graphene. *Review Modern Physics*, 81, 2009.

[5] A. K. Geim et al. The rise of graphene. *Nature Materials*, 6, 2007.

[6] K. S. Novoselov et al. Two-dimensional gas of massless dirac fermions in graphene. *Nature*, 438, 2005.

[7] F Schwierz. Graphene transistors. *Nature Nanotechnology*, 5, 2010.

[8] L. A. Falkovsky. Optical properties of graphene. *Journal of Physics: Conference Series*, 129, 2008.

[9] M. F. Craciun et al. Properties and applications of chemically functionalized graphene. *Journal of Physics: Condensed Matter*, 25, 2013.

[10] R. Balog et al. Bandgap opening in graphene induced by patterned hydrogen adsorption. *Nature Materials*, 9, 2010.

[11] S-H. Cheng et al. Reversible fluorination of graphene: Evidence of a two-dimensional wide bandgap semiconductor. *Physical Review B*, 81, 2010.

[12] Y. Zhang et al. Direct observation of a widely tunable bandgap in bilayer graphene. *Nature*, 459, 2009.

[13] V. Barone et al. Electronic structure and stability of semiconducting graphene nanoribbons. *Nano Letters*, 6, 2006.

[14] Y-C. Chen et al. Tuning the band gap of graphene nanoribbons synthesized from molecular precursors. *ACS Nano*, 7, 2013.

[15] H. Yoon et al. Measurement of collective dynamical mass of dirac fermions in graphene. *Nature Nanotechnology*, 9, 2014.

[16] Q. H. Wang et al. Electronics and optoelectronics of two-dimensional transition metal dichalcogenides. *Nature Nanotechnology*, 7, 2012.

[17] D. Akinwande et al. Two-dimensional flexible nanoelectronics. *Nature Communications*, 5, 2014.

[18] J.-H. Chen et al. Charged-impurity scattering in graphene. *Nature Physics*, 4, 2008.

[19] T. H. H. Bointon et al. Is graphene a good transparent electrode for photovoltaics and display applications? *IET Circuits, Devices and Systems*, 9, 2015.

[20] I. Khrapach et al. Novel highly conductive and transparent graphene-based conductors. *Advanced Materials*, 24, 2012.

[21] L. Britnell et al. Strong light-matter interactions in heterostructures of atomically thin films. *Science*, 340, 2013.

[22] S. Roddaro et al. The optical visibility of graphene: interference colors of unltrathin graphite on sio2. *Nano Letters*, 7, 2007.

[23] F. H. L. Koppens et al. Photodetectors based on graphene, other two-dimensional materials and hybrid systems. *Nature Nanotechnology*, 9, 2014.

[24] R. R. Nair et al. Fine structure constant defines visual transparency of graphene. *Science*, 320, 2008.

[25] J. P. Kottmann et al. Plasmon resonant coupling in metallic nanowires. *Optics Express*, 8, 2001.

[26] X. Li et al. Large-area synthesis of high-quality and uniform graphene films on copper foils. *Science*, 324, 2009.

[27] K. S. Kim et al. Large-scale pattern growth of graphene films for stretchable transparent electrodes. *Nature*, 457, 2009.

[28] F. Bonaccorso and others. Graphene photonics and optoelectronics. *Nature Photonics*, 4, 2010.

[29] K. J. Tielrooij et al. Photoexcitation cascade and multiple hot-carrier generation in graphene. *Nature Physics*, 9, 2013.

[30] A. Celis et al. Graphene nanoribbons: fabrication, properties and devices. *Journal of Physics D: Applied Physics*, 49, 2016.

[31] X. Sun et al. Nano-graphene oxide for cellular imaging and drug delivery. *Nano Research*, 1, 2008.

[32] E. Goki et al. Field emission from graphene based composite thin films. *Applied Physics Letters*, 93, 2008.

[33] T. Gokus et al. Making graphene luminescent by oxygen plasma treatment. *ACS Nano*, 3, 2009.

[34] Y. D. Kim et al. Bright visible light emission from graphene. *Nature Nanotechnology*, 10, 2015.

[35] G. Prakash et al. Afm study of ridges in few-layer epitaxial graphene grown on the carbon-face of 4H–SiC($000\bar{1}$). *Carbon*, 48, 2010.

[36] E. Torres Alonso et al. Homogeneously bright, flexible, and foldable lighting devices with functionalized graphene electrodes. *ACS Applied Materials & Interfaces*, 8, 2016.

[37] A. A. Griffith. Vi. the phenomena of rupture and flow in solids. *Philosophical Transactions of the Royal Society of London A: Mathematical, Physical and Engineering Sciences*, 221, 1921.

[38] C. Lee et al. Measurement of the elastic properties and intrinsic strength of monolayer graphene. *Science*, 321, 2008.

[39] L. Banszerus et al. Ultrahigh-mobility graphene devices from chemical vapor deposition on reusable copper. *Science Advances*, 1, 2015.

[40] L. Wang et al. One-dimensional electrical contact to a two-dimensional material. *Science*, 342, 2013.

[41] S. Stankovich et al. Graphene-based composite materials. *Nature*, 442, 2006.

[42] X. Qi et al. Amphiphilic graphene composites. *Angewandte Chemie International Edition*, 49, 2010.

[43] Y. Hernandez et al. High-yield production of graphene by liquid-phase exfoliation of graphite. *Nature Nanotechnology*, 3, 2008.

[44] J. N. Coleman. Liquid exfoliation of defect-free graphene. *Accounts of Chemical Research*, 46, 2013.

[45] K. R. Paton. Scalable production of large quantities of defect-free few-layer graphene by shear exfoliation in liquids. *Nature Materials*, 13, 2014.

[46] J. N. Coleman et al. Two-dimensional nanosheets produced by liquid exfoliation of layered materials. *Science*, 331, 2011.

[47] V. Nicolosi et al. Liquid exfoliation of layered materials. *Science*, 340, 2013.

[48] A. Reina et al. Large area, few-layer graphene films on arbitrary substrates by chemical vapor deposition. *Nano Letters*, 9, 2009.

[49] M Losurdo et al. Graphene cvd growth on copper and nickel: role of hydrogen in kinetics and structure. *Phys. Chem. Chem. Phys.*, 13, 2011.

[50] Y. Zhang et al. Review of chemical vapor deposition of graphene and related applications. *Accounts of Chemical Research*, 46, 2013.

[51] R. Muñoz et al. Review of CVD synthesis of graphene. *Chemical Vapor Deposition*, 19, 2013.

[52] C. Guohua et al. Preparation and characterization of graphite nanosheets from ultrasonic powdering technique. *Carbon*, 42, 2004.

[53] X. Li et al. Chemically derived, ultrasmooth graphene nanoribbon semiconductors. *Science*, 319, 2008.

[54] R. K. Singh et al. Graphene oxide: strategies for synthesis, reduction and frontier applications. *RSC Advances*, 6, 2016.

[55] D. Marcano et al. Improved synthesis of graphene oxide. *ACS Nano*, 4, 2010.

[56] D. R. Dreyer et al. The chemistry of graphene oxide. *Chem. Soc. Rev.*, 39, 2010.

[57] S-H. Kang et al. Electrical and mechanical properties of graphene oxide on flexible substrate. *Journal of Physics and Chemistry of Solids*, 74, 2013.

[58] D. A. Dikin et al. Preparation and characterization of graphene oxide paper. *Nature*, 448, 2007.

[59] D. Voiry et al. High-quality graphene via microwave reduction of solution-exfoliated graphene oxide. *Science*, 71, 2016.

[60] S. Borini et al. Ultrafast graphene oxide humidity sensors. *ACS Nano*, 7, 2013.

[61] H. Bi et al. Ultrahigh humidity sensitivity of graphene oxide. *Scientific Reports*, 3, 2013.

[62] L. Ganhua et al. Reduced graphene oxide for room-temperature gas sensors. *Nanotechnology*, 20, 2009.

[63] M. S. Dresselhaus et al. Intercalation compounds of graphite. *Advances in Physics*, 51, 2002.

[64] K. R. Kganyago et al. Structural and electronic properties of lithium intercalated graphite lic_6. *Physical Review B*, 68, 2003.

[65] T. E. Weller. Superconductivity in the intercalated graphite compounds c6yb and c6ca. *Nature Physics*, 1, 2005.

[66] W. Bao et al. Approaching the limits of transparency and conductivity in graphitic materials through lithium intercalation. *Nature Communications*, 5, 2014.

[67] D. Zhan et al. $FeCl_3$-based few-layer graphene intercalation compounds: Single linear dispersion electronic band structure and strong charge transfer doping. *Advanced Functional Materials*, 20, 2010.

[68] T. H. Bointon et al. Large-area functionalized cvd graphene for work function matched transparent electrodes. *Scientific Reports*, 5, 2015.

3

EXPERIMENTAL METHODS

3.1 INTRODUCTION

In this chapter, the techniques employed to produce, process and characterise the samples and their performance are presented. This chapter is intended, however, to be an overview; the aim of this thesis is to bridge the gap between research and industry, thus most of the techniques employed are well-known. Luckily, the planar nature of graphene makes it already compatible with most of the complementary metal oxide semiconductor (CMOS) processing techniques and schemes available.
The methods to produce graphene started with mechanical exfoliation, capable of producing micrometer-sized graphene flakes, reaching stages where roll-to-roll (R2R) processes combined with chemical vapour deposition (CVD) are capable of producing continuous 30' films of single-layer graphene (SLG).[1] With the discovery of liquid-exfoliated graphene (LEG), cost-effectiveness and production scalability are achieved in expense of quality. The latter two will be the ones discussed here. Doping methods to further reduced the resistivity, and characterisation techniques to assess quality, number of layers and electrical behaviour are also explained.

3.2 GRAPHENE FABRICATION

Many methods can be used to grow or produce graphene. As mentioned, mechanical cleavage is only suitable for research grade samples. For consumer applications, two routes present processes feasible to be used in mass-produced devices with graphene. These are CVD and liquid-phase exfoliation (LPE), which are the methods employed

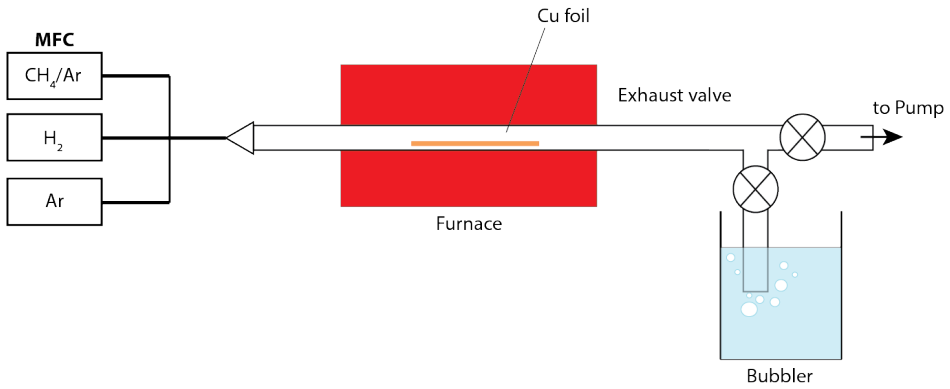

Figure 3.1: Schematic of the furnace used for APCVD growth of graphene.

in this thesis and the ones attention will be focused onto.

3.2.1 *CVD graphene*

The process of CVD in graphene is as any other CVD process for layer growth. In this thesis, multilayer Ni-grown graphene was purchased from Graphene Supermarket. This was used in Chapters 4 and 5 for the realisation of iron-chloride intercalated few-layer graphene ($FeCl_3$-FLG) and few-layer graphene (FLG) transparent electrodes for alternating-current electroluminescence (ACEL) devices and touch-sensors. In Chapters 4 and 5, SLG was employed with the same purpose of transparent conductive film (TCF). However, SLG was grown with atmospheric pressure and low-pressure CVD. In both cases, Cu foils were used a substrate as SLG preferentially grows on it.[2] The precursors gas flows were regulated using a mass-flow controller (MFC).

Low-pressure CVD was carried out with a cold-wall nanoCVD unit from Moorfield Instruments. After loading 25 μm thick copper foils from Alfa Aesar, the chamber was quickly pumped down to a few mTorr, pressure which is maintained throughout all the process (which is never above 10 $mTorr$). Then, fast-heating was achieved (over 800 ^oC/min) through a resistive heating stage. An annealing step is carried out to remove native copper oxides formed by exposure to ambiental conditions and to increase grain size in the substrate to improve graphene quality; this is done under an H_2 (20 $sccm$) atmosphere at 1000 ^oC. Then, CH_4/H_2 are introduced in the chamber at a ratio of 1:1 to start graphene growth. This ratio was chosen after some optimization runs, where graphene growth and etching resulting from an excess of H_2 was balanced. Then, the

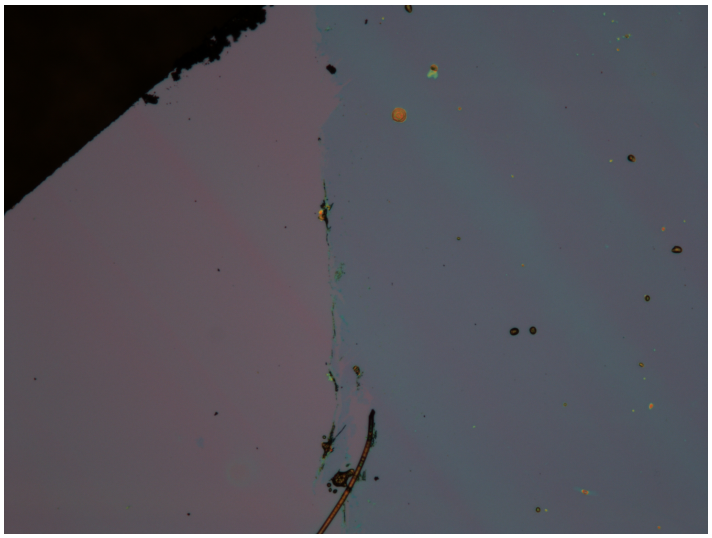

Figure 3.2: Optical microscope picture of a CVD-grown SLG film on a SiO_2/Si. The slighly bluish area on the right corresponds to the graphene film, where some residual contamination from the Cu substrate and PMMA-assisted transfer is also apparent.

sample is let to cool down under an Ar (20 *sccm*) flow. A picture of the films can be seen in Figure 3.2.[3]

In the case of atmospheric pressure growth, a custom-built furnace was used as seen in Figure 3.1. A hot-wall furnace from MTI Instruments is loaded with the copper foils. After loading the samples , the tube was pumped down and flushed with Ar (100 *sccm*) for 5 minutes at low pressure. Then, the tube is brought to atmospheric pressure closing the exhaust valve and filling the tube with Ar (300 *sccm*) for 5 minutes. Then, the bubbler valve is open, releasing excess Ar and equilibrating the pressure. The temperature was then ramped up (33^oC/min) to 1000 ^oC and an annealing was performed under H_2 (70 *sccm*) and Ar (230 *sccm*) flow for 15 minutes to remove native oxides and increase grain size. Growth was then triggered introducing a Ar/CH_4 source (200/10 sccm) in the line as carbon precursor, and maintained for 15 minutes. This diluted carbon source was deliberately chosen since at higher pressures the decomposition rate is increased and thus the layer number increases too; since SLG growth is desired, a low CH_4 concentration is targeted to minimise this effect.[4;5] Then, the heating was stopped, the gas lines were shut, the bubbler valve was switched off, the exhaust valve was switched on and the tube was then pumped down under Ar (300

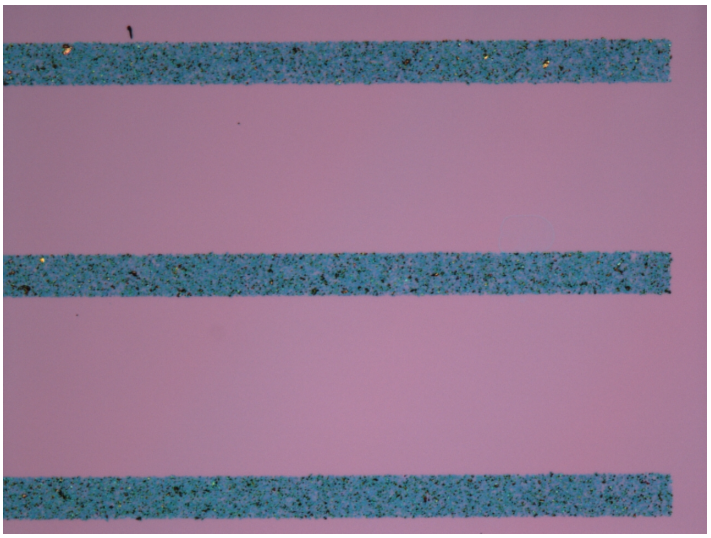

Figure 3.3: Optical microscope picture of a LEG patterned film on a SiO_2/Si. The thinner and thicker graphene and graphite flakes are distinguishable by contrast.

sccm) flow and left to cool down.

3.2.2 *Liquid-exfoliated graphene*

LEG was produced by shear exfoliation of graphite (from Sigma-Aldrich) in water. Since graphite is hydrophobic, sodium cholate (NaC) ($C_{24}H_{39}NaO_5$) from Sigma-Aldrich was used to change surface interaction with water and make graphite hydrophilic allowing its dispersion. 15 g of graphite powder were dissolved in 1 L of water with the help of 5 g of NaC. Then, the mixture was introduced into a shear mixer from Silverson with a rotor size of 4.5 cm in diameter and blended at a speed of 6000 rpm for 2 hours. The solution was centrifuged for 60 minutes at 8000 rpm and then decanted. Then, a second centrifugation and decantation step was performed to further optimise the graphene dispersed. The final graphene thickness has an average of 5 layers, consistent with previous reports.[6;7] Lines of LEG are shown in Figure 3.3.

3.2.3 *Graphene transfer*

Depending on the type of graphene, three different transfer methods were performed. For standard CVD graphene, the standard poly(methyl methacrylate) (PMMA)-assisted

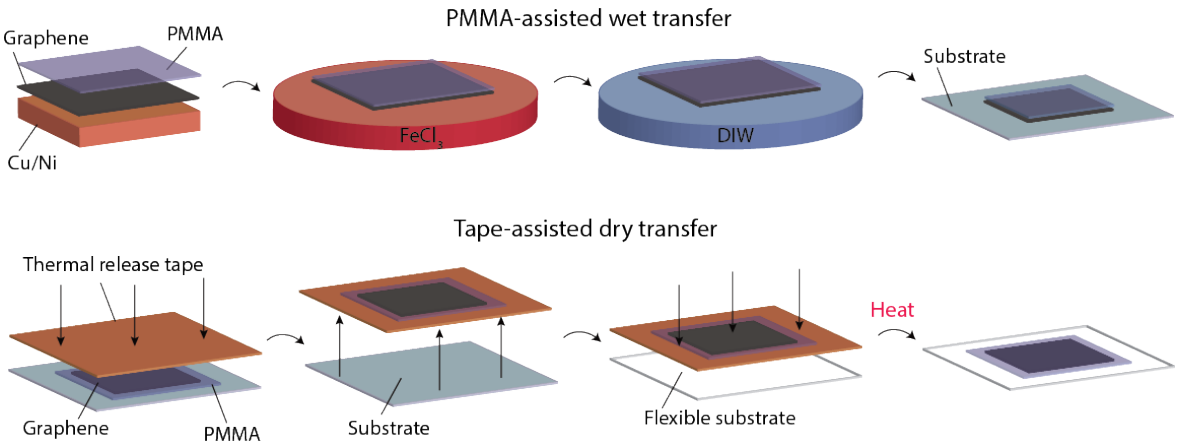

Figure 3.4: Schematic of the PMMA-assisted wet-transfer method (top) and Tape-assisted dry-transfer method (bottom).

wet transfer was performed (see Figure 3.4). After spinning a thin layer of PMMA 450K A6 (400 nm) over the graphene/Cu or graphene/Ni films, the sample was introduced in a 1 M iron chloride (III) ($FeCl_3$) avoiding immersion. In the case of Cu, a reactive ion etching (RIE) step was performed prior to $FeCl_3$ etching to remove the graphene grown on the backside of the Cu, which would prevent contact with the etchant solution.

The $FeCl_3$ solution etches both Cu and Ni, and leaves only the PMMA/graphene membrane floating on the surface. After transferring this film to de-ionised water (DIW) several times, the target substrate is placed under the membrane and the film is scooped out and left to dry for at least 12 hours. Usually, a mild RIE O_2 plasma is performed on the target substrate to increase hidrophilicity prior to the transfer, which usually results in better film transfers. The PMMA can be removed with an acetone bath, and the graphene is ready to be processed.

In the case of $FeCl_3$-FLG a dry transfer method is performed (see Figure 3.4). After coating the sample with PMMA, which acts just as a protection layer, a thermal-release tape is sticked onto the PMMA/graphene membrane. A 2 kg weight is placed on top to ensure good attachment for 5 minutes. Then, the thermal-release tape is slowly and gently pulled up, releasing the PMMA/graphene membrane from the substrate.

This tape is then placed onto the target substrate, pressed down, and place on a hotplate. The temperature is then gently ramped up to 100-110 ^oC; at this temperature, the thermal-release tape loses its adherence and releases the sample. The

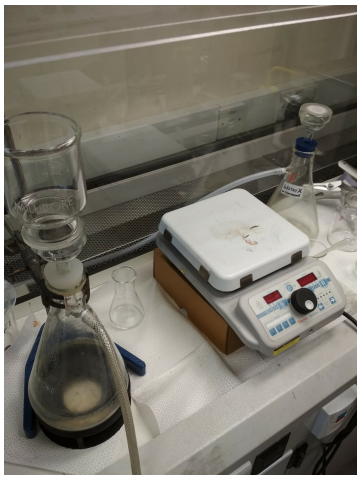

Figure 3.5: Picture of the vacuum-filtration setup. Next to it the hotplate used to carry out the IPA-transfer.

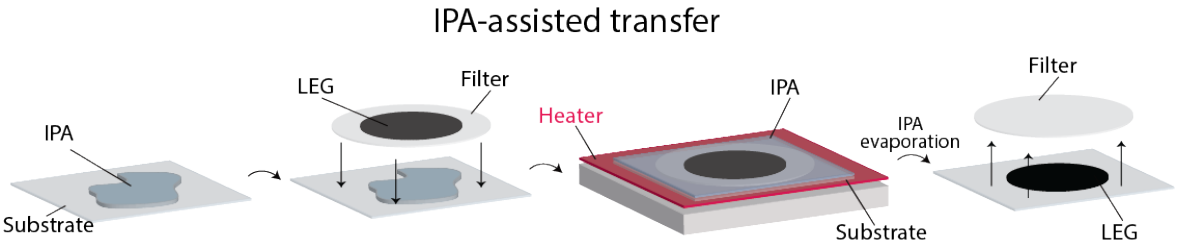

Figure 3.6: Schematic of the IPA-assisted transfer process.

PMMA/graphene sample remains attached to the substrate by van der Waals interactions. The protective PMMA layer is rinsed off with acetone and transfer is then finished.

For LEG and graphene oxide (GO) films, the process employed is a combination of vacuum filtration and water- or IPA-assisted transfer method which our group developed. The setup can be seen in the Figure 3.5. Using a pump, the LEG and GO solutions are filtered through polytetrafluoroethylene (PTFE) and cellullose filters respectively. The thickness of the film can be tuned by varying the concentration of the solution. The PTFE filters with LEG films are placed on an substrate which has been covered with water- or isopropanol (IPA) and placed on a hotplate, with the LEG facing down, in direct touch with the substrate, as shown in the Figure 3.6.

The temperature is ramped up in the hotplate, and then the water or the IPA are

evaporated. While evaporating, the filter is dragged down towards the substrate by means of its surface tension, and makes the filter stick to it, although not strongly. After the filter is pulled away, the graphene is effectively transferred to the substrate by means of mild exfoliation onto the substrate. Usually, a few depositions are needed to achieve conductive films. Both water and IPA-assisted methods were employed for LEG; in the case of GO, water is the only solvent used instead of IPA, and instead of temperature the release of the GO films is driven by a quick blow-dry with a N_2 gun to the backside of the filter.

3.3 DEVICE FABRICATION

Device fabrication was carried out using standard semiconductor processing techniques, most of them compatible with CMOS processes. Since the techniques are well-known, a rather simple overview is presented.

Spin coating was the technique employed to produce reproducible thicknesses in optical lithography (OL) processes, ACEL device fabrication and coating in general.

Patterns were created with a laser writer from Durham MagnetOptics, operating with a laser source of 405 nm. The spot size could be tuned to optimize patterning speed from 0.6 to 5 μm. Photoresist S1813 and polymethylglutaramide (PMGI) lift-off resist from MicroChem were spun by spin coating, with thicknesses of around 1.4 μm. The former is an imaging resist, and the latter produces an undercut that helps the lift-off process after metallisation. Once exposed, the cross-linked resist can be removed with the help of MF-319 developer from MicroChem, which is an aquous tetramethyl-ammonium hidroxide (TMAH) solution. This also etches the PMGI underneath. Interestingly, S1813 is removed with acetone and IPA but PMGI is not, which is taken advantage of in Chapter 6.

To produce metal thin-films for device contacts, thermal evaporation was used. A thin wetting layer of 5 nm of Cr was deposited prior to a 70 nm Au layer. Al was also used as a contact in very few devices. The excess metal is removed by means of lift-off in acetone or n-methyl-2-pyrrolidone (NMP) if PMGI is used.

Removal of CVD graphene after patterning was achieved through RIE, with either O_2 or Ar plasma.

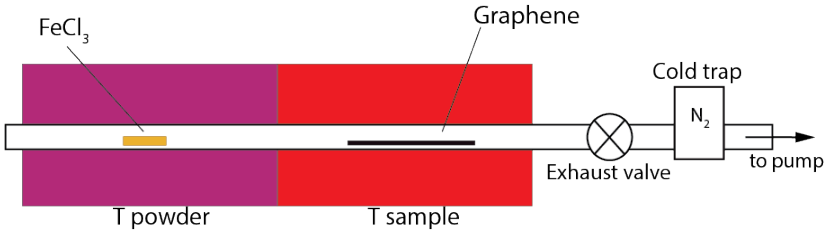

Figure 3.7: Schematic of the furnace used in the intercalation of FLG by $FeCl_3$.

3.4 INTERCALATION OF FEW-LAYER GRAPHENE

The intercalation of FLG was carried out with the two-zone vapour transport method previously demonstrated by our group. Anydrous $FeCl_3$ powder was placed in a crucible and then loaded into a quartz tube (see Figure 3.7). The tube is then pumped down to 10^{-4} $mBar$ with a rotary pump first and then a turbo-pump to achieve 10^{-7} $mBarr$. A liquid N_2 cold trap is placed in the way to achieve low pressures in the system.

There are two zones within the furnace (MTI Instruments) that are heated: T_{sample} and T_{powder} at 360 and 315 ^oC respectively. At that temperature, the powder sublimates producing $FeCl_3$ vapour that fills the tube; the sample is kept at 360 ^oC to produce a thermal bath which enhances layer decoupling and thus intercalation. This is carried out for 8 hours generally to ensure succesful $FeCl_3$ intercalation has happened. The vapour then condenses at the ends of the tube, as well as on top of the sample in smaller amounts, forming crystals. However, T_{powder} is lowered first to stop sublimation while keeping T_{sample} constant, trying that the $FeCl_3$ condenses away from the sample as much as possible. The furnace is left to cool down, with final pressures in the range of 10^{-2} $mBar$ after the intercalation step. The tube is then pumped down to remove vapours produced in the process; here, the liquid N_2 traps the $FeCl_3$ fumes that remain in the tube, avoiding system contamination.

3.5 CHARACTERIZATION

In this section, the methods used to characterise the materials and devices presented in this thesis are discussed. The quality of graphene, number of layers, degree of doping, thickness of the films, its conductivity and morphology are assessed using four simple techniques.

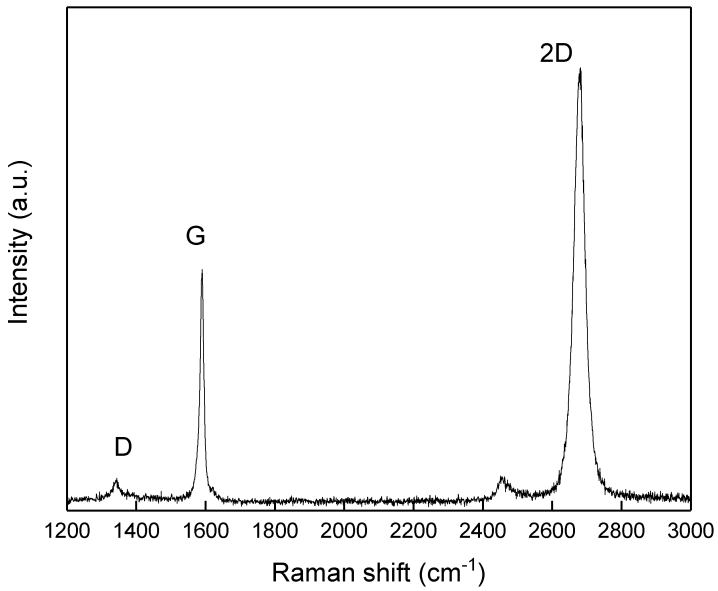

Figure 3.8: Raman spectra of a CVD-grown SLG film.

3.5.1 *Raman scattering in graphene*

Raman spectroscopy is a widely used technique in the study of crystalline structures, which relies in the interaction of light with the lattice of the material. It is a non-destructive, easy and fast technique. In the case of graphene, it provides information about the number of layers and their orientation, disorder, strain, doping and even edge orientation; this is due to the remarkable access that Raman spectroscopy has to the electronic structure of graphene.[8;9;10]

There are 3 main peaks in which most of the information of graphene is contained: G, D and 2D modes, as seen in the Figure 3.8, where a typical SLG Raman spectrum is shown.

The lattice displacements that give rise to the G peak, at 1580 cm^{-1}, are seen in the Figure 3.9. This G peak arises from the stretching of the sp^2 bonds that form the lattice, corresponding to the E_{2g} vibrational mode. Due to this, the G peak shifts with strain because the stressed bonds undergo a change in their energy and thus their resonant frequency. This peak is always present, it is a signature of sp^2 bonding.[8;10]

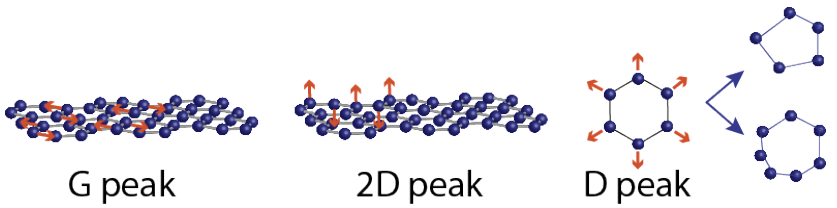

Figure 3.9: The 3 vibrational modes giving rise to the G, 2D and D peaks.

It also can serve as an indication of doping: changing the charge density produces a shift in the G peak due to the change in screening of the ionic potential created by the nucleii. This effect is enhanced in graphene due to a Kohn anomaly.[11] Theoretical calculations have been done by Lazzeri *et al* to calculate the shift (see Figure 3.10) in a Raman G peak relative to the charge density; thus, one can quickly estimate the doping level without the necessity of doing any invasive processes or measurements.[11]

The intensity of the G peak is related with the layer number: a higher layer number will result in a more intense G peak signal due to a larger number of atoms present and thus a larger number of excitations. Usually, its intensity is compared to that of the 2D peak for an estimation of the layer number.

The 2D peak arises from the A_{1g} vibrational mode (see Figure 3.9), and due to this out-of-plane vibration it provides information about the number of layers. For SLG only one transition is posible, giving rise to a single 2D peak. However, the electronic structure of bilayer graphene (BLG) possesses a double dispersion band, which enables four different transitions, which accounts for the four different peaks of BLG as seen in the Figure 3.11. The 2D peak drastically changes its shape with the number of layers.

However, the shape of the 2D peak remains almost unchanged after 5 layers; then complimentary methods such as atomic force microscopy (AFM) are necessary, and comparison of the intensity of G/2D peaks is carried out too. Usually, in mechanically exfoliated samples, for SLG a G/2D=0.5 is expected, for BLG G/2D=1, for trilayer graphene (TLG)=1.5. Comparison between G/2D and shape and full-width half maximum (FWHM) of 2D peak is usually enough for graphene samples with layers up to four layers.

The shape of the 2D peak can also provide valuable information. Fitting to one, four or three lorenztians is signature of SLG, BLG and TLG respectively. Also, the FWHM can be determined; usually SLG has a FWHM of 30 cm^{-1}, BLG of 45 cm^{-1}

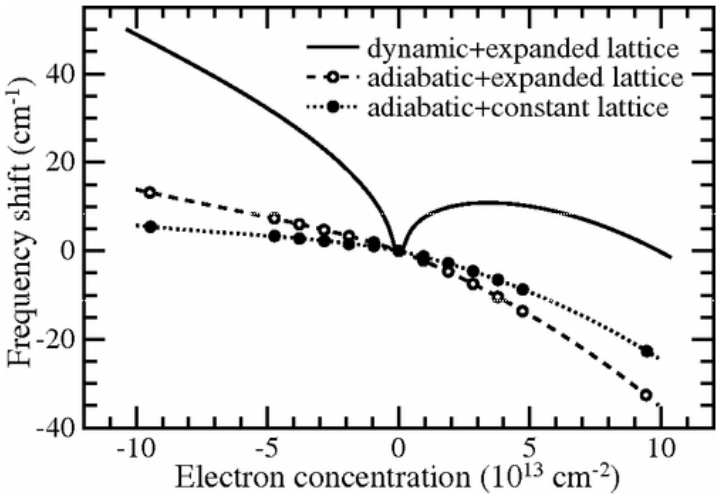

Figure 3.10: Raman peak shift as function of doping. The relation used corresponds to that of the dynamic + expanded lattice. Reproduced with permission from [11].

and TLG of 60 cm^{-1}. This is particularly useful in CVD samples as their lower degree of crystallinity might blur out these features.

Doping is determined by analysing the shift in the G peak with respect to its undoped position (1580 cm^{-1}). As described above, Lazzeri *et al* provide a theoretical estimation of doping concentration related to the G peak shift (see again Figure 3.10).[11] Complementary electrical measurements indicate that this theoretical estimation holds within 10 % of error.

Ordering can be determined examining the D/G intensity. The D peak results from the "breathing" motion of the C atoms, as seen in the Figure 3.9. It is related with defect density, since it requires a defect (a lacking or an extra atom) for the process to occur (see again Figure 3.9). Usually, a quick inspection to the D/G ratio serves as an estimation of the quality of the sample: a high D/G ratio indicates a high defect density (D/G=0.5 is usually considered a good threshold for high-quality graphene).

In mechanically exfoliated samples, this peak is not present since the lattice is pristine; in CVD samples however this D peak is usually a good quality benchmark, where a low D/G ratio indicates large grain size and thus better electronic properties. Both the D and the 2D peak are dispersive with the excitation wavelength, so this has to be considered when analising the data.[8;9;10]

The possibility of performing scans, rastering the sample with the laser source,

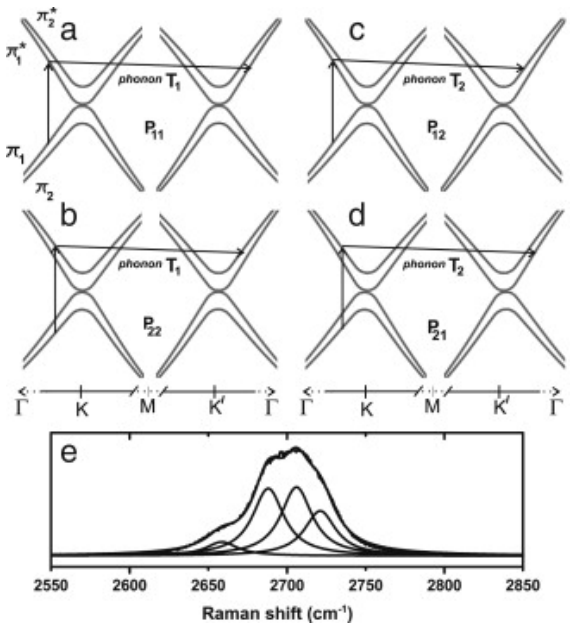

Figure 3.11: The four possible transitions corresponding to the multi-peak shape of the 2D peak in BLG. Extracted with permission from [8].

allows a complete spatial mapping of doping levels, strain and layer number; Raman spectroscopy is probably the only technique capable of doing this, simultaneously, in a fast and non-destructive way.

Raman spectroscopy was performed using a 532 nm green laser as an excitation source on a Renishaw confocal Raman spectroscope with a 40x lens, which provides a spot size of 1 μm. The power was limited to a few μW to avoid heating and sample damage. Also, all the spectra were normalised to the Si peak at 520 nm for an accurate comparison between different scans. For the number of layers, usually the ratio of the intensity between the G and 2D peak is analysed. G/2D is 0.5, 1 and 1.5 for SLG, BLG and TLG respectively. From 3 layers on, it becomes difficult to tell and complementary methods are needed.

3.5.2 *Raman scattering in $FeCl_3$-FLG*

The Raman spectrum of $FeCl_3$-FLG has a few features that distinguish it from that of pristine graphene, as seen in Figure 3.12. First, the G peak presents multiple features: this is an indication of different doping stages, as seen in Figure 3.12. If graphene is

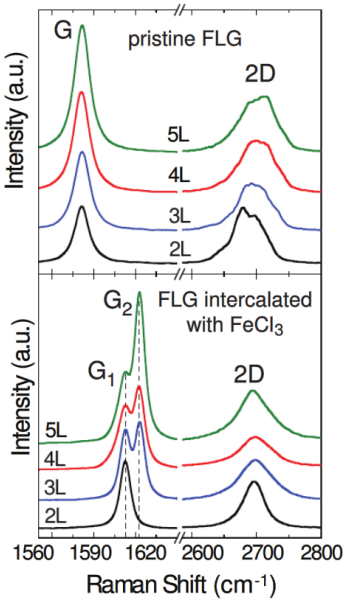

Figure 3.12: Two different Raman spectra: top spectrum corresponds to the single G peak and multilayer 2D features of FLG, and the bottom spectrum corresponds to the multi-peak structure of the G peak and single-layer 2D features in $FeCl_3$-FLG. Extracted with permission from [13].

present with only one $FeCl_3$ adjacent layer, this produces a peak at 1615 cm^{-1}, that is defined as G_1 peak; if graphene is sandwiched between two $FeCl_3$ adjacent layers this results in a peak at 1625 cm^{-1}, defined as G_2. The higher the $FeCl_3$ content, the larger the charge transfer is, the larger the doping is and the larger the shift in wavelength is.[12;13]

Also, the multipeak structure of the 2D peak at 2680 cm^{-1} is lost and a single peak with reduced FWHM, resembling that of SLG, is seen. This is an indication of effective intercalation and layer decoupling.[12;13] Thus again, with a simple non-destructive technique, we are able to determine the degree of intercalation and hence the doping level of the sample.

3.5.3 *Electrical measurements*

To characterise the materials´ electrical properties, measurements for conductivity and sheet resistance (R_s), impedance were performed. Usually, DC voltages were measured with an Agilent multimeter, a 2400 Keithley was used as DC power source and AC impedances were measured with a Hammeg 8008 LCR bridge. Usually, devices were contacted using a probe station, although ball wedge-bonding was employed in a few occasions.

In order to characterise the conductivity of the films, contacts at different distances were produced to extract resistance as a function of channel lenght. The total resistance measured R will be $R = R_s\frac{L}{W} + 2R_c$, where R_s is the sheet resistance of the material, L its length and W its width. So, varying L allows us to produce a fitting that provides both R_s as the slope and $2R_c$ as the intercept.

3.5.4 *Atomic force microscopy*

The AFM technique relies on the atomic interaction between a very sharp tip, placed at the end of a cantilever, and the surface of the sample. This technique allows for profiles and maps of surfaces with very high resolution. The signal comes from the defection of the cantilever due to the interaction with the sample profile/surface, which is usually recorded with a laser and a photo-detector.

A common mode in which to perform AFM is the contact mode, where the sample is in contact with the sample. One can decide to keep the height constant and record the

changes in deflection provoked by the interaction between the tip and the sample; this deviation of the cantilever produces a profile of the surface. This mode is the constant height mode, the most commonly employed mode, it was the one performed in the experiments of this thesis, using a DC bias. High resolution (sub-nm range) topography profiles can be realised with this technique. One can also record the lateral deviation of the tip can also be measured, and this signal usually provides a sharper image of the morphology of the sample. Because the tip and thus the cantilever is deflected upon contact, it is an indirect measurement of the friction between the material sampled and the AFM tip. This is particularly useful when imaging different materials, which will provide a sharp contrast due to differences in their mechanical properties. Also, back and forth rasters are generally substracted one from another to eliminate artifacts in this mode.

A Bruker Innova AFM was used to perform both maps and profiles; to extract the roughnesses and thicknesses of the samples, the software Gwyddyon was used.

3.5.5 *Scanning electron microscopy*

For quick inspection of conductive samples, scanning electron microscope (SEM) provides a relatively quick and high resolution technique for sample inspection. A very fine beam of electrons is shone on to the sample, which interacts with it to provide so-called secondary electrons, backscattered electrons, X-rays, etc; they can be detected and used to provide not only topographic images down to the nanoscale but also chemical composition of the material. The SEM pictures shown in this work were taken with a Hitachi S3200N.

BIBLIOGRAPHY

[1] S. Bae et al. Roll-to-roll production of 30-inch graphene films for transparent electrodes. *Nature Nanotechnology*, 5, 2010.

[2] F. Otakar et al. Interaction between graphene and copper substrate: The role of lattice orientation. *Carbon*, 68, 2014.

[3] T. H. Bointon et al. High quality monolayer graphene synthesized by resistive heating cold wall chemical vapor deposition. *Advanced Materials*, 27, 2015.

[4] X. Li et al. Large-area synthesis of high-quality and uniform graphene films on copper foils. *Science*, 324, 2009.

[5] H. Mehdipour et al. Kinetics of low-pressure, low-temperature graphene growth: Toward single-layer, single-crystalline structure. *ACS Nano*, 6, 2012.

[6] Y. Hernandez et al. High-yield production of graphene by liquid-phase exfoliation of graphite. *Nature Nanotechnology*, 3, 2008.

[7] K. R. Paton et al. Scalable production of large quantities of defect-free few-layer graphene by shear exfoliation in liquids. *Nature Materials*, 13, 2014.

[8] L. M. Malard et al. Raman spectroscopy in graphene. *Physics Reports*, 473, 2009.

[9] A. C. Ferrari et al. Raman spectroscopy of graphene and graphite: Disorder, electron–phonon coupling, doping and nonadiabatic effects. *Solid State Communications*, 143, 2007.

[10] A. C. Ferrari et al. Raman spectroscopy as a versatile tool for studying the properties of graphene. *Nature Nanotechnology*, 8, 2013.

[11] M. Lazzeri et al. Nonadiabatic kohn anomaly in a doped graphene monolayer. *Physical Review Letters*, 97, 2006.

[12] I. Khrapach et al. Novel highly conductive and transparent graphene-based conductors. *Advanced Materials*, 24, 2012.

[13] D. Zhan et al. $FeCl_3$-based few-layer graphene intercalation compounds: Single linear dispersion electronic band structure and strong charge transfer doping. *Advanced Functional Materials*, 20, 2010.

4

$FECL_3$-FLG ELECTRODES FOR FLEXIBLE LIGHT-EMITTING DEVICES

4.1 MOTIVATION

Displays and screens are some of the most important devices within the field of optoelectronics. Large-area displays are ubiquitious in advertising, ambient lighting, television, and even light therapy to treat skin deseases. These displays should be robust, withstand mechanical shocks and harsh environmental conditions. The trend nowadays in consumer electronics is towards flexible and wearable devices; then, exceptional mechanical properties are needed, and good conductivity is needed to minimize driving voltage and increase lighting area. This would allow truly expandable displays for electronics paper, smartphones and TVs, wallpapers and rollable screens.[1;2]

Currently, alternating-current electroluminescence (ACEL) is probably the most (and maybe the only) mature technique capable of producing homogenous lightning on large area displays, which are also flexible, capable of withstanding mechanical shocks and with good contrast.[3;4] Their fabrication process is straightforward and easily scalable. If the transparent electrode is patterned, micrometre features can be implemented to include text or images, that would help to deliver the targeted information. The maximum size of these ACEL panels is limited to metre square size due to significant brightness drop in the electrodes; this effectively limits the size of these panels. This also results in the need of high power and frequency which would increase power consumption and promote device degradation.[5;6;3]

The standard in transparent conductive electrodes for optoelectronics is indium tin oxide (ITO), which transparency around ∼90 % and sheet resistances of ∼10s of

Ω/sq are usually taken as reference for comparison with novel transparent conductive electrodes. However, ITO is not flexible, the scarcity of In makes it increasily expensive and the well-known problem of its diffusion into device components make it difficult to accomodate within flexible electronic devices.[7;8]

Among the flexible transparent electrodes, poly(3,4-ethylenedioxythiophene) polystyrenesulfonate (PEDOT:PSS) is a transparent conductive polymer widely used in flexible optoelectronics, due to its good mechanical properties. However, PEDOT:PSS has a sheet resistance of ∼850 kΩ/sq for an optical transparency of ∼90 %, an unwanted blue tinge and a limited environmental stability: when exposed to relative humidity of just ∼40 %, the uptake of water by hygroscopic PSS leads to the development of shear lips when the films are stressed/deformed, which dramatically increases resistance.[9;10;11] Furthermore, this water absorption together with the PSS acidity is a well-known cause of device degradation.[11]

Metallic thin films of silver and copper coupled with metal-organic compounds have been also employed as transparent conductive film (TCF), although their high performance is intrinsically linked to their low work-function and organic photovoltaics (PV) they were used in, where electron transport and extraction plays a key role.[12;13] Another emerging TCF are metallic nanowires (NW) films. Their values of transparency and sheet resistance are unrivaled; however, nanowire dimensions have to be accurately controlled to avoid failure due to mechanical stresses, they suffer from optical haze due to different size and spacing of these nanowires, they lack electrical stability because of current-induced damage and are prone to electromigration-induced structural defects.[14;15;16] The last two characteristics make them virtually incompatible with the ACEL technology, which relies on high AC voltages for illumination; however metal nanowires, specially copper- and silver-based, are being employed in touch-sensing applications, where the trend is to replace the expensive silver with the cheaper copper.

Carbon-based materials are emerging as a candidate for replacing ITO, due to their inherent high conductivity and flexibility. For instance chemical vapour deposition (CVD)-grown single-layer graphene (SLG) has a very high transparency (∼97 %), but its high resistance of ∼1000 Ω/sq hinders its potential as TCF as discussed previously; there have been reports of ACEL devices using carbon nanotubes (CNT) as TCF, but their high resistivities (5 kΩ/sq) prevents their use in large-area displays.[17]

A solution for this problem is to engineer the properties of graphene to make it

suitable as TCF. CVD-grown few-layer graphene (FLG) on Ni was chosen, with a transparency of around ∼80 % and sheet resistance of around ∼300 Ω/sq, to intercalate molecules of iron chloride (III) ($FeCl_3$). This drastically reduces the resistance of the material by one order of magnitude without alterring its transparency, achieving specifications close to those of ITO. For the same thickness, iron-chloride intercalated few-layer graphene ($FeCl_3$-FLG) can carry 10 times as much current as copper;[18] this makes it interesting for future replacement of copper in chip interconnects approaching the nanoscale.[19]

This $FeCl_3$-FLG electrode is very suitable to power ACEL devices due to the large voltages that such devices operate under. It is observed that their brightness was increased compared to that of pristine FLG; moreover, when comparing them with SLG, PEDOT:PSS and FLG, it is shown that $FeCl_3$-FLG present no observable brightness gradient whilst other materials do. Final tests were conducted to test their mechanical resilience, where devices where folded without change of brightness, and which resilience to different strains was comparable to PEDOT:PSS.

4.2 PHYSICS OF ACEL DEVICES

One of the first reports of electroluminescence was by Destriau in 1936 for ZnS powder layers.[3] It was not after 1950´s that Piper and Williams, Alfrey and Taylor developed a theoretical framework and described empirically some of the properties of these powders. Nevertheless, discrepancies in both theory and experiment still exist depending on the author, specially regarding certain mechanisms of excitation and recombination of carriers and light output characteristics.[20;21;22;23;24] This, possibly, is due to different growth and deposition methods of these electroluminescent materials (thick films, thin films, powder-based). Even though a thorough revision of the physics of ACEL devices is out of the scope of this thesis, it is necessary to briefly summarise some general concepts to help the reader to understand some of the upcoming contents.

In this thesis powder-based copper-doped zinc sulphide (ZnS:Cu) crystals, which were embedded in a binder resin to form a paste, were chosen as luminescent material. They are usually refered to as phosphors, since the luminescence mechanism is a type of phosphorecence. In the Figure 4.1a one can see the sandwiched structure of an ACEL device. Over a substrate, for instance glass, one deposits a TCF, which will simulta-

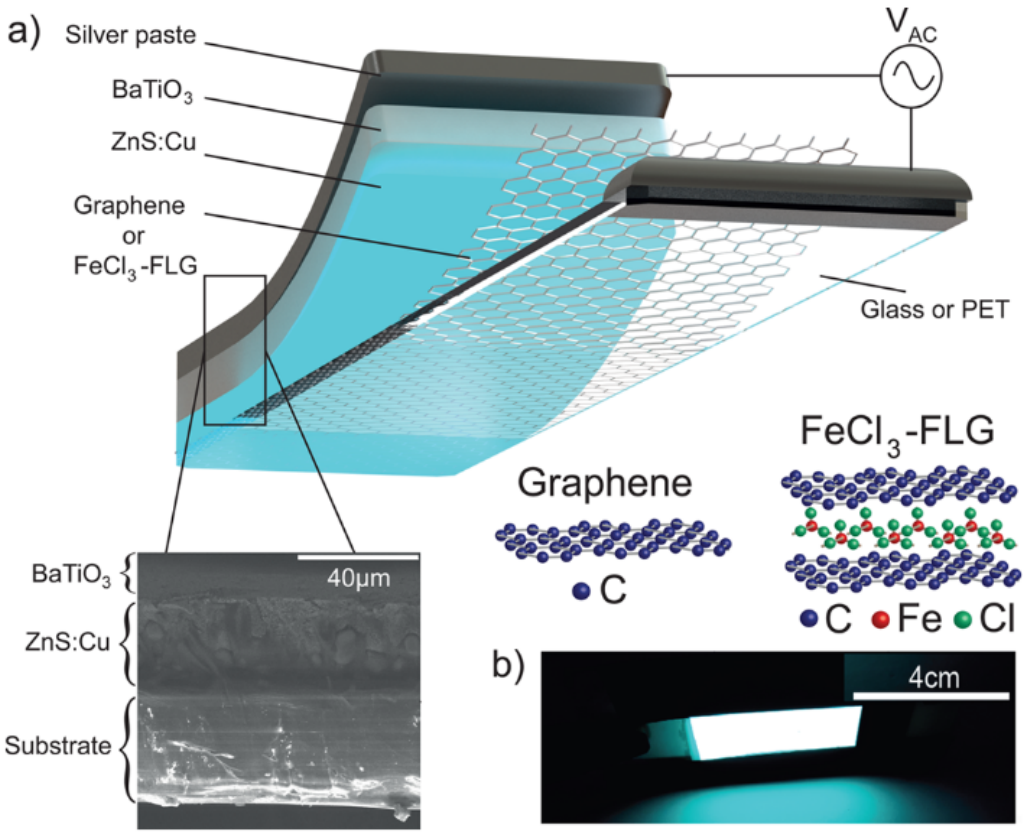

Figure 4.1: a) Schematic of a typical ACEL device, with an SEM cross-section of the device and a schematic of pristine FLG and $FeCl_3$-FLG sandwich structures. b) Photograph of a large-area device lighting up using $FeCl_3$-FLG electrodes.

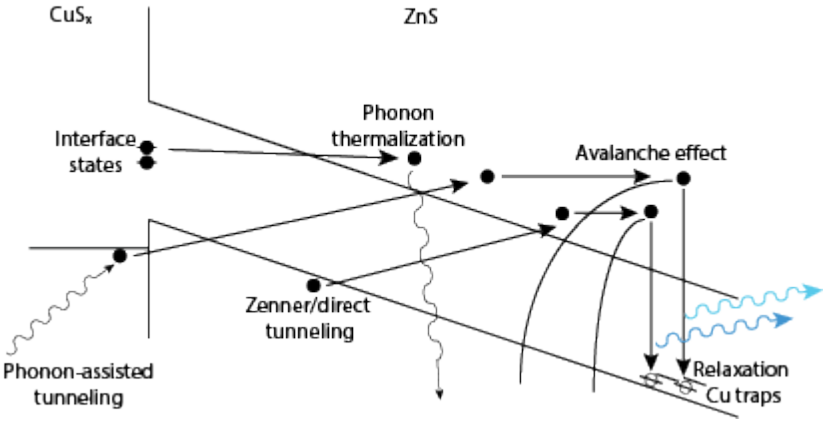

Figure 4.2: Schematic of the different excitation, recombination and scattering processes giving rise to light emission in ACEL

neosly contact the device while allowing light to be transmitted. The light-emitting layer of ZnS:Cu paste is deposited on top, and an insulating barium titanate ($BaTiO_3$) layer is also deposited, as seen in the scanning electron microscope (SEM) cross-section image. Since ACEL devices need high voltages for operation, inhomogeneities in the thickness of the ZnS:Cu layer may short the top silver paste and bottom $FeCl_3$-FLG electrodes; the $BaTiO_3$ essentially avoids this and prevents dielectric breakdown of the phosphor, enhancing device lifetime too.

The whole structure then behaves as a capacitor.[23] In the light-emitting layer, ZnS:Cu crystals of around 20 μm in size (whose size and packing density ultimately determines resolution) are seen embedded in a binder; this binder usually has a high dielectric constant, which enhances the field in the ZnS:Cu particles according to $E_{ZnS} = E_m[\frac{3\varepsilon_{r2}}{2\varepsilon_{r2}+\varepsilon_{r1}-\phi(\varepsilon_{r1}-\varepsilon_{r2})}]$, where E_m is the applied field, ε_{r1} and ε_{r2} are the dielectric constants of the ZnS and the binder respectively, and ϕ is the volume fraction of ZnS:Cu crystals within the binder.[3] With thicknesses of around 50 μm and voltage of 100 V, the electric fields achieved are in the order of $10^7 - 10^8$ V/m, enough to produce electroluminescence in the crystals, as shown in Figure 4.1b in a large-area device.

Why are such high fields needed to produce light-emission? In Figure 4.2 the light-emitting process is shown. The excitation mechanism in ZnS ($E_{gap} = 3.67$ eV) crystals is thought to be impact ionization or excitation.[20;23;24] The dielectric breakdown of zinc sulphide (ZnS) is between $10^7 - 10^8$ V/m, in the order of magnitude of the AC bias in

ACEL devices.[21] Needle-like structures of CuS_x that are formed within the ZnS matrix enhance the electric field with their sharp tips, concentrating it.[23;25] Under such large electric fields, highly energetic electrons can knock/scatter other electrons, promoting them from the valence to the conduction band, overcoming phonon thermalization in an avalanche-like excitation. These electrons may come from interface states, and Zenner tunneling and phonon-assisted tunneling across the bandgap. They would eventually recombine into the Cu traps, acting as recombination centres where light-emission is produced.[23;25;20;24;3]

The excitation with an AC field is then two-fold: first, it produces continuous light-emission, since a DC field would eventually fill all the Cu traps and eventually forbid emission; second, the whole structure behaves as a capacitor, thus a DC field would eventually polarise the device, quenching light-emission since the field across the capacitor would be reduced below the threshold for impact excitation and eventually become zero.[23;25;20;24;3]

Typical excitation frequencies are between 50 and 1000 Hz; the time windows have to be large enough (or frequencie low enough) to allow donor/acceptor-type electroluminescence. Decay times larger than this will not produce luminescence since they are not in phase with the AC field frequency, which will sweep away the carriers that have not recombined; this is actually one of the reasons why there are such few dopants that behave as luminescent centers.[3;20] Increasing the driving frequency would increase the brightness in the device until a point where the field switches too fast to allow efficient recombination. In general, sharper waveforms, faster frequencies and higher voltages will accelerate device degradation.[25]

An empirical relationship between light output (B) and voltage applied (V) was obtained by Alfrey and Taylor in the form $B = B_0 exp(\frac{-b}{\sqrt{V}})$, where B_0 and $-b$ are empiric constants related with the phosphor size and paste composition, layer thickness, etc.[22;20]. This is the so-called Alfrey-Taylor relationship, and usually the agreement with experimental data is very good.

4.3 SAMPLE FABRICATION

Usually, ACEL devices are created by means of screen-printing: the pastes are usually pushed through a mesh that contains a mask. This mask determines whether or not

the paste will go through, creating the patterns; the mesh size determines the thickness of the final printed layer. This method is not suitable when working with two dimensional (2D) materials because the mesh damages considerably the 2D electrode; also, variation in thicknesses across devices and batches makes a faithful characterization very difficult, since at such high voltages a small difference in layer thickness would mean a significative drop in voltage and thus in luminescence, given the exponential relationship between the two.

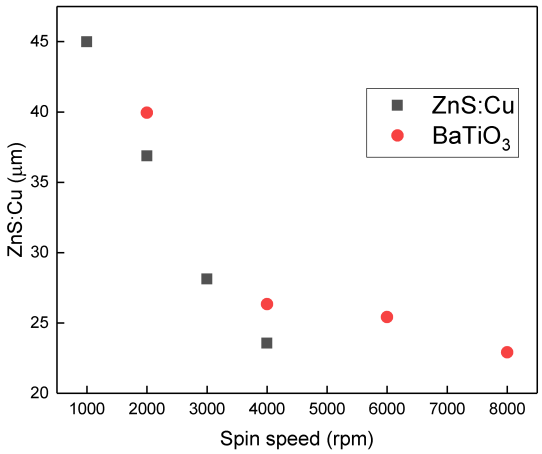

Figure 4.3: The different thicknesses of ZnS:Cu and $BaTiO_3$ pastes spun on glass.

For this reason, we chose spin-coating as a deposition technique. After successful transfer of SLG and FLG by poly(methyl methacrylate) (PMMA)-assisted wet-transfer and of $FeCl_3$-FLG by dry-transfer to glass or polyethylene terephthalate (PET), silver paint was used to contact the transparent electrode. PEDOT:PSS films were already deposited on the substrate when purchased. Then, ZnS:Cu and $BaTiO_3$ were spun on top. In Figure 4.3 the spin curves for ZnS:Cu and $BaTiO_3$ are shown; the spin speeds were 2000 *rpm* and 3500 *rpm* for ZnS:Cu and $BaTiO_3$ respectively to match the thicknesses recommended by the paste supplier. After every spinning step, the samples were cured in an oven at 120^oC for 10-15 minutes to remove solvents. Finally, the top electrode was silver painted, and the device finished.

SLG and FLG were produced and purchased respectively, as explained in Chapter 3. PEDOT:PSS stripes were purchased from Agfa.

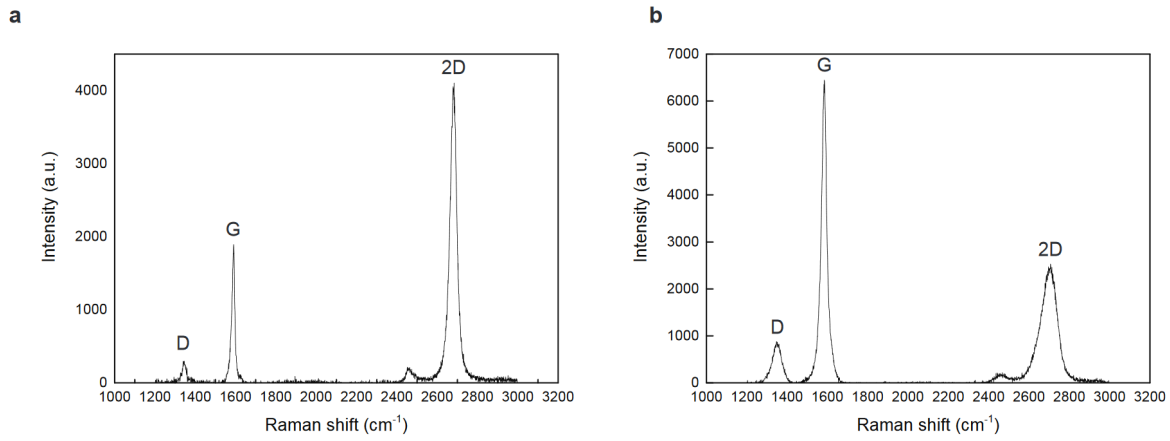

Figure 4.4: a) Raman spectrum of SLG. b) Raman spectrum of FLG

4.4 CHARACTERIZATION AND RESULTS

The characterization of the graphene was done by Raman spectroscopy. In the Figure 4.4a and Figure 4.4b the Raman spectra of SLG and FLG and are shown, with the characteristic $2D/G = 3$ and $2D/G = 0.45$ for SLG and FLG respectively.[26;18] In the case of FLG it is difficult to determine exactly the number of layers; previous studies in our group have established a range of 2-11 layers with an average of 4 in CVD Ni-grown films such as the ones used here.[27] In Figure 4.5a the Raman spectra of $FeCl_3$-FLG is shown, the multipeak G band characteristic of $FeCl_3$-FLG is shown in Figure 4.5b, with a strong signal from the G_2 component indicating strong p-type doping. Remarkably, all spectra present a small D band, which suggest high-quality films.[18;27;26]

In the Figure 4.6 the characteristics of $FeCl_3$-FLG versus pristine FLG devices are compared. The emission of these devices was collected from a 5 mm spot through a microscope objective, rastering the sample with a pitch of 5 mm to avoid overlap to obtain the total emission of the sample, and the spectra is then averaged. In the Figure 4.6, two emission spectrum are shown, where the $FeCl_3$-FLG electrode emits light 49% brighter than FLG at the peak emission of 495 nm. This is attributed to the lower sheet resistance (10 times smaller) of the $FeCl_3$-FLG electrode which drives power more efficiently; the resemblance between the two curves is due to flat optical transmittance of $FeCl_3$-FLG and FLG.[28;18] The four gaussian fittings in green represent the 4 components of the spectra ($\lambda = 438, 464, 497, 525\ nm$) from different states (Cu

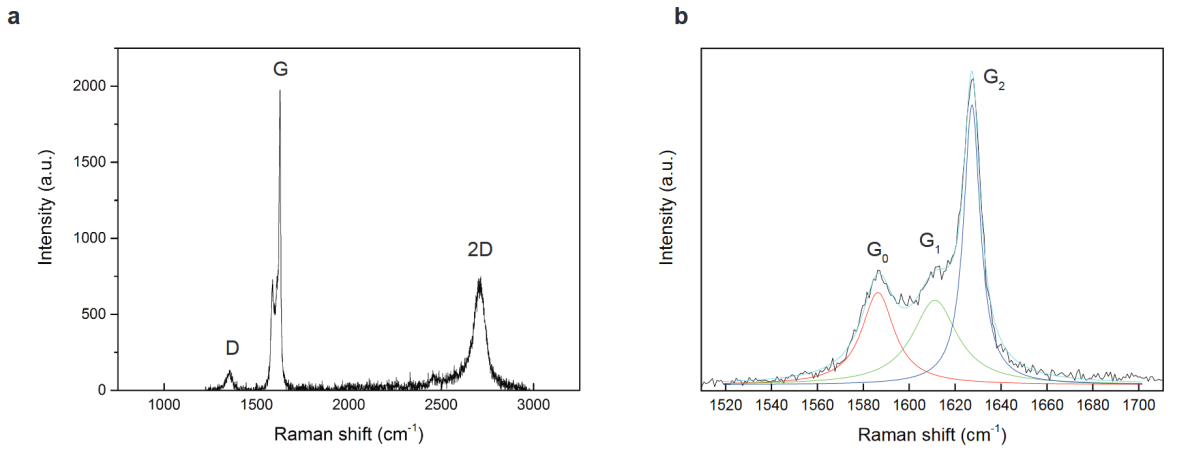

Figure 4.5: a) Raman spectrum of $FeCl_3$-FLG. b) Magnified view of the multi G peak of a), fitted with three Lorentzians corresponding with different doping stages.

impurities that might be either interstitial or superstitial, different oxidation states or even S vacancies...), as reported previously.[5] Broadening and shifts of these peaks is mainly due to variation in phosphor size and phase, as well as AC frequency.[5]

This difference is present across the whole range of voltages as seen in Figure 4.6b, confirming that this improvement is related to the electrode material; moreover, the greater the voltage the larger the difference is. This is due to the exponential behaviour of the light output with voltage according to the Alfrey-Taylor relationship $B = B_0 exp(\frac{-b}{\sqrt{V}})$.[21;20] In the Figure 4.6c the peak emission at 495 nm is plotted against the bias, and fitted with the Alfrey-Taylor relationship with very good agreement, highlighting the exponential dependence on the bias. This enhanced brightness is readily noticeable by visual inspection in the photograph in Figure 4.6d, where the $FeCl_3$-FLG device (right side) has a brighter and more homogeneous lighting than the FLG device (left side).

Two more large-area devices were built and characterised to confirm these findings; in the Figure 4.7 two emission spectrum of $FeCl_3$-FLG devices are compared against pristine FLG ones; the emission intensities measured are higher in $FeCl_3$-FLG than pristine FLG for all the 3 devices compared (the ones shown in Figure 4.6 and these two). The differences in emission in between the same kind of samples are thought to be due to different graphene qualities; even same pristine FLG devices have different intensities, despite being from the same graphene wafer sample. This would surely

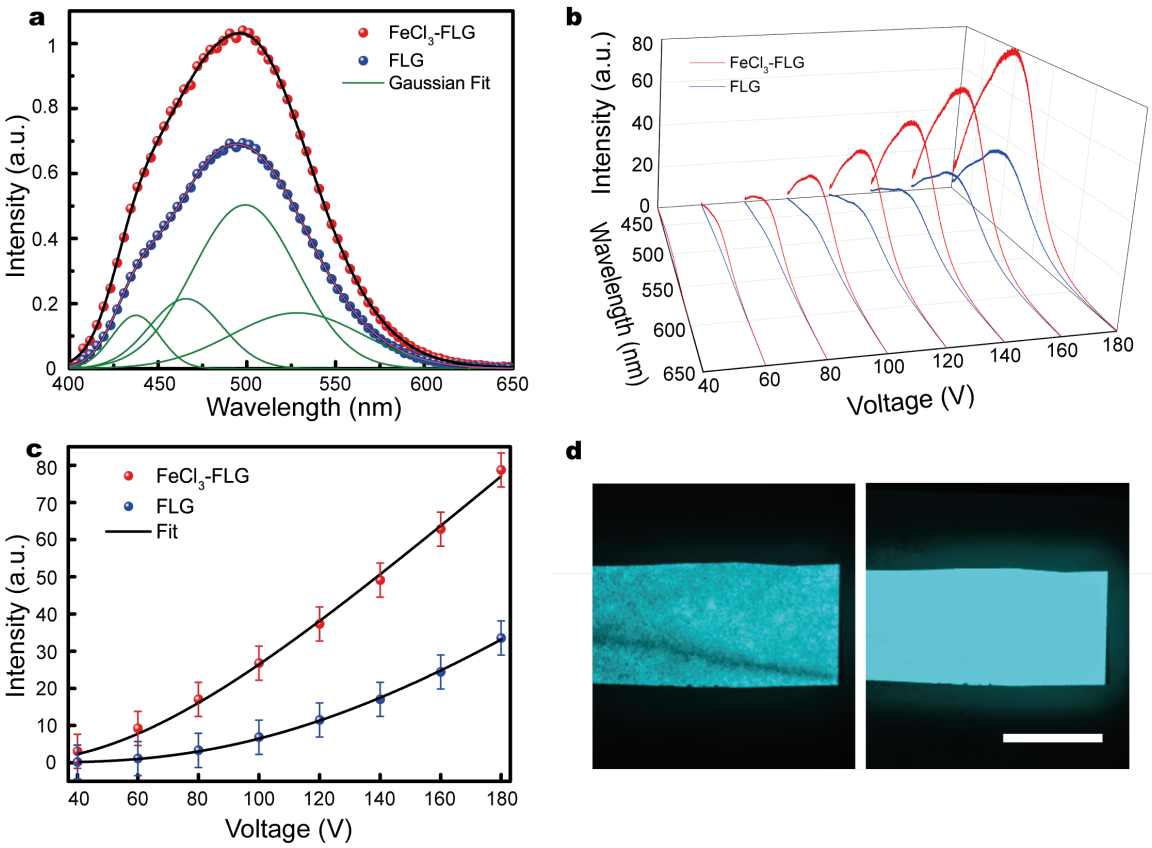

Figure 4.6: a) Emission in the visible of pristine FLG and $FeCl_3$-FLG devices. b) Emission in the visible of pristine FLG and $FeCl_3$-FLG devices at different voltages. c) Peak emission (495nm) for different voltages. The curves are fitted using the Alfrey-Taylor relationship. d) Photograph of pristine FLG (left) and $FeCl_3$-FLG (right) devices.

affect also the degree of $FeCl_3$ intercalation, and produce different light intensities too. However, looking at the graphs, it is clear that the intercalation with $FeCl_3$ renders brighter devices.

To assess the performance of these electrodes in large area panels, electrodes with high aspect ratios (30:1) were fabricated. The brightness gradient is ultimately related to the resistance of the electrode given by $R = R_s \frac{L}{W}$, where R is the resistance, R_s is the sheet resistance, and L and W are the length and width respectively; therefore reducing the width of the electrode will enhance the voltage drop across the device.

Pristine SLG, pristine FLG, $FeCl_3$-FLG and PEDOT:PSS, common flexible trans-

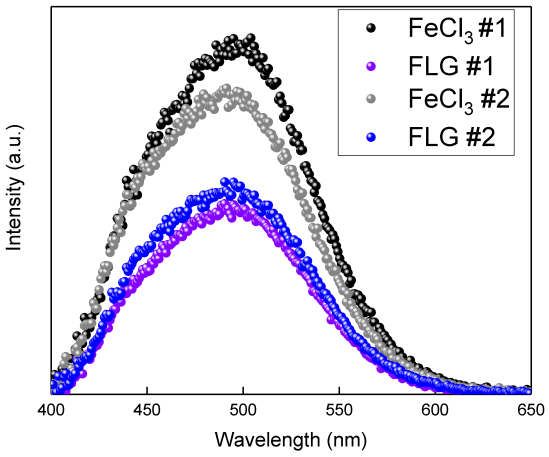

Figure 4.7: Batch characterisation of $FeCl_3$-FLG devices and pristine FLG devices. In all the devices fabricated, $FeCl_3$ intercalation renders brighter illumination.

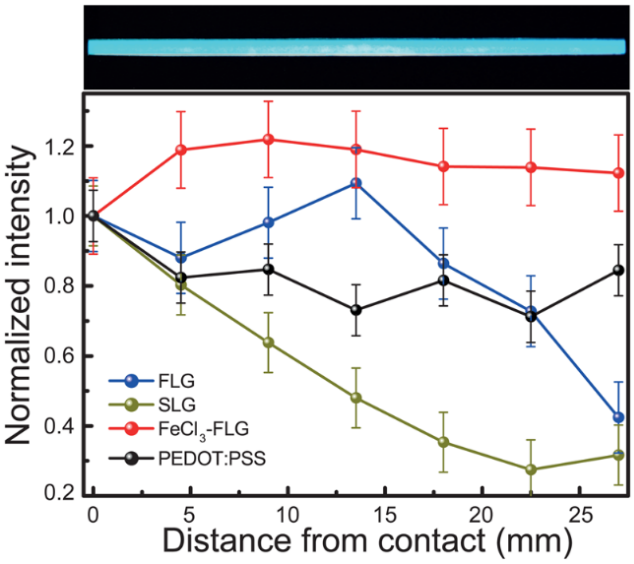

Figure 4.8: Brightness gradient of four materials: $FeCl_3$-FLG, FLG, SLG and PEDOT:PSS. The top image is a typical device for brightness gradient characterisation (1 *mm* width), made out of$FeCl_3$-FLG.

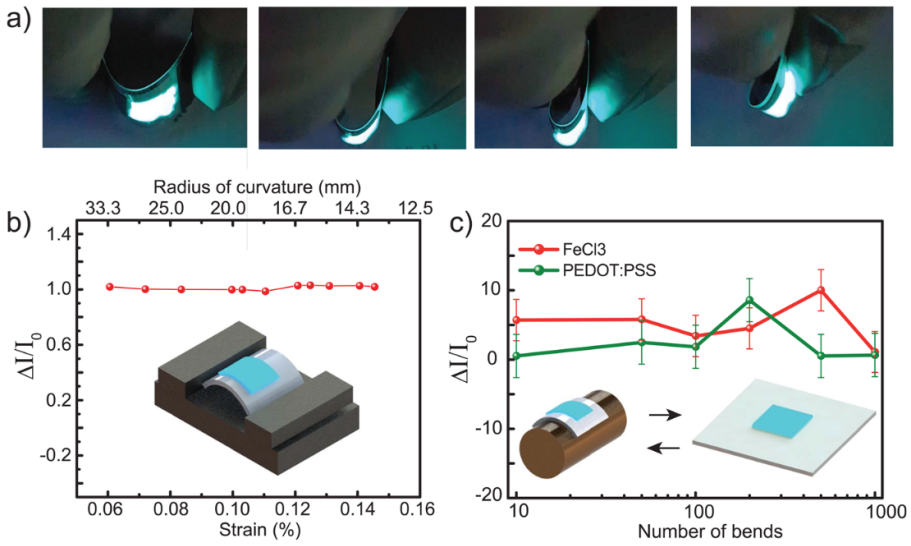

Figure 4.9: a) Sequence where a ACEL device with $FeCl_3$-FLG electrodes is bent and ultimately folded. b) Emission vs strain of a ACEL device with $FeCl_3$-FLG electrodes. c) Emission vs bending of two ACEL devices, with $FeCl_3$-FLG and PEDOT:PSS electrodes for comparison.

parent electrodes available nowadays with good mechanical properties, were used as TCF. In the Figure 4.8 the brightness is plotted along the distance of the electrode (starting from the contact to the electrode). The light intensity is normalised to this value; in this way, the different transparencies of the materials would be neglected and the true brightness gradient can be assessed.

The brightness gradient is related to the sheet resistance of the electrode as expected: the lowest sheet resistance corresponds to $FeCl_3$-FLG (20 Ω/sq), which shows negligible brighness gradient, and the highest sheet resistance (1 $k\Omega$/sq) corresponds to SLG, which shows the most dramatic drop in brightness along the distance.[27;29] From these results, it is clear that $FeCl_3$-FLG is an optimal electrode for large area panels.

As is mentioned above, one of the main characteristics of ACEL devices is their intrisic flexibility.[3;4] The flexibility of the devices can be readily assessed in the bending cycle shown in the photograph Figure 4.9a, where the device is increasingly strained until it is folded, without change in light emission. We then characterised the emission while the device is bent, using a custom-made holder, that can be fitted under the microscope so light can be collected while strain can be simultaneously changed; this

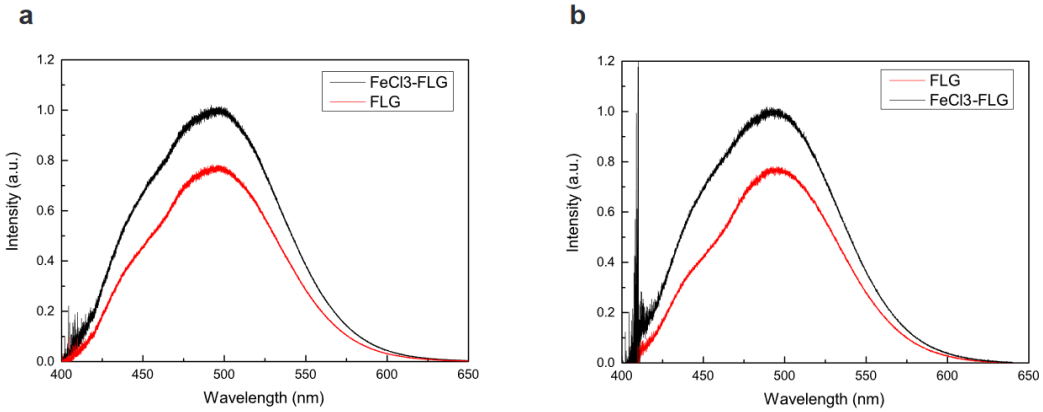

Figure 4.10: a) Emmission of $FeCl_3$-FLG and pristine FLG characterised after fabrication. b) Emmission of $FeCl_3$-FLG and pristine FLG characterised 2 months after fabrication.

is shown in Figure 4.9b. The device strain was calculated using the expression $\epsilon = z - 2d/2r$, where z is the distance of the surface from the neutral axis of the substrate ($\sim$0.14 mm), d is the substrate thickness ($\sim$0.28 mm) and r is the bending radius. In the Figure 4.9c, the light emission of the device was characterised against number of bends. Special attention was taken to collect the light from the same spot after the bending cycle. We compared this performance to that of PEDOT:PSS, a well known flexible TCF: the performance is the same for both. These results confirm the potential of $FeCl_3$-FLG also for flexible and foldable electronics.

$FeCl_3$-FLG has a well-known stability under harsh environments, where high (873 K) or low (30 mK) temperatures or high humidity are present.[30]. However, little is known about the stability of this material in devices; possible $FeCl_3$ de-intercalation may occur when in touch with the phosphor solvents, or after repeated large current flow.

This, however, is not the case for $FeCl_3$-FLG. In the Figure 4.10 emission of a pristine FLG was used as a reference to compare the intensity of a $FeCl_3$-FLG device over time. In the Figure 4.10a the emission is taken after device fabrication, and in the Figure 4.10b the emission is taken 4 months after device fabrication; both plots are identical, showing no change in emission, which confirms the long-term stability of $FeCl_3$-FLG also when used in devices under high voltage operation.

4.5 CONCLUSIONS

The results presented here show the potential of $FeCl_3$-FLG as a TCF for the first time, in a real application. It is shown how the intercalation with $FeCl_3$ molecules in graphene films produces more conductive films and thus a brighter light emission in ACEL devices than with pristine FLG. Also, we demonstrate that these $FeCl_3$-FLG electrodes do not suffer from dramatic brightness gradients due to their very good conductivity unlike most of the emerging flexible TCF. Moreover, its flexibility and mechanical resilience was tested, and found to be highly flexible, thus suitable for the next generation of flexible optoelectronic devices and displays.

BIBLIOGRAPHY

[1] D. Akinwande et al. Two-dimensional flexible nanoelectronics. *Nature Communications*, 5, 2014.

[2] A. K. Yetisen et al. Nanotechnology in textiles. *ACS Nano*, 10, 2016.

[3] M. Bredol et al. Materials for powder-based AC-electroluminescence. *Materials*, 3, 2010.

[4] Z-G. Wang et al. Flexible graphene-based electroluminescent devices. *ACS Nano*, 5, 2011.

[5] A. Brigida et al. Spectroscopic characterisation of alternate current electroluminescent devices based on ZnS:Cu. *Journal of Alloys and Compounds*, 341, 2002.

[6] Yu. P. Chukova. Electroluminescent capacitors as systems with distribution parameters. *Journal Applied Spectroscopy*, 7, 1967.

[7] K. Alzoubi et al. Bending fatigue study of sputtered ITO on flexible substrate. *Journal of Display Technology*, 7, 2011.

[8] S T. Lee et al. Metal diffusion from electrodes in organic light-emitting diodes. *Applied Physics Letters*, 75, 1999.

[9] T. Nagata et al. Effect of UV–ozone treatment on electrical properties of PEDOT:PSS film. *Organic Electronics*, 12, 2011.

[10] U. Lang et al. Mechanical characterization of PEDOT:PSS thin films. *Synthetic Metals*, 159, 2009.

[11] M Jørgensen et al. Stability/degradation of polymer solar cells. *Solar Energy Materials and Solar Cells*, 92, 2008.

[12] M. S. Tyler et al. High-performance silver window electrodes for top-illuminated organic photovoltaics using an organo-molybdenum oxide bronze interlayer. *ACS Applied Materials & Interfaces*, 8, 2016.

[13] O. S. Hutter et al. A hybrid copper:tungsten suboxide window electrode for organic photovoltaics. *Advanced Materials*, 27, 2015.

[14] Z. Wu et al. Nanowire failure: Long = brittle and short = ductile. *Nano Letters*, 12, 2012.

[15] D. S. Hecht et al. Emerging transparent electrodes based on thin films of carbon nanotubes, graphene, and metallic nanostructures. *Advanced Materials*, 23, 2011.

[16] H. H. Khaligh et al. Failure of silver nanowire transparent electrodes under current flow. *Nanoscale Research Letters*, 8, 2013.

[17] C. Schrage and S. Kaskel. Flexible and transparent SWCNT electrodes for alternating current electroluminescence devices. *ACS Applied Materials & Interfaces*, 1, 2009.

[18] I. Khrapach et al. Novel highly conductive and transparent graphene-based conductors. *Advanced Materials*, 24, 2012.

[19] J. Jiang et al. Intercalation doped multilayer-graphene-nanoribbons for next-generation interconnects. *Nano Letters*, 17, 2017.

[20] W. W. Piper et al. Electroluminescence of single crystals of ZnS:Cu. *Physical Review*, 87, 1952.

[21] W. W. Piper et al. The mechanism of electroluminescence of zinc sulphide. *British Journal of Applied Physics*, 6, 1955.

[22] G. F. Alfrey et al. Electroluminescence in single crystals of zinc sulphide. *Proceedings of the Physical Society. Section B*, 68, 1955.

[23] W. Kaiser et al. Light emission of electroluminescent lamps under different operating conditions. *2012 IEEE Industry Applications Society Annual Meeting*, 2012.

[24] E. Bringuier. Impact excitation in ZnS-type electroluminescence. *Journal of Applied Physics*, 70, 1991.

[25] S. Medling et al. Local degradation of electroluminescent emission centers in ZnS:Cu,Cl phosphors. *Journal of Luminescence*, 134, 2013.

[26] L. M. Malard et al. Raman spectroscopy in graphene. *Physics Reports*, 473, 2009.

[27] T. H. Bointon et al. Large-area functionalized CVD graphene for work function matched transparent electrodes. *Scientific Reports*, 5, 2015.

[28] R. R. Nair et al. Fine structure constant defines visual transparency of graphene. *Science*, 320, 2008.

[29] X. Li et al. Transfer of large-area graphene films for high-performance transparent conductive electrodes. *Nano Letters*, 9, 2009.

[30] D. J. Wehenkel et al. Unforeseen high temperature and humidity stability of $FeCl_3$ intercalated few layer graphene. *Scientific Reports*, 5, 2015.

5

GRAPHENE-BASED LIGHT-EMITTING DEVICES ON TEXTILE FIBRES

5.1 MOTIVATION

Textile electronics are attracting a lot of interest due to the possibility of embedding electronic devices and applications in everyday clothing. However, the concept of textiles itself is not only restricted to fashion or garments, and new combinations of materials are employed to add new meaning to smart textiles and satisfy the increasing demand for these kind of applications. This results in new devices that span from military applications to biometric markers and sensing for healthcare purposes, or even industrial packaging and automotive textiles.

Light-emitting devices will surely be a cornerstone within these novel technologies; they will be manufactured for leisure purposes, advertising or displaying of information, and they must be lightweight, flexible, unnoticeable and comfortable. The incorporation of displays and antennas in clothes for geo-positioning could help young and elderly people on their daily commute, or garments that change color for security alert within harsh environments and for light-therapy are only a few examples of the possibilities that some of these wearable devices will allow in the upcoming future.[1] Also, the production of these smart textiles must be cost-effective, and compatible with the existing techniques and approaches that are used in the current textile production lines; failure to do so will inevitably delay their introduction into the mass market and raise their cost, being this of higher importance than functionality within the clothing industry.

Various examples of light emitting devices on textile fibres have been realized with different types of electrode materials: indium tin oxide (ITO), carbon nanotubes

(CNT), nanowires (NW) or polymers;[2;3;4;5;6;7;8;9] most of them have been reviewed in the previous chapter.

As was already mentioned, ITO is known to be brittle: its sheet resistance increases dramatically upon bending, and also its deposition requires of temperatures not compatible with textile processing.[10] CNT suffer from the difficulties in producing either single metallic or semiconducting tubes and their high resistance.[11;12] NW are prone to breakage due to stress induced electromigration and destruction at moderate current.[13;14] Ionic liquids, despite their exceptional stretchability, suffer from limited stability.[15;16] There have been examples using poly(3,4-ethylenedioxythiophene) polystyrenesulfonate (PEDOT:PSS) on textile fibres for light-emitting devices, but in this case the PEDOT:PSS was printed as many as 6 times, which increases material and time consumption, rendering poor transparency and non-uniform luminescence;[17] to this, one should add that PEDOT:PSS does not withstand well ultraviolet radiation and has limited environmental stability.[18;19;20]

Overall there is not an optimal transparent conductor in the market that satisfies all the demands for wearable optoelectronics. In addition, most of the architectures require several deposition and/or processing steps which make them difficult to scale up to mass production, some of them require fibers which are not readily compatible with the clothing industry, or the devices are glued or mounted onto the fibers, not truly embedded.[2;5;7]

Lastly, when depositing these materials there are intrinsic problems related with the textile fibres themselves and the way they are manufactured, due to their microscopic roughness and surface properties, especially when the required thickness approaches the nanoscale. Some of the components and layers of modern organic light-emitting diodes (OLED) and photovoltaics (PV) have dimensions of tens of nm; these thicknesses are incompatible with roughness values in the μm scale.

Recently graphene's potential to be a transparent flexible electrode for polymeric textile fibres has been explored by our group.[21;22] In this chapter, few-layer graphene (FLG) is transferred onto monofilament polypropylene (PP) fibres. PP one of the most common polymers employed in the textile industries because it is the lightest among all the commodity plastics, used for a myriad of applications such as protective packaging, parachutes, cleansuits and waterproof clothing.[23] This is especially important in aerospace technologies and transport of goods, where the payload trade-off is crucial. It

Figure 5.1: Picture of a extrusion head for polymeric fibres.

also withstands the most common solvents and its melting temperature (160^{o}C) allows baking processes for lithography or solvent evaporation.

FLG is chosen due to its much better electrical conductivity (order of ∼100s Ω/sq) and mechanical properties than those of graphene.[24;25] Also, due to its organic nature it should not present any incompatibility with the human body or skin, which is necessary for human applications. This FLG has been used for transparent electrodes powering alternating-current electroluminescence (ACEL) devices on PP fibres. As mentioned in the previous chapter, ACEL is an established technology for large-area, flat and flexible light-emitting applications available nowadays.[26] These light-emitting devices are created by spin coating, but the method possesses potential compatibility with screen-printing and roll-to-roll (R2R) processes. Also, possible encapsulation is readily available due to the planar nature of the materials and the resulting device.

In the previous chapter, the physics of ACEL devices have been already introduced. Since the light-emitting fibres have the same structure and perform under the same physical principles, the reader is kindly referred to the previous chapter for that aspect.

5.2 POLYPROPYLENE FIBRES

PP is the second most produced commodity plastic in the world; the market for PP in 2016 for flexible packaging demanded 16.77 million tonnes.[27] A thermoplastic usually molded by injection, it was first polymerised in 1954. Yarns of this polymer can be made by extruding the melted PP through a slit, creating a ribbon, or through a "shower

head" as shown in Figure 5.1. These fibres are then joint together to produce the final yarn before cooling down.[23] This production method renders fibres which usually have roughnesses in the μm scale, which makes it difficult to integrate electronic devices with them.

As mentioned in the introduction, PP fibres have many good features. They are produced from inexpensive and abundant raw materials and resins, with an straightforwards process; this results in low cost of production. Due to their chemical composition, PP is very hydrophobic due to the dense packing of polymer chains and lack of polar chemical groups; it absorbs very little water (∼0.1% at 65 % relative humidity (RH)), less than nylon and polyester.[23] It is also inert to chemicals including acids, alkalis and many organic compounds. Fibres made out of PP possess high ductility and high mechanical strength and iare neither toxic nor a good host for bacteria.[23] All these attributes have made PP a basic material within the textile industry at all levels.

For something to be considered as a textile fibre, it needs to have a length of at least a hundred times its diameter or width. The fibres need to be able to make a fabric/tissue by interlacing methods such as weaving, knitting, etc.[23] Rolls of PP tapered yarns of 2.5 mm width were provided by CenTex in Belgium, where they were manufactured according to the standards of the industry. This ensured the raw material/substrate the devices would be built on already met the requirements in terms of fibre production.

5.3 SAMPLE FABRICATION

The sample fabrication process is the same as that explained in the previous chapter. CVD-grown FLG graphene is transferred using the standard poly(methyl methacrylate) (PMMA)-assisted wet transfer. Prior to this transfer, the PP fibres were exposed to O_2 plasma through reactive ion etching (RIE) to increase their hydrophilicity.[28] This turned out to be a critical step to achieve a 100 % yield in the graphene transfer. A spin-coating curve calibration (see Figure 5.2) to match the paste thicknesses was performed; the difference in thicknesses between de fibre and the glass is probably due to different roughness and surface energies between the PP fibres and standard glass.

For patterning of the electrode, standard optical lithography (OL) is performed, and then O_2 RIE step is realised for pattern transfer; this is done at low power (50 W)

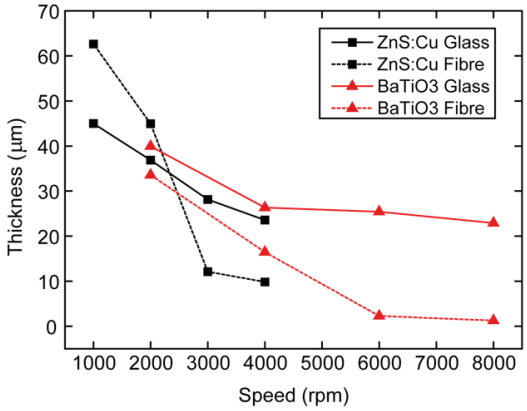

Figure 5.2: Spin-coating curves for the two ACEL pastes, spun on fibres and glass for comparison.

to prevent photoresist (PR) cross-linking. Once the graphene is patterned, the sample is immersed in acetone to remove the PR. Subsequently, the graphene electrode is contacted with silver paint and then device is built through spin-coating of the ACEL pastes.

The advantage of this approach is that the graphene transfer occurs after the fibre is manufactured so no change in the production lines is required, which might hamper the development of smart textiles.[29]

5.4 CHARACTERIZATION AND RESULTS

The fibre reels and fibres with three different widths, ranging from 2.5 mm down to 500 μm can be seen in Figure 5.3a. To assess the microscopic roughness of the fibre, we performed contact profilometry to obtain surface topography profiles of the fibre in the X and Y axis, which are shown in Figure 5.3b together with an optical microscope picture. The root mean square (RMS) of the surface roughness of the bare fibres (where X is the length of the fibre and Y is its width) are 311 and 722 nm respectively. This large difference between X and Y axis of the fibres is due to the extrusion direction of the fibres, along the X axis; this is a major difference between truly polymeric textile fibres, extruded in a manufacturing line, and other approaches rendering prototypes where the morphology of the substrate is uniformly smooth. Moreover, this roughness makes it virtually impossible to deposit any other material at the nanometre range;

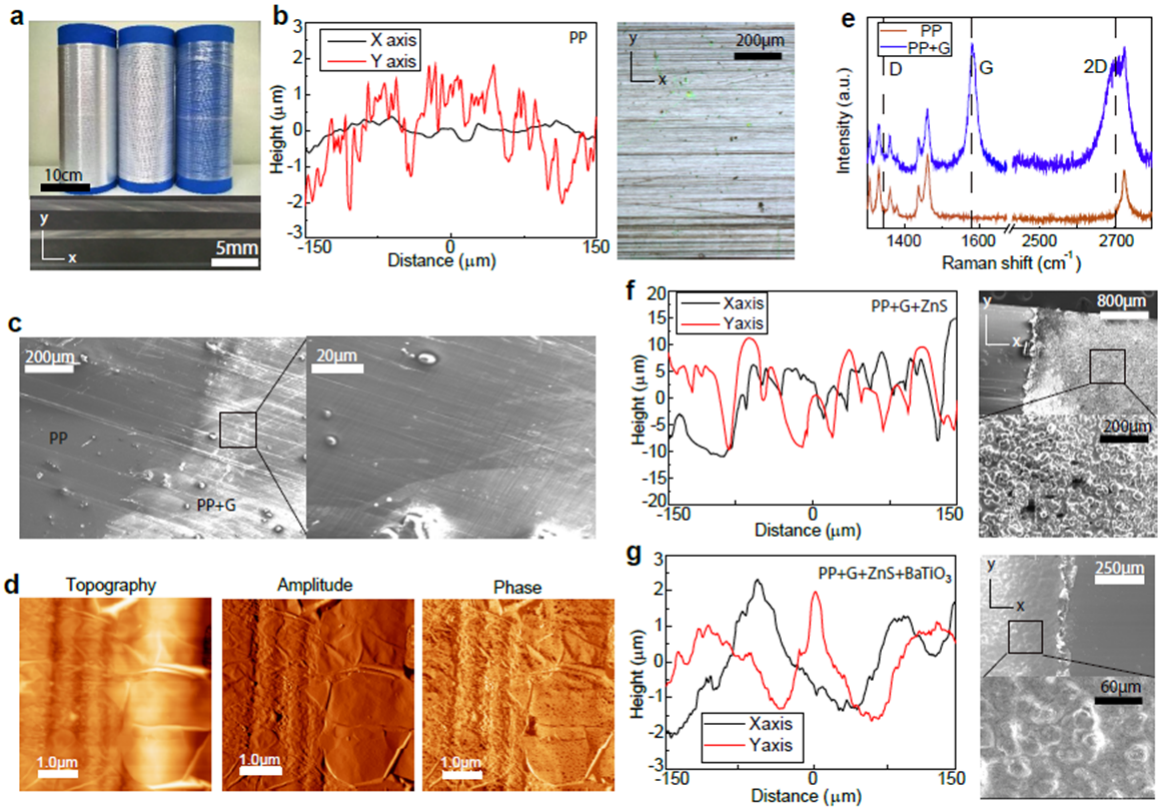

Figure 5.3: a) The reels as supplied by the manufacturer. Bottom picture shows PP fibres with three different widths. b) Surface profile along the X and Y axis, and optical microscope picture of a fibre. c) SEM pictures of a PP fibre coated with FLG. d) AFM topography, amplitude and phase maps. e) Raman spectrum of a bare fibre and a graphene-coated fibre. f) Surface profile of a fibre coated with ZnS:Cu paste and SEM picture. g) Surface profile of a fibre coated with ZnS:Cu and $BaTiO_3$ and corresponding SEM picture

this implies that for instance, when evaporating 50 nm of Au, this roughness would make obtaining a continuous, homogeneous and conductive layer impossible or, at least very challenging. For instance, transfer of iron-chloride intercalated few-layer graphene ($FeCl_3$-FLG) was attempted, as it seemed an obvious choice of transparent conductive film (TCF); however, due to the transfer method involved (tape-assisted dry transfer) and the high roughness of the fibres, the transfer of $FeCl_3$-FLG onto the fibres was not succesful as it was impossible to obtain a continuous $FeCl_3$-FLG layer due to low adhesion, and wet-transfer method was chosen as transfer process. This process allows for graphene to acomodate the high roughness of the fibre, making it conductive.

Even though the values for surface roughness are large (much larger than typical values of surface roughness in glass or polyethylene terephthalate (PET) substrates[30]), the coverage of the fibres is good and continuous, as seen in the scanning electron microscope (SEM) pictures in Figure 5.3c, where the brighter side corresponds to the graphene-covered one. The nanoscale coverage is evaluated with topography, amplitude and phase atomic force microscopy (AFM) maps of 4×4 μm; the full, continuous coverage of the fibre with graphene is shown in Figure 5.3d, and clean from residual PMMA.

This is further confirmed in the Raman spectra in Figure 5.3e, where PP fibres with (bottom panel) and without (top panel) graphene are shown. It is clear the presence of the G peak and 2D peak at ∼1580 cm^{-1} and ∼2700 cm^{-1} respectively, the intensity ratio I_G/I_{2D}= 1.05 and the width of the 2D peak W_{2D} ∼70 cm^{-1} are signatures of FLG. One cannot distinguish the D peak at 1350 cm^{-1} from the PP background signal, suggesting that the graphene film contains little defects. Also, the PP peaks remain unaltered, which suggests that no chemical interactions exist between the PP, graphene and the solvents employed in the transfer process.

The topography profiles after copper-doped zinc sulphide (ZnS:Cu) and barium titanate ($BaTiO_3$) on top of ZnS:Cu are shown in Figure 5.3f,g respectively. The RMS of the surface roughness for ZnS:Cu is 10.780 μm (X axis) and 7.778 μm (Y Axis) and for $BaTiO_3$ are 4.364 μm (X axis) and 3.517 μm (Y axis). These values agree quite well with the SEM pictures of ZnS:Cu and $BaTiO_3$: in Figure 5.3f the ZnS:Cu crystals, about 20 μm size, can be clearly seen; the RMS roughness agrees quite well with the radii of the crystals. In Figure 5.3g the $BaTiO_3$ covers the crystals, smoothing out the surface in good agreement with the lower value of surface roughness, and blurring the

image due to its insulating properties.

In Figure 5.4a a sketch of an ACEL device on a fibre is shown. Three devices with different widths can be seen lightning up in Figure 5.4b upon application of 100V AC. The emission spectra for the different ZnS:Cu thicknesses is shown in Figure 5.5c. The maximum value is achieved for a thickness of 47 μm, approximately equal to the supplier's recommendations (40 μm). The slightly lower emission for 62 μm thickness is probably due to slightly lower voltage drop across the ZnS:Cu layer; the emission of 22 μm and 10 μm are lower due to a lower density of ZnS:Cu crystals. The voltage dependence is shown in Figure 5.4d and fitted with the Alfrey-Taylor relationship $B = B_0 exp(-b/V)1/2$ with good agreement (R^2=0.9982).[26;31]

The mechanical resilience of the device is then studied, in the form of bending and torsion tests as seen in Figure 5.4e. The change in emission in the three cases analyzed here (emission while strained, emission after bending and emission after torsion) is normalized to that of the pristine device. Different devices where used for each individual test. In Figure 5.4f the change in emission while the device is strained through bending is shown, with no change when the device is bent well below 10 mm radius. Neither in Figure 5.4g where the change in emission versus number of bents is shown, nor in Figure 5.4h where the change in emission when the device affected by torsion is plotted, a deviation from the original pristine value is observed after 2000 bents. The measurement is performed as shown in the insets: the device is bent first and then measured flat. The strain and bending radii tested are such that demonstrate the resilience to mechanical stresses and thus feasibility of these devices for textile and wearable applications; for instance, a bending radius of 10 mm is approximately equal to that of an human finger radius on average.

Within the semiconductor processing techniques, patterning and pattern-transfer are among the most important ones; every electronic device is built with a combination of patterning and etching. So being able to perform such techniques in textile fibres will indeed open the path for wearable electronics more rapidly due to the compatibility of the processes. Given this perspective, we used conventional OL and RIE to pattern the graphene electrode in a desired shape, being able to write "EXETER CfGS" (EXETER Centre for Graphene Science) in both in negative and positive contrast, as seen in Figure 5.5a, with patterned features as small as 100 μm. OL and RIE are standard techniques for patterning and pattern-transfer within the semiconductor industry, even compatible

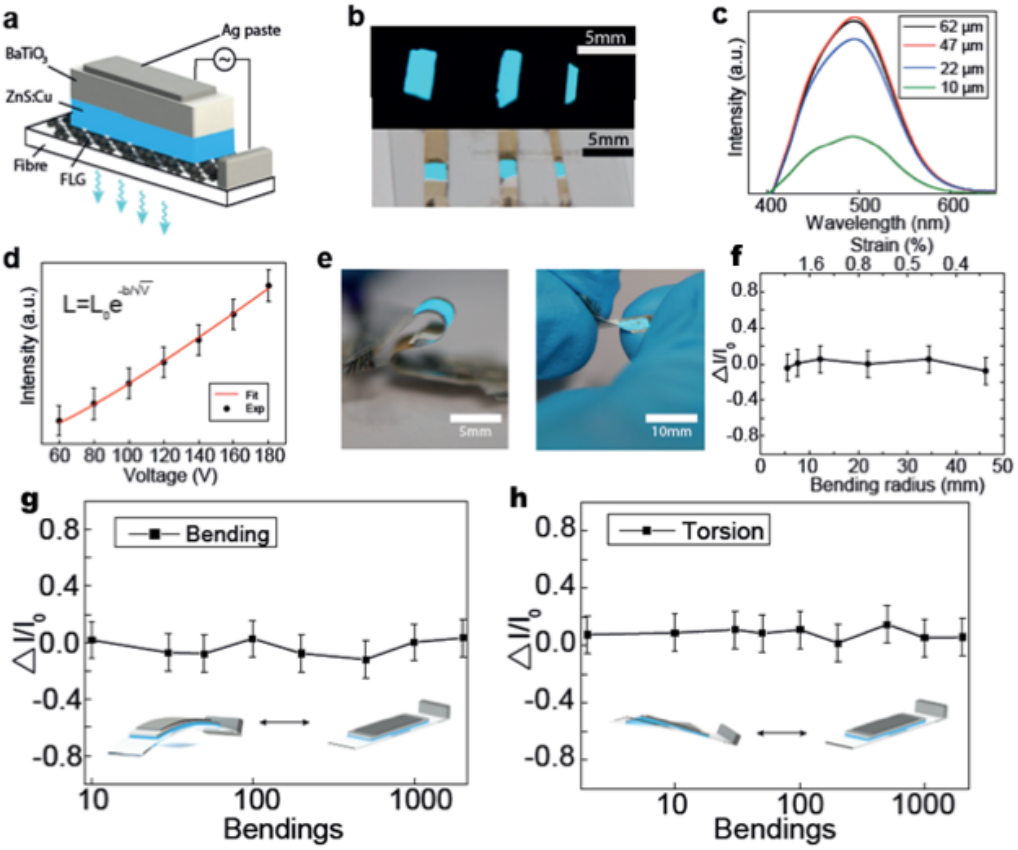

Figure 5.4: a) Sketch of the device structure. b) Three devices lightning up with three different widths. c) Emission for four different ZnS:Cu paste thicknesses. d) Emission as a function of voltage and fit to the Alfrey-Taylor relationship. e) Photographs of the fibres being bent and twisted. d) Normalised change in emission versus bending radius. f) Normalised change in emission versus number of bendings. g) Normalised change in emission versus number of twists.

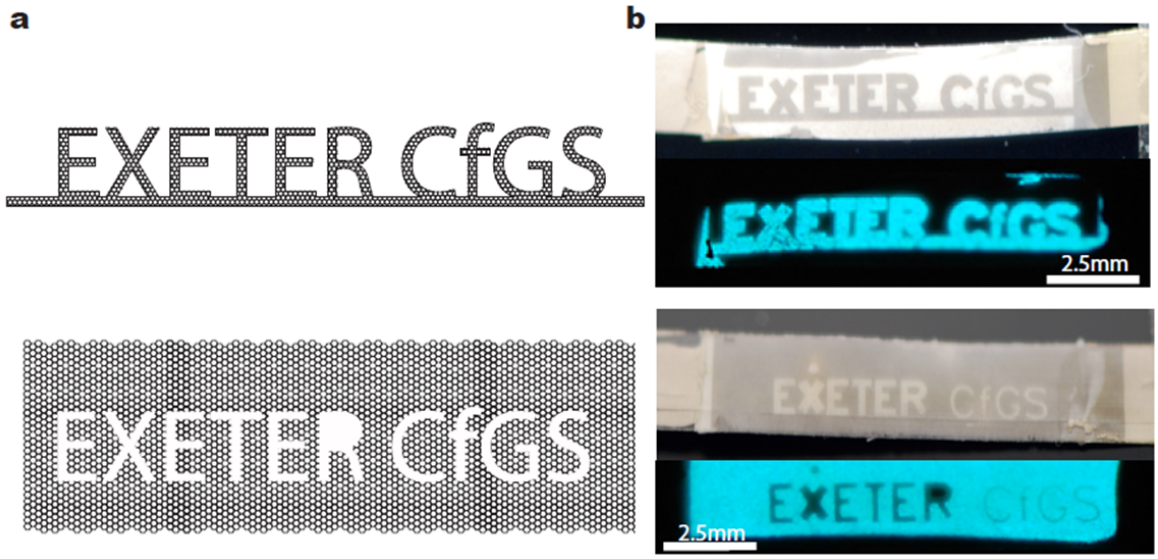

Figure 5.5: a) Positive (top) and negative (bottom) patterning of a graphene electrode. b) Patterned ACEL device on fibres, showing positive (top) and negative (bottom) configurations.

with R2R processes for mass production. On top of the patterned graphene, one can build an ACEL device as shown earlier. In Figure 5.5b one can see both negative and positive patterns in actual ACEL devices, and emitting light upon application of 100 V AC. For the purpose of displaying information or signaling, this is a technique that can be readily implemented within the industry standards.

Finally, we create some arrays of light-emitting fibres, demonstrating their potential to become large-area textile displays. Figure 5.6a shows an approach to create such arrays, where the fibre is contacted on the rear electrode with other fibre coated with silver paint. This allows to create arrays with large-area pixels ($\sim$6 mm^2); these pixels are homogeneously illuminated and their shape is given ultimately by the rear Ag contact. The creation of individual pixels endows the arrays much versatility in display uses. These arrays are robust and highly flexible as shown in Figure 5.6a.

However, with this approach it is difficult to scale down the size of the pixels. To overcome this difficulty, we manufactured a different array shown in Figure 5.6b: one of the fibres is coated with graphene solely and a silver-painted contact, while the other one is coated with ZnS:Cu, $BaTiO_3$ and Ag paste. When they are put on top

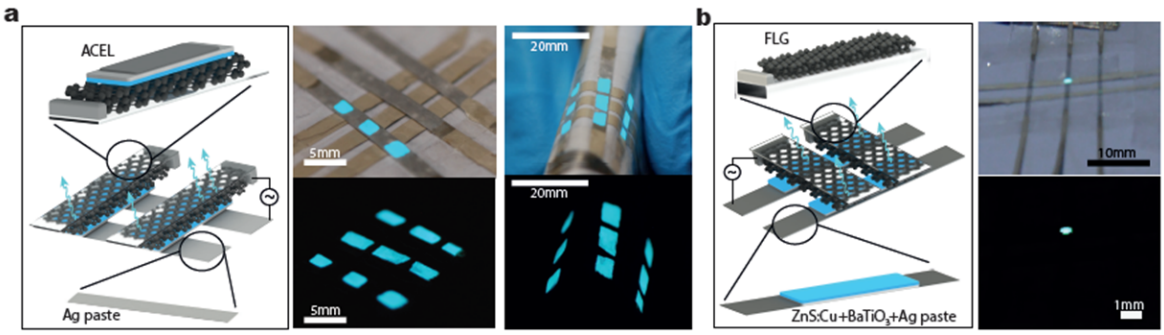

Figure 5.6: a)Schematic of the device structure for large pixel (left), and photographs of the structure lighting up and being bent in both dark and bright environment. b) Sketch of the device structure for small pixels. Photograph of the device lighting up in both light and dark environment.

of each other, the graphene contacts the ZnS:Cu, closing the circuit and producing the light emission, with a pixel size of merely $\sim$0.25 mm^2. This approach is not as mechanically robust as the previous one due to need of full contact of the graphene with the ZnS:Cu layer, but that could be solved with some encapsulation that ensures appropriate contact between the graphene and the ZnS:Cu layer.

As a remarkable feature of these arrays, and in contrast to previous works when the functionality is added once the textile array is manufactured, our textile fibres have the functionality already in them prior to the creation of the array. This widens the possibilities of such wearable electronics and helps the integration of these materials into established textile workflows.

5.5 CONCLUSIONS

In summary, it is shown that polymeric textile fibres can be coated with FLG to create for the first time graphene-based ACEL devices on polymeric textile fibres. FLG is transferred with a good, large-area coverage and its resistivity allows for bright and uniform luminescence; these results show the versatility and potential of graphene to become the standard transparent electrode in wearable electronics.

It is also demonstrated that FLG is resilient to mechanical stresses similar to those that would experience when worn in actual clothes, and its feasibility for TCF in light-

emitting textile devices. The patterning of these fibres is done with easy, scalable processes already being widely used in the industry such as OL and RIE, and may be compatible with established techniques such as screen-printing and the emerging R2R processing. This is not only of importance for the possibility of information display with these light-emitting devices, but truly paves the way for these techniques to be exported from the semiconductor to the textile industry.

BIBLIOGRAPHY

[1] S. R. Feldman. Psoralen plus ultraviolet light phototherapy effectiveness. *Journal of the American Academy of Dermatology*, 63, 2015.

[2] H. Yang et al. Light-emitting coaxial nanofibers. *ACS Nano*, 6, 2012.

[3] W. Seung et al. Nanopatterned textile-based wearable triboelectric nanogenerator. *ACS Nano*, 9, 2015.

[4] S. Choi et al. Highly flexible and efficient fabric-based organic light-emitting devices for clothing-shaped wearable displays. *Scientific Reports*, 7, 2017.

[5] E. Nilsson et al. Energy harvesting from piezoelectric textile fibers. *Procedia Engineering*, 87, 2014.

[6] K. Cherenack et al. Woven electronic fibers with sensing and display functions for smart textiles. *Advanced Materials*, 22, 2010.

[7] J. Wang et al. Highly stretchable and self-deformable alternating current electroluminescent devices. *Advanced Materials*, 27, 2015.

[8] M. Hamedi et al. Towards woven logic from organic electronic fibres. *Nature Materials*, 6, 2007.

[9] B. O Connor et al. Fiber shaped light emitting device. *Advanced Materials*, 19, 2007.

[10] C-H. Lim et al. Mechanical and electrical stability indium-tin-oxide coated polymer substrates under continuous bending stress condition. *Journal of International Council on Electrical Engineering*, 2, 2012.

[11] C. Schrage et al. Flexible and transparent swcnt electrodes for alternating current electroluminescence devices. *ACS Applied Materials & Interfaces*, 1, 2009.

[12] J. W. G. Wilder et al. Electronic structure of atomically resolved carbon nanotubes. *Nature*, 391, 1998.

[13] J. Zhao et al. Electrical breakdown of nanowires. *Nano Letters*, 11, 2011.

[14] H. H. Khaligh et al. Failure of silver nanowire transparent electrodes under current flow. *Nanoscale Research Letters*, 8, 2013.

[15] S. Chowdhury et al. Reactivity of ionic liquids. *Tetrahedron*, 63, 2007.

[16] K. J. Baranyai et al. Thermal degradation of ionic liquids at elevated temperatures. *Australian Journal of Chemistry*, 57, 2004.

[17] B. Hu et al. Textile-based flexible electroluminescent devices. *Advanced Functional Materials*, 21, 2011.

[18] U. Lang et al. Mechanical characterization of PEDOT:PSS thin films. *Synthetic Metals*, 159, 2009.

[19] M. P. Nikiforov et al. Delineation of the effects of water and oxygen on the degradation of organic photovoltaic devices. *Solar Energy Materials and Solar Cells*, 110, 2013.

[20] T. Nagata et al. Effect of uv–ozone treatment on electrical properties of pedot:pss film. *Organic Electronics*, 12, 2011.

[21] A. I. S. Neves et al. Transparent conductive graphene textile fibers. *Scientific Reports*, 5, 2015.

[22] A. I. S. Neves et al. Towards conductive textiles: coating polymeric fibres with graphene. *Scientific Reports*, 7, 2017.

[23] K. J. Phillips et al. The technology of polypropylene tape yarns: processing and applications. *Textile Progress*, 33, 2003.

[24] K. S. Kim et al. Large-scale pattern growth of graphene films for stretchable transparent electrodes. *Nature*, 457, 2009.

[25] H. J. Hye Jin Park et al. Growth and properties of few-layer graphene prepared by chemical vapor deposition. *Carbon*, 48, 2010.

[26] M. Bredol et al. Materials for powder-based ac-electroluminescence. *Materials*, 3, 2010.

[27] Ceresana. Market study: Polypropylene (4th edition).

[28] S. H. Say Hwa Tan et al. Oxygen plasma treatment for reducing hydrophobicity of a sealed polydimethylsiloxane microchannel. *Biomicrofluidics*, 4, 2010.

[29] A. K. Yetisen et al. Nanotechnology in textiles. *ACS Nano*, 10, 2016.

[30] Z. Kolská et al. Surface properties of poly(ethylene terephthalate) foils of different thicknesses. *Journal of Materials Science*, 47, 2012.

[31] J. Ibañez et al. Frequency-dependent light emission and extinction of electroluminescent zns:cu phosphor. *Displays*, 28, 2007.

6

GRAPHENE-BASED TOUCH-SENSORS ON TEXTILE FIBRES

6.1 MOTIVATION

The capability of sensing human touch is a characteristic that many electronic interfaces require for a myriad of purposes. These span from healthcare, consumer electronics to military and transport applications. The most common touch-sensors available nowadays are still rigid and bulky, attributes that make them un-suitable for the next generation of electronics, where flexible, lightweight and imperceptible devices are demanded, especially within the wearable electronics industry. Moreover, they need to withstand mechanical shocks, heat resistance, avoid skin corrosion, etc...[1] The processing of these devices however relies on thermal deposition of materials on smooth surfaces in most cases, making their compatibility with the new generation of flexible substrates, mainly polymers and organic materials, very difficult. Specifically, the textile industry has well-established methods of production which are not always readily compatible with the semiconductor industry processes, as mentioned in the previous chapter.[2]

Since the discovery of graphene, its high transparency and conductivity have been subject of much attention; especially when graphene is cited as replacement for indium tin oxide (ITO) in optoelectronic devices. A well-known usage of such properties are the smart-phone screens, where touch-sensing capability is embedded in the screen allowing device manipulation while simultaneously displaying information.

This is usually done using ITO, which is both transparent and conductive but not flexible and increasingly expensive due to In scarcity; this hinders its potential for wear-

able electronics due to lack of mechanical durability and production volume. There have been some reports where graphene and graphene derivatives have been used employing different architectures to create such touch-sensors, and nanowires (NW) and poly(3,4-ethylenedioxythiophene) polystyrenesulfonate (PEDOT:PSS)-based sensors have been also demonstrated.[3;4;5;6;7;8;9;10;11;12;13;14;15;16;17]

Nevertheless, most of them rely on resistive or thermoelectric sensing, which offers worse performance when used solely as touch-sensors or they use thick graphene materials where the high transparency of single-layer graphene (SLG) is lost. Also, they need a substrate, usually polydimethylsiloxane (PDMS) or polyethylene terephthalate (PET) on which fabricate the device, when a free-standing device would be much more convenient for its integration into garments. Lastly, the processing techniques or materials employed are unsuitable for mass-production due to their complexity or high-cost. This is especially the case of metallic NW-based transparent conductive film (TCF); the high cost of Au and Ag NW, together with stability and toxicity issues (Ag reacts when in contact with humidity and sweat apart from being a known allergen) make them difficult to implement in wearable technologies, despite some efforts.[18;19;20;11;12] Thus the ultimate wearable touch sensors, in which all these attributes are met in a single device, is yet to be realised.

In this chapter highly transparent, flexible, robust and free-standing capacitive touch sensors are presented, based on polypropylene (PP) textile fibres coated with different graphene materials. Introduced in the previous chapter, PP is an ubiquitous polymer employed in a myriad of applications, from cleanroom clothing and parachutes to waterproof garments and automobile textiles. Such sensors are created using a simple, scalable process, with a pioneering lithographic technique which ensures compatibility with roll-to-roll (R2R) processing. The performance and resilience of these devices is thoroughly analysed, using both types of projective-capacitive (p-cap) sensing, self- and mutual-capacitive. Furthermore, the easy and individual processing of these textile fibres allows for versatility in device design and operation; their potential is shown by creating an array of such devices, where a woven free-standing position-sensitive capacitive touch sensor is demonstrated.

6.2 SENSING MECHANISM

Usually, touch-sensing is interpreted as the change from an OFF state, where there is no touch between two biased electrodes and a high-impedance is read, to an ON state, where there is touch and low-impedance is read, as seen in the Figure 6.1a. In the OFF state, the circuit is open and only a capacitive contribution from the air is measured; in the ON state, the finger shorts the two electrodes and the impedance is given then by both resistive and capacitive contributions (see Figure 6.1a) as $|Z| = \frac{R}{1+\omega CR}$, where C and R are the capacitance and resistance of the human finger.

There are two main schemes for touch detection: resistive and capacitive, as seen in Figure 6.1b. Resistive touch sensing relies on a change in resistance as a sensing parameter, which is usually realised with two conductors separated by a gap. When the sensor is touched, the circuit is closed by the finger altering the resistance of the system which is interpreted as signal. Even though it is conceptually simple, this approach as been abandoned in favour of capacitive touch sensing, which is more reliable and durable, for commercial applications.

In commercial devices, the implementation of touch-sensing is normally carried out through capacitive touch-sensing, which can be realised in two ways: mutual and self-capacitive capacitive (see the Figure 6.1b). In the mutual capacitive scheme, two different electrodes (a drive electrode and a sense electrode) are biased creating a capacitor. When the electric field fringes are disturbed by an external element (i.e. finger), this produces a capacitive change which is interpreted as a signal.[21] This is conceptually similar to the resistive approach.

In self-capacitance, the touch is recognised by the addition to the sensing circuit of a capacitance (i.e. a finger) in parallel, and this larger capacitance is interpreted as a touch, as it will be explained in the results section. Its functioning is a bit more complex than the mutual capacitive approach since it requires a microcontroller, but its reliability and fast performance have made it the industry standard.

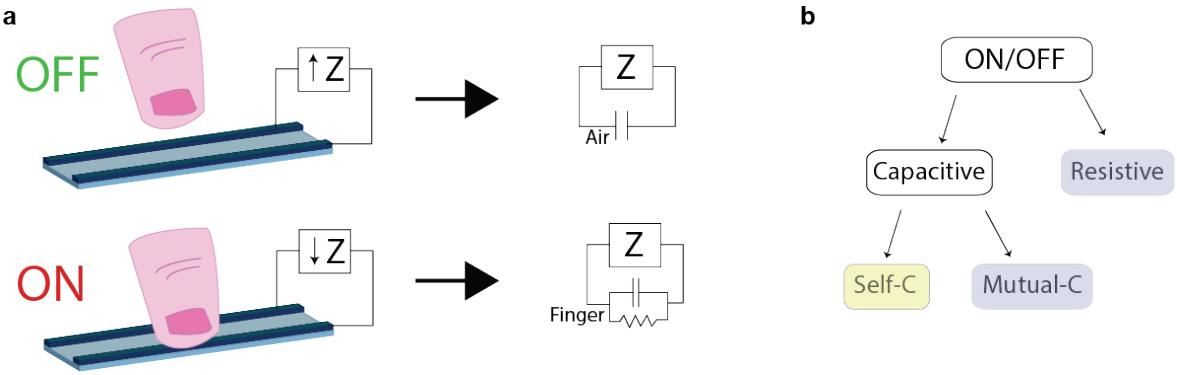

Figure 6.1: a) Schematic of the touch-sensing mechanism (ON/OFF states), using impedance as sensing parameter. The equivalent circuits are shown. b) Clasification of touch-sensing schemes. Mutual-capacitive and resistive are blue-coloured to highlight the similar sensing mechanism; self-capacitive is yellow-coloured because the sensing is implemented with electronics.

6.3 SAMPLE FABRICATION

A new lithographic approach that is compatible with R2R processing has been developed for the purpose of creating touch-sensors. The way usually a pattern is transferred to graphene is by means of reactive ion etching (RIE) after patterning, as performed in the previous chapter. Nevertheless, RIE is a technique that requires vacuum and plasma generation, which are of difficult incorporation into R2R workflows.

To illustrate this, in Figure 6.2a we sketched a typical PMMA-assisted graphene transfer and patterning process on a PP fibre: after transferring the PMMA/graphene membrane on top of the fibre and removing the poly(methyl methacrylate) (PMMA) with an acetone bath, photoresist is spun, exposed and developed. Then, a RIE process is performed to etch away the graphene, and then the photoresist is stripped away with acetone and device is finally contacted with silver paint and finished.

The novel R2R approach is shown in Figure 6.2b: prior to the PMMA/graphene transfer, the fibre is patterned. Then, the PMMA/graphene membrane is transferred on top of the patterned fibre; upon PMMA removal with acetone, the pattern underneath will dissolve as well, tearing apart the graphene that was on top of it and effectively transferring the pattern to the graphene sheet. In this way we removed the necessity of a RIE etching step, making it readily compatible with R2R techniques, and also we

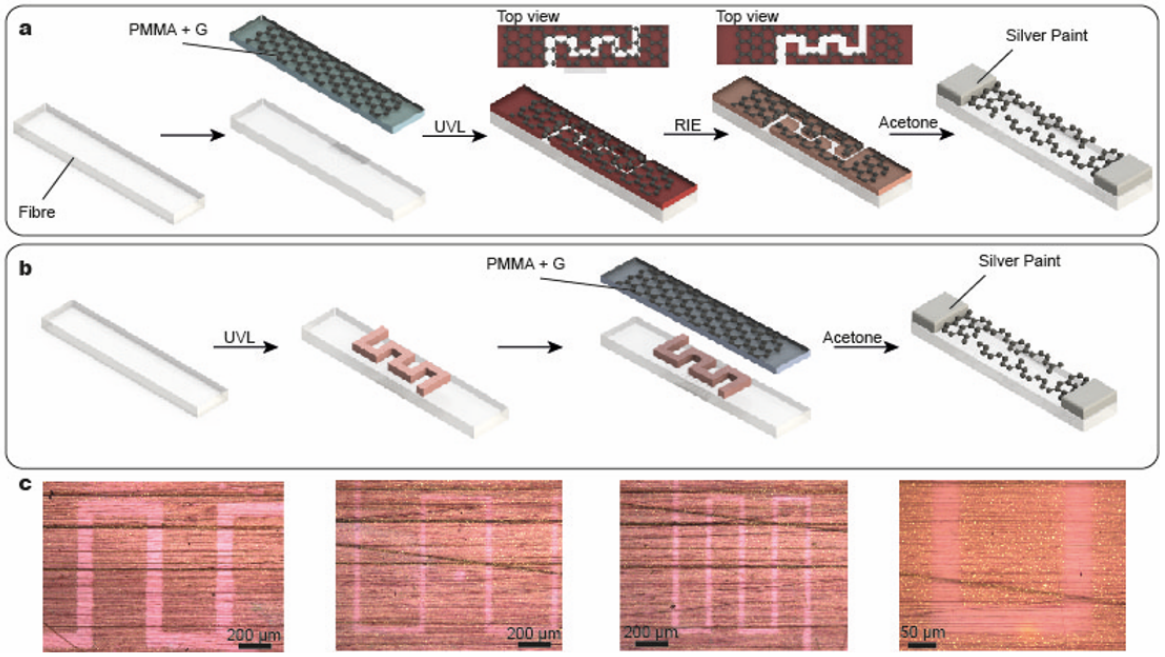

Figure 6.2: a) Standard lithographic process. b) Roll-to-roll compatible lithographic process. c) Optical microscope pictures of patterns realised with the roll-to-roll compatible process.

shorten the processing time since we have eliminated one step. We were able to define interdigitated electrodes, with features from 100 μm down to 50 μm wide and a pitch from 1000 μm to 250 μm with perfect definition (see Figure 6.2c). Larger features can be achieved, and we believe that after some parameter optimization smaller features can be done too.

SLG was grown by chemical vapour deposition (CVD) in Cu foils (from Alpha Aesar) at atmospheric pressure (in an MTI Furnace), as explained in Chapter 3. liquid-exfoliated graphene (LEG) was produced by shear exfoliation of graphite in water, as explained in Chapter 3. few-layer graphene (FLG) was purchased from Graphene Supermarket. Graphene transfer was carried out by the standard PMMA-assisted method (for CVD graphene) and vacuum filtration and water-assisted transfer (for LEG) as explained in Chapter 3. Patterning of the fibres was done by standard optical lithography (OL). Contacts were realised with silver paint.

6.4 CHARACTERIZATION AND RESULTS

To explore the potential of this novel technique, we transferred CVD-grown SLG, CVD-grown FLG and LEG onto PP fibres. The successful transfer was confirmed with Raman spectroscopy, where the different intensities of the G peak, signature of SLG and FLG, are clearly observed (see Figure 6.3a). The different devices can be seen in the photograph in Figure 6.3b; since the different graphenes (CVD and LPE) are processed with different methods, their transparencies are different. These are shown in Figure 6.3c, in good agreement with previous reports: for SLG the decrease in transparency with respect the bare fibre is about 2-3%; with FLG this decrease is about 20% and with LEG the absolute transparency is about 40%.

Importantly, the roughness in these fibres can be as high as 700 nm, as demonstrated in the previous chapter;[22] the typical thickness of sputtered ITO for electronics applications is between 300 - 400 nm, otherwise the material suffers from poor transparency and flexibility.[23;22] Given the roughness of these fibres, ITO cannot be a suitable material because this high fibre roughness makes it challenging to obtain continuous films; this can be an issue when using metallic NW as well. Due to this, graphene seems the only feasible material to be deposited on these fibres for electronics purposes. It is important to mention once again, the transfer and patterning are performed once the

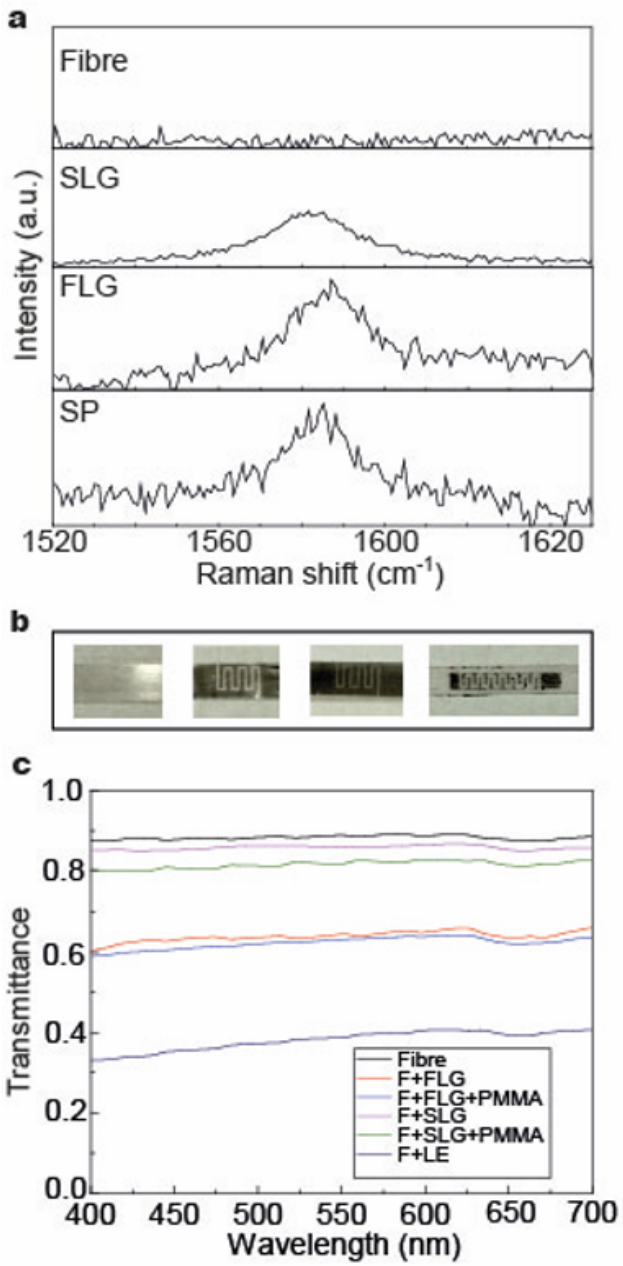

Figure 6.3: a) Raman spectra of a bare fibre, SLG, FLG and SPG (from top to bottom). b) Photographs of SLG, FLG, blade-cut SPG and roll-to-roll SPG devices. c) Transmittance spectra of the devices employed here.

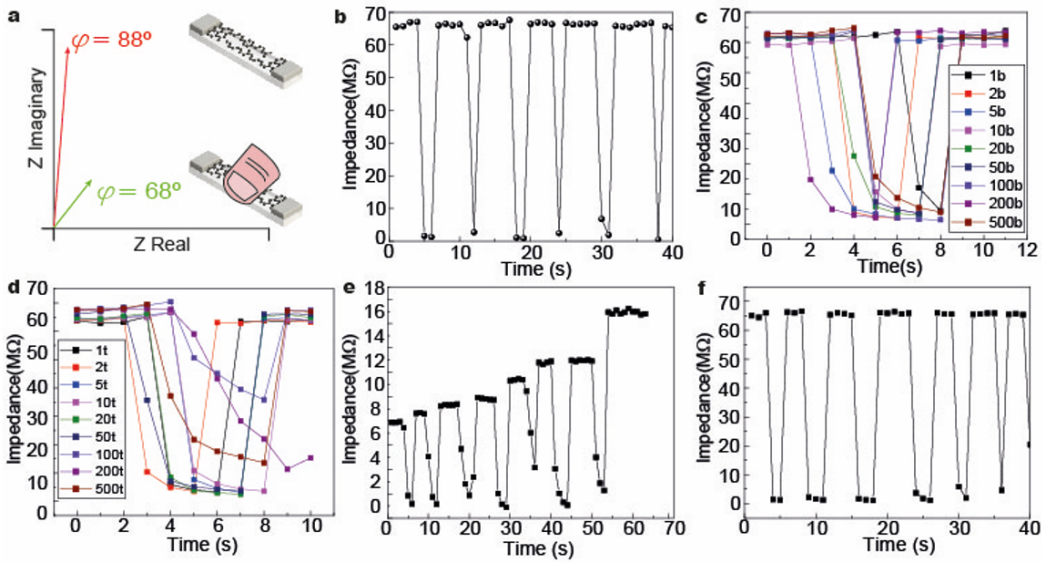

Figure 6.4: a) Sketch of the impedance response with and without touching. b) Impedance upon touching versus time. c) Impedance upon touching versus time for different number of bending cycles. d) Impedance upon touching versus time for different number of touches. e) Impedance upon touching versus time for a SPG sample with RIE process. f) Impedance upon touching versus time for a SPG sample with roll-to-roll process.

fibre is manufactured, removing intermediate steps within the manufacturing process which may be not compatible with the production work flow.[2]

Two mechanisms are behind the touch-sensing response in these devices: either resistive, where a change in resistance is the measured signal, or capacitive, where this signal comes from a change in capacitance in between the electrodes. When the device is untouched, the impedance modulus is around 60 $M\Omega$ and $\phi = 89^o$, since the PP fibres are insulating. When the device is touched, both the impedance modulus reduces drastically by an order of magnitude and the phase drops down to $\phi = 68^o$, due to the finger effectively shorting both interdigitated electrodes, reducing both the resistance and the capacitance of the device. This can be seen in Figure 6.4a. As mentioned before, one can choose to measure resistance or capacitance to detect touch, depending on which one is more convenient.

The resilience of the devices is further tested with a series of touches, shown in Figure 6.4b with a FLG device. When the finger is pressed (ON state) the impedance drops, and when released (OFF state) the impedance increases back to its original value with great stability. Since a flexible, wearable touch-sensor would be subjected to mechanical stress, we further analyse the OFF/ON/OFF performance of our device upon 500 bends (see Figure 6.4c) and 500 touches (see Figure 6.4d). The performance of the device remains the same up to 500 bends thanks to the great flexibility of graphene. Surprisingly, given the atomic thickness of our active material, the performance of the device remains good after 500 touches, with a clear distinction between the OFF/ON/OFF states. These results are consistent, with great reproducibility, for all the graphene materials employed in the study (see Figure 6.5 and Figure 6.6) for both normal and R2R processing.

The potential of our novel R2R approach is exemplified with LEG: in Figure 6.4e a LEG sample was processed using the normal processing, using RIE to etch away the graphene and transfer the pattern. After several RIE runs, the films are still conductive in the OFF state, meaning that the graphene has not been fully etched away; moreover, the resistance increases after every touch, which is an indication that with every touch the finger is removing graphene flakes from the channel, hence erasing percolation pathways and changing the conductivity of the sample, making it unsuitable for sensing due to this variability. This effect is not observed in the LEG with the R2R approach, where the performance of the device is the same to that of the other devices with

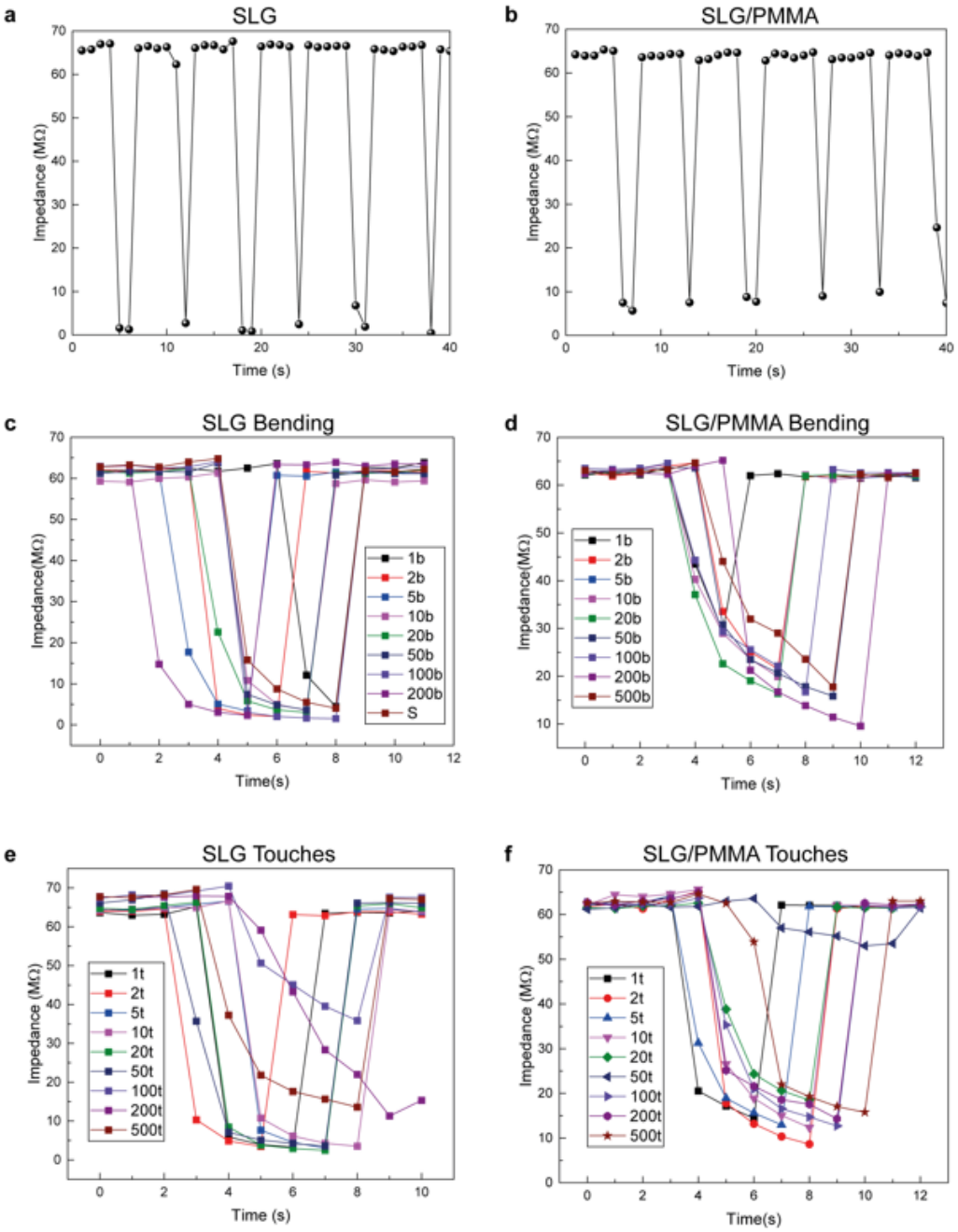

Figure 6.5: a) SLG device performance. b) SLG/PMMA device performance. c) SLG device performance for different number of bendings. d) SLG/PMMA device performance for different number of bendings. e) SLG device performance for different number of touches. f) SLG/PMMA device performance for different number of touches.

other graphene electrodes. Also, alternatively the LEG can be mechanically patterned with a blade achieving same performance (see Figure 6.6). For further protection, the devices can be encapsulated with a thin layer of PMMA (400 nm) spun on top, acting as a protection layer, without altering their capacitive performance (see Figure 6.5 and Figure 6.6).

Finally, some of these devices were woven together to make a highly transparent, flexible and position-sensitive array as shown in Figure 6.7a. The inset shows a conventional capacitive touch sensor array taken from a mobile phone, where its opacity and bulkiness make it not suitable for the next generation of wearable devices.

In contrast, our arrays can be attached to a garment or bare skin, or even a single fibre can be wrapped around a finger, as shown in Figure 6.7b, while retaining full functionality. The array consist of 6 sensing fibres, 3 of them along the X direction and 3 of them along the Y direction, which provides a total of 9 sensitive points at the cross point of each of these fibres, woven within a bare PP fibre matrix. Once coated with graphene and prior to weaving, the edges of the fibres were removed to avoid parasitic contact between the fibres; then the fibres were coated with PMMA for further insulation and protection. The sensing mechanism in this devices is purely self-capacitive touch-sensing, widely used across the electronics industry due its superior performance and reliability against resistive touch-sensing.[21] We used a commercially available Charge Time Measurement Unit (CTMU) microcontroller, which is sketched again in Figure 5.6c. The sensing mechanism is the following: the CTMU microcontroller has a constant-current source I that charges an internal capacitor C_I to a voltage V for a given time. This voltage follows $V = It/C$, so when a finger with external capacitance C_F is added in parallel to the total capacitance, increases to $C = C_I + C_F$, resulting in a lower V. This voltage is continuously measured by the Analog to Digital (A/D) converter, so if the voltage reading changes, that is interpreted as touch.

We implemented an algorithm, that only when two fibres in the X and Y direction are touched simultaneously the controller registers a signal, allowing unequivocal position-sensitive recognition. The performance upon several touches is shown in Figure 6.7d, with very stable ON/OFF states. Also, the speed of sensing is analysed with the help of an oscilloscope, finding a rise and fall times of 1.4 ms, regardless the materials used, which implies that this time is limited by the electronics used in the measurement, and that probably the actual response time is lower than that. However,

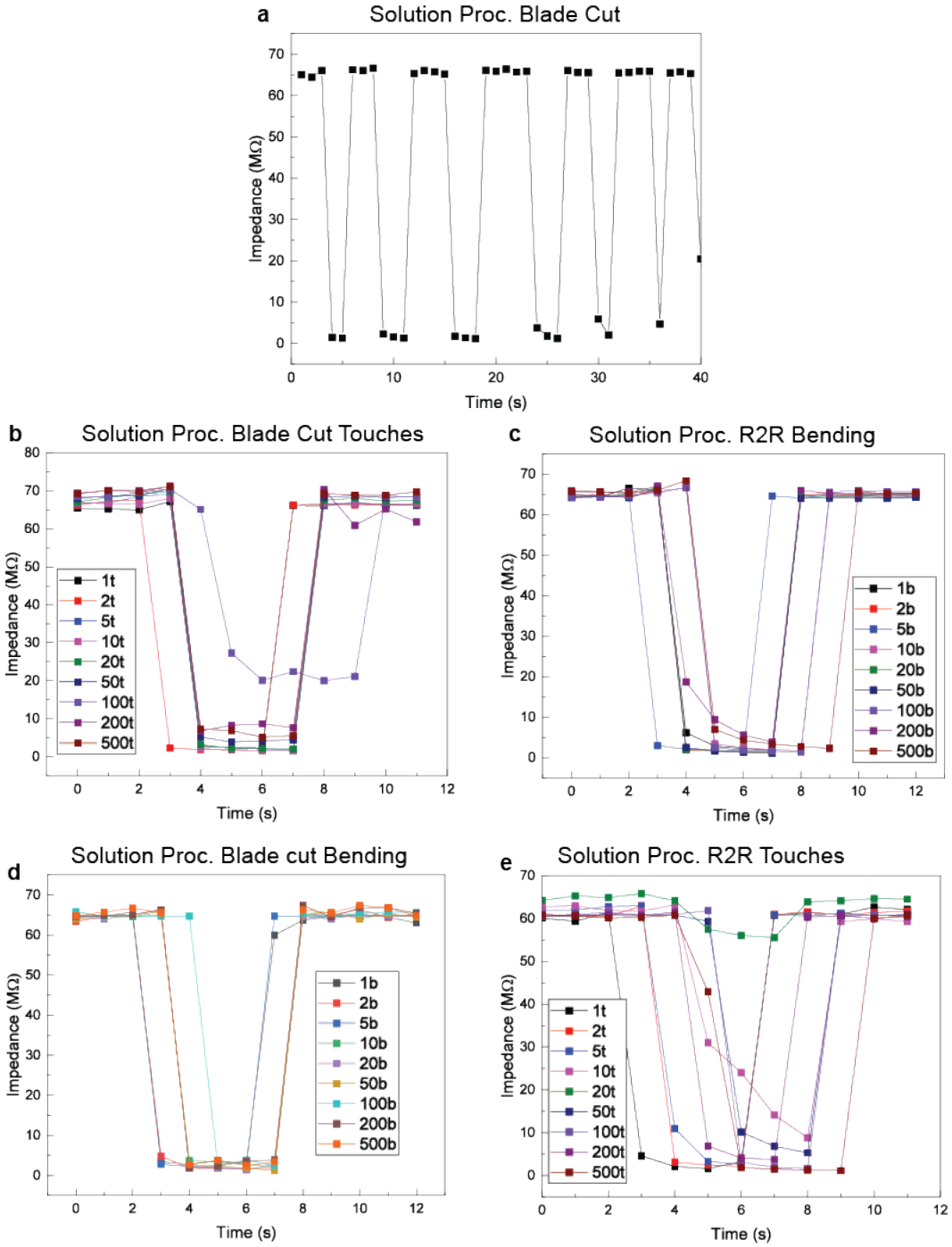

Figure 6.6: a) LEG-Blade cutted device performance. b) LEG-Blade cutted device performance after several touches. c) LEG-R2R device performance after several bendings. e) LEG-Blade cutted device performance after several bendings. f) LEG-R2R device performance after several touches.

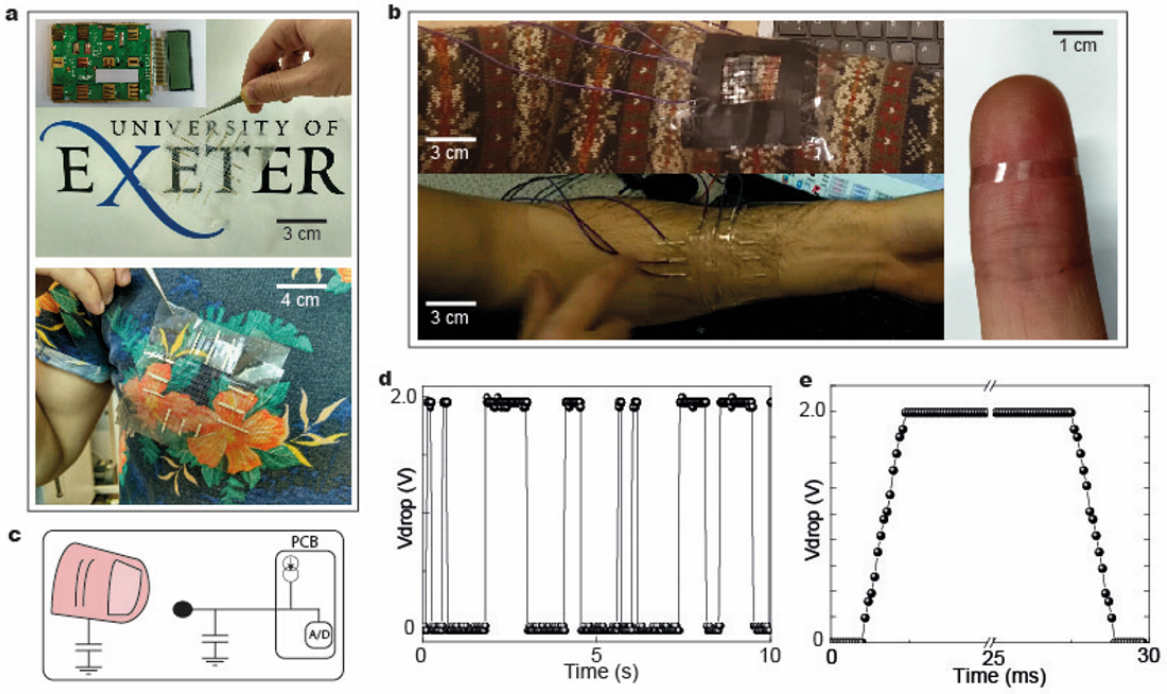

Figure 6.7: a) Pictures of the highly transparent array. The inset shows a commercial touch sensor of an old phone. b) Device can be attached to a sweater or a bare skin. Single fibres can be wrapped around fingers. c) Schematic of the electronics of the self-capacitive touch-sensing. d) Performance of the arrays upon touching using the self-capacitive scheme. e) Magnified response of the self-capacitive scheme upon touching; speeds in the range of ms are achieved.

this rise and fall times are within the range of commercial devices, and combined are the best values in the literature to the best of my knowledge. Also, the conventional complementary metal oxide semiconductor (CMOS) electronics needed for the microcontroller may be miniaturized and mounted in a flexible substrate as has been shown before.[21;10] Moreover, due to the possibility of patterning, more complicated detection schemes such as mutual-capacitance based can be readily implemented, when more complicated functions such as simultaneous multi-touch features are required.

6.5 CONCLUSIONS

In summary, this chapter presents for the first time of transparent, flexible and durable touch-sensors embedded on polymer fibres. These devices have great potential for wearable applications. Besides the wide range of graphene-based materials employed, which enables tailoring of their features depending on their application, we introduce a novel patterning technique for graphene that enables R2R processing of these fibres and removes the necessity of a RIE to accurately transfer patterns onto graphene, and possibly other two dimensional (2D) materials such as graphene oxide (GO) or reduced graphene oxide (r-GO), hexagonal boron nitride (h-BN) or transition metal dichalcogenides (TMDs); this new lithography technique is of great interest due to the increasing availability of 2D materials in solutions.[24;25] Furthermore, these fibres were employed to create highly transparent, flexible and durable position-sensitive arrays. Using commercially available capacitive touch-sensing electronics, the immediate feasibility of this technology for textile applications is demonstrated.

BIBLIOGRAPHY

[1] S. Park et al. Enhancing the quality of life through wearable technology. *IEEE Engineering in Medicine and Biology Magazine*, 22, 2003.

[2] A. K. Yetisen et al. Nanotechnology in textiles. *ACS Nano*, 10, 2016.

[3] H. Tian et al. A graphene-based resistive pressure sensor with record-high sensitivity in a wide pressure range. *Scientific Reports*, 5, 2015.

[4] Y. A. Samad et al. Novel graphene foam composite with adjustable sensitivity for sensor applications. *ACS Applied Materials & Interfaces*, 7, 2015.

[5] Y. R. Jeong et al. Highly stretchable and sensitive strain sensors using fragmentized graphene foam. *Advanced Functional Materials*, 25, 2015.

[6] R. Kazemzadeh et al. Highly sensitive pressure sensor array with photothermally reduced graphene oxide. *IEEE Electron Device Letters*, 36, 2015.

[7] J. S. Lee et al. Highly sensitive and multifunctional tactile sensor using free-standing ZnO/PVDF thin film with graphene electrodes for pressure and temperature monitoring. *Scientific Reports*, 5, 2015.

[8] O. A. Araromi et al. High-resolution, large-area fabrication of compliant electrodes via laser ablation for robust, stretchable dielectric elastomer actuators and sensors. *ACS Applied Materials & Interfaces*, 7, 2015.

[9] S-E. Zhu et al. Graphene based piezoresistive pressure sensor. *Applied Physics Letters*, 102, 2013.

[10] H. Heidari et al. E-skin module with heterogeneously integrated graphene touch sensors and cmos circuitry. In *2016 IEEE SENSORS*, 2016.

[11] Z. Cui et al. Design and operation of silver nanowire based flexible and stretchable touch sensors. 30, 2015.

[12] S. Gong et al. A wearable and highly sensitive pressure sensor with ultrathin gold nanowires. *Nature Communications*, 5, 2014.

[13] S. Chun et al. A flexible graphene touch sensor in the general human touch range. *Applied Physics Letters*, 105, 2014.

[14] C. Hou et al. Highly conductive, flexible, and compressible all-graphene passive electronic skin for sensing human touch. *Advanced Materials*, 26, 2014.

[15] S. Takamatsu et al. Flexible fabric keyboard with conductive polymer-coated fibers. In *2011 IEEE SENSORS Proceedings*, 2011.

[16] T. Vuorinen et al. Inkjet-printed graphene/PEDOT:PSS temperature sensors on a skin-conformable polyurethane substrate. *Scientific Reports*, 6, 2016.

[17] S. Takamatsu et al. Transparent conductive-polymer strain sensors for touch input sheets of flexible displays. *Journal of Micromechanics and Microengineering*, 20, 2010.

[18] D-H. Kim et al. Epidermal electronics. *Science*, 333, 2011.

[19] M. Kaltenbrunner et al. An ultra-lightweight design for imperceptible plastic electronics. *Nature*, 499, 2013.

[20] A. Miyamoto et al. Inflammation-free, gas-permeable, lightweight, stretchable on-skin electronics with nanomeshes. *Nature Nanotechnology*, 12, 2017.

[21] G Barrett et al. Projected-capacitive touch technology. *SID Information Display*, 2010.

[22] K. J. Phillips et al. The technology of polypropylene tape yarns: processing and applications. *Textile Progress*, 33, 2003.

[23] H. Kim et al. Effect of film thickness on the properties of indium tin oxide thin films. *Journal of Applied Physics*, 88, 2000.

[24] D. McManus et al. Water-based and biocompatible 2d crystal inks for all-inkjet-printed heterostructures. *Nature Nanotechnology*, 12, 2017.

[25] J. N. Coleman et al. Two-dimensional nanosheets produced by liquid exfoliation of layered materials. *Science*, 331, 2011.

7

LIQUID-EXFOLIATED GRAPHENE AND GRAPHENE OXIDE FOR ALL-CARBON HUMIDITY SENSORS

7.1 MOTIVATION

The potential of graphene for sensing applications is well known, spanning from single molecule gas to light detection.[1;2;3;4;5;6;7] Other two-dimensional materials have been studied with the same purposes too.[8;9;10;11;12] Particularly graphene oxide (GO), which is a graphene compound which has different oxygen functional groups attached to it, has been demonstrated as an excellent material for sensing humidity, among other properties.[13;14;15;16] The truly two dimensional (2D) nature of these materials and hence their great surface to volume ratio are behind the exceptional response exhibited, as it has been mentioned in previous chapters.

One key advantage of graphene oxide (GO) is that is readily soluble in water, which allows it to be dispersed in solutions that can be spun or vacuum filtered. This can also be achieved in graphene with different solvents using a surfactant which enables graphene's dispersion; moreover, choosing appropriate solvent enables liquid exfoliation of a wide variety of 2D crystals.[17;18;19;20;21] The great scalability of their production and their cost-effectiveness make them of big interest for the industry; furthermore, their synthesis and deposition is generally carried out at room or moderate temperatures, which dramatically facilitates their integration with flexible polymeric substrates such as polyethylene terephthalate (PET), polyethylene naphthalate (PEN), polystyrene (PS) and polycarbonate (PC), commodity plastics that are used ubiquitously as printed electronic substrates.

Monitoring humidity is key in many applications or industrial processes. Pulp,

paper and cardboard factories need a precise measurement of humidity during their processes to ensure the final quality of their products. The ambient humidity when storing explosives and ammunition needs to be low to avoid corrosion and deterioration of the gunpowder. In the transport of vaccines and pharmaceuticals, a tight control of humidity is necessary to avoid condensation for labelling, coding and final packing of food and edibles. For instance, the World Health Organization' requirements for Time and Temperature Sensitive Pharmaceutical Product (TTSPP) establishes a 5% accuracy in humidity readings and they should be minimally affected by transient events.[22]

However, despite the reports using these 2D solutions for inkjet printing and spin-coating, little is being done with these materials when it comes to actual applications, and most of them do not fully exploit 2D intrinsic features such as good flexibility and transparency, which can be of major importance when applications need to be embedded in consumer products. The mix of these 2D materials, which gave rise to heterostructures, have been extensively realized with mechanically exfoliated samples and a few works with inkjet printing have been demonstrated already, but despite the ever increasing number of studies reporting such 2D inks with different features and properties, their combination and integration into real-life applications and devices is still very small.[23;24;25;26;27;28;29;30;31;32;33]

One of the main drawbacks of these solutions is that once they are deposited as large area films, they are very difficult to pattern by means of dry or wet etching due to their large thicknesses, a key process for device fabrication. This can be overcome using screen printing processes, but it is really challenging to achieve patterns with linewidths of under 100 μm and very extensive optimization of mesh and paste formulation is required.

Alternatively one could use inkjet printing, where the inks are selectively printed to form patterns. Despite some reports in carbon nanotubes (CNT) and 2D materials inkjet printing, achieving micron-size resolution and functional devices, it is a time consuming process since the printer has to raster over the substrate, and this can be a drawback if multiple depositions are needed; also, the inks usually require extensive formulation engineering, and they usually require substrate functionalization or need chemically aggressive and/or thermal post-deposition treatments to achieve desired features.[23;24;26;27;28;31] Moreover, the creation of these devices should be compatible

with the existing approaches in materials processing such as complementary metal oxide semiconductor (CMOS) techniques and the emerging roll-to-roll (R2R) processing for the successful integration of such devices into mass-production lines.

In this chapter, a workflow that allows integration of these 2D inks and their combinations, to create accurate patterns and enabling device designing, is demonstrated. Carefully formulated water-based liquid-exfoliated graphene (LEG) and GO solutions were employed to create interdigitated LEG electrodes and thin GO sensing films, demonstrating the full power of this technique to accurately place and aggregate different 2D materials in a large scale. To demonstrate its potential, all-carbon humidity sensors were created at the wafer scale level, with CMOS-compatible and room temperature processing techniques. These sensors have uniform response, good life time, transparency and flexibility. In principle, this method can be conveniently adapted to any kind of 2D material dispersion and combination to produce patterns and devices with different functionalities, with high yields over large areas.

7.2 DEVICE PHYSICS

The physical process giving rise to this response is summarised as follows: in GO, planes and edges contain oxygen functional groups, which gives it its hydrophilicity and also their naturally insulating properties.

At low relative humidity (RH), water molecules are primarily physisorbed onto the available active sites (hydrophilic groups, vacancies) of the GO surface through double hydrogen bonding. The water molecules are thus unable to move freely because of the restriction from double hydrogen bonding. However, these physisorbed water molecules can be ionized producing hydronium ions (H_3O^+) that behave as charge carriers, but the hopping transfer of protons between adjacent hydroxyl groups in the first-layer of physisorbed water requires much energy due to the double hydrogen bonding; it is for this reason that GO films exhibit strong electrical resistance. Although the protons in GO films are minimal, and are restricted by discontinuous mobile layers, they contribute to the conduction.

As the RH increases, the multilayer physical adsorption of water molecules occurs. A second physisorbed layer is created, where water molecules are bond through single hydrogen to the hydroxyl groups. Thus, the water molecules become more mobile and

resemble that of the bulk behaviour.[16] As more water is physisorbed, proton-transfer reactions take place, hopping in between water molecules and oxygen-rich groups within the GO via Grotthuss chain reaction.[16;34] This in fact increases the conductance, which is used as sensing parameter.

The weak forces involved in the process allow reversibility and desorption of compounds by thermal agitation, which is in the range of 26 meV at room temperature.

7.3 SAMPLE FABRICATION

The process for the device fabrication is sketched in Figure 7.1a. First, a layer of polymethylglutaramide (PMGI) is spun and baked over a Si/SiO_2 substrate, with a resultant thickness of $\sim$250 nm. Then, a layer of photoresist (PR) is spun and baked, achieving a thickness of $\sim$1.4 μm. This PR is then exposed with the help of a laser writer to create a pattern and is then developed, as in standard optical lithography (OL).

In our devices, we patterned interdigitated electrodes and snake-like ribbons as seen in Figure 7.1b. The interdigitated electrodes are used as contacts in the humidity sensors. The developer dissolves not only the areas where the PR has been exposed (acting as an image resist), but also to the PMGI layer which is underneath. After the development step, the PR is stripped off with acetone and isopropanol (IPA), whereas the patterned PMGI remains. This is crucial, since the LEG deposition is assisted by IPA, thus the pattern needs to withstand IPA. For the lithographic step, PMGI SF6 from MicroChem Corp. was spun at 4000 rpm, baked at 180 ^oC for 360 seconds. Then, PR S1813 from MicroChem Corp is spun at 4000 rpm and baked at 120 ^oC. Then, the sample is loaded into a laser-writer from Durham Magnetoptics Ltd, exposed, and developed in an alkaline-based solvent (tetramethyl-ammonium hidroxide (TMAH)). As just mentioned, this chemical also etches the bottom PMGI layer.

Subsequently, the deposition of LEG takes place by IPA-assisted transfer, as explained in Chapter 3. The advantage of using the IPA-assisted transfer is that it is not affected by surface interaction such as hydrophilicity as much the water-assisted method, which is of great advantage when using silicon dioxide (SiO_2) or PET substrates, naturally hydrophobic. Pictures of the filters can be seen in Figure 7.1c. The process can be carried out again to increase conductivity and film uniformity; at least

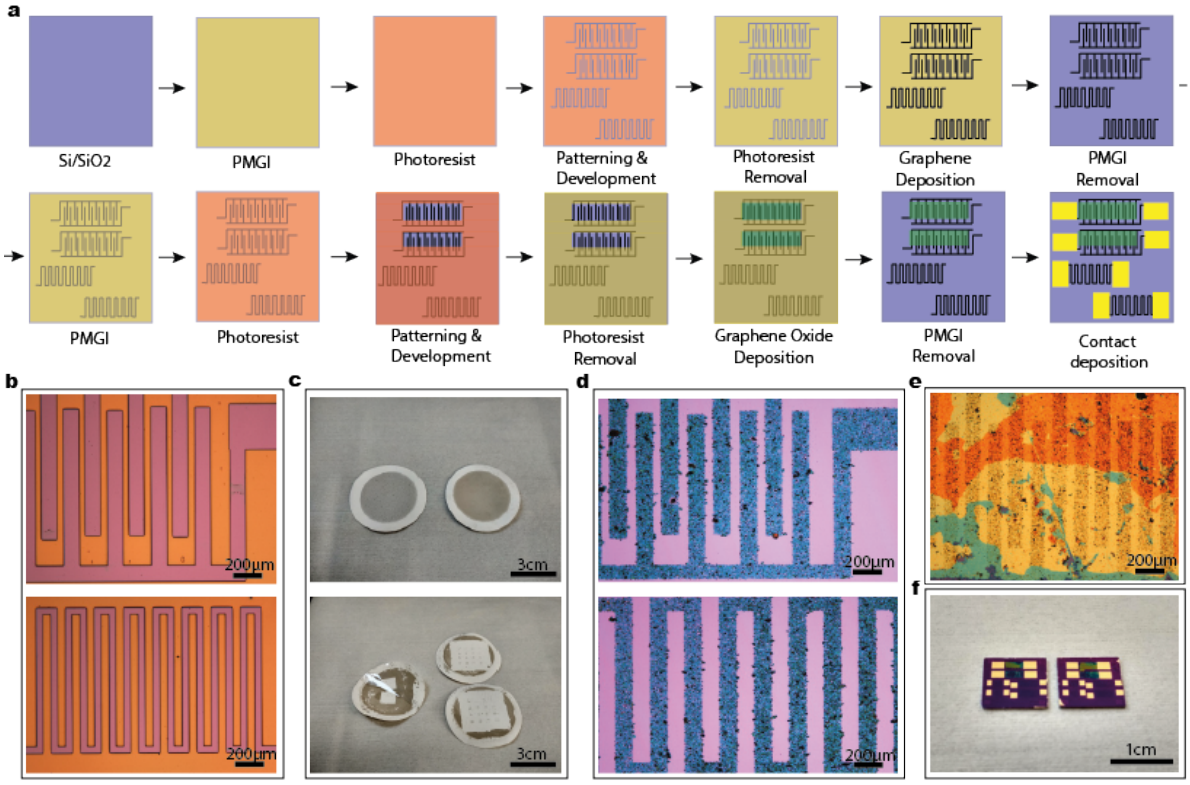

Figure 7.1: a) Sketch of the fabrication process. b) Patterned features on a Si/SiO_2 chip. c) Filters used for graphene deposition by IPA-assisted method. d) Resulting patterns after graphene deposition and PMGI stripping off. e) Graphene oxide placed on top of the interdigitated electrodes. f) Finished devices after metallization.

four depositions are necessary to create graphene patterns that are conductive in this work. Stacks of different materials and films can be made using this technique. When the deposition is the desired one, the PMGI is dissolved using n-methyl-2-pyrrolidone (NMP) and is introduced in a mild ultrasonic bath to help the lift-off process. The sample is then rinsed first in acetone and then in IPA. An optical microscope picture shows in Figure 7.1d the good agreement between the pattern and the final deposition.

This process is then repeated for the deposition of GO on top of the interdigitated electrodes as shown in Figure 7.1e. The vacuum filtration of GO was done with a cellulose filter, and water and N_2 dry-blowing were employed for its transfer to the substrate, as explained in Chapter 3.

Once the GO has been deposited and the PMGI lifted-off, the sample is finalised by the final metallization step. For these test devices, made on a 1 cm^2 Si/SiO_2 chip as shown in Figure 7.1f, a 5 nm thick wetting layer of Cr and 90 nm thick layer of Au, both thermally evaporated, were employed for contacts.

The LEG solutions were created as explained in Chapter 3. 10 ml of these solution were dispersed in 60 ml of de-ionised water (DIW) and vacuum filtered on a polytetrafluoroethylene (PTFE) filter (from G&E healthcare), which was finally used for the IPA-assisted transfer. 1 ml of GO with concentration of 4 g/L was dispersed in 60 ml of DIW and filtered through a cellulose filter to achieve GO thin-films.

7.4 CHARACTERIZATION AND RESULTS

In order to know more about the outcome and possibilities of this patterning and deposition technique, we patterned lines ranging from 10 μm up to 200 μm, which can be seen in the scanning electron microscope (SEM) photographs of Figure 7.2. It was found that at least 50 μm wide is the minimal width where graphene could be deposited with an acceptable coverage, comparable to those features achieved by ink-jet printing.[25;26;28] This coverage can be improved realizing successive depositions. To assess this step, we patterned 100 μm lines and did a series of 2, 4 (4D) and 6 (6D) depositions. Only 2 deposition rendered poor graphene coverage and no conductive patterns. This means that the percolation threshold for conduction is achieved with a minimum of four depositions and that it changes very little with subsequent depositions.

To corroborate this, we performed profile scans using atomic force microscopy

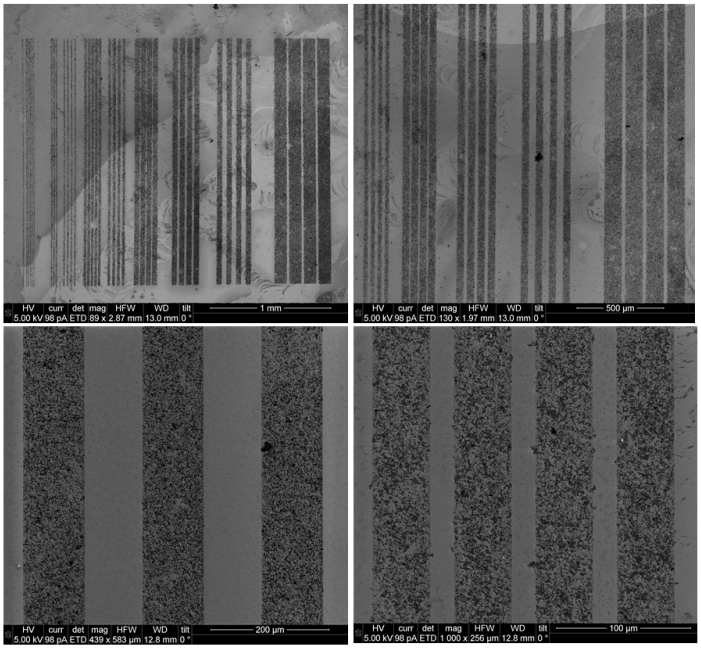

Figure 7.2: SEM pictures of the LEG patterns (on SiO_2) realised to optimise the deposition and resolution of the technique..

(AFM) in DC contact mode. The images shown in Figure 7.2 are also after 6D. In Figure 7.3a and Figure 7.3b an AFM topographic (top, red colored) image and an AFM lateral deviation (bottom, grey colored) are shown of 4D and 6D respectively. From these pictures one can cleary distinguish the LEG from the SiO_2 thanks to the contrast provided by the mechanical nature of the different materials. This contrast is not that evident in the case of GO, because its mechanical properties are different to those of LEG and it is much thinner.

We performed several of these scans to average a value of thickness of such films, resulting in an averaged thickness of 215 *nm* for 4D and 316 *nm* for 6D, with a root mean square (RMS) roughness of 78.72 *nm* and 108 *nm* respectively. In the AFM images one can see the well-defined edges of the graphene tracks, and also appreciate their rough surface. In the case of GO however, shown in Figure 7.3c, the averaged thickness was 31 *nm* with a much smoother surface of only 9 *nm* of RMS roughness. This obvious differences between LEG and GO films are most likely due to the intrinsic hydrophilic character of GO.

A Raman spectroscopy map was performed and the number of layers was deter-

mined using a previously published method by Paton *et al.*[17]. The Raman map in Figure 7.3d sets an average of 6 layers, which comparing with the thickness of the films derived from AFM measurements and assuming 1 nm of interlayer spacing, we calculated that the films are composed of an average number of 10 and 15 graphene flakes of 6 layers for the 4D and 6D samples respectively.

Finally, the sheet and contact resistance were determined, which are plotted in Figure 7.3e. The values of sheet resistance are similar for both 4D (37 $k\Omega$/sq on average) and 6D (46 $k\Omega$/sq on average), yet the values of contact resistance differ slightly, with 14 $k\Omega$/sq and 49 $k\Omega$/sq respectively. This difference in contact resistance is attributed to the larger graphene coverage achieved with 6D than with 4D. Since contact resistance plays an important role in device performance, we used 6D as the standard for device fabrication.

Once the technique was optimised, we analysed the performance of the humidity sensors. The conductance was recorded with a HM8118 LCR bridge from Rohde & Schwarz at 1 kHz and 1 V. In the Figure 7.4a we show the change in conductance produced when the sample is exposed to human exhaled respiration, and it is compared to that of a commercially available CMOS capacitive sensor (HIH-4000-003 from Honeywell).

The performance is very similar. The little differences in response may be attributed to a slightly different positions of the samples, being affected differently by different air flows. Nevertheless, the correlation is between our own LEG/GO device and the CMOS sensor is clear. Moreover, this change in conductance is mainly due to a change in electrical resistance, with a negligible capacitive change. The excitation voltage was only 1 V, suitable for low-power electronics. We tested our device in very humid atmospheres, up to 97% RH; the performance is similar to that of the commercial sensor, as seen in the Figure 7.4b.

Some reports show the correlation between temperature and humidity response of GO sensors; remarkably, that is not the case in these devices, which should in principle help the integration of these sensors in applications. In the Figure 7.4c we show how the sample was heated from room temperature up to 55 ^oC; no appreciable change in conductance is observed. Temperature was measured using a TMP36GT9Z-ND temperature sensor from Digi-Key Electronics. It is well known that GO undergoes reduction when heated up, due to some desorption of some functional groups, which

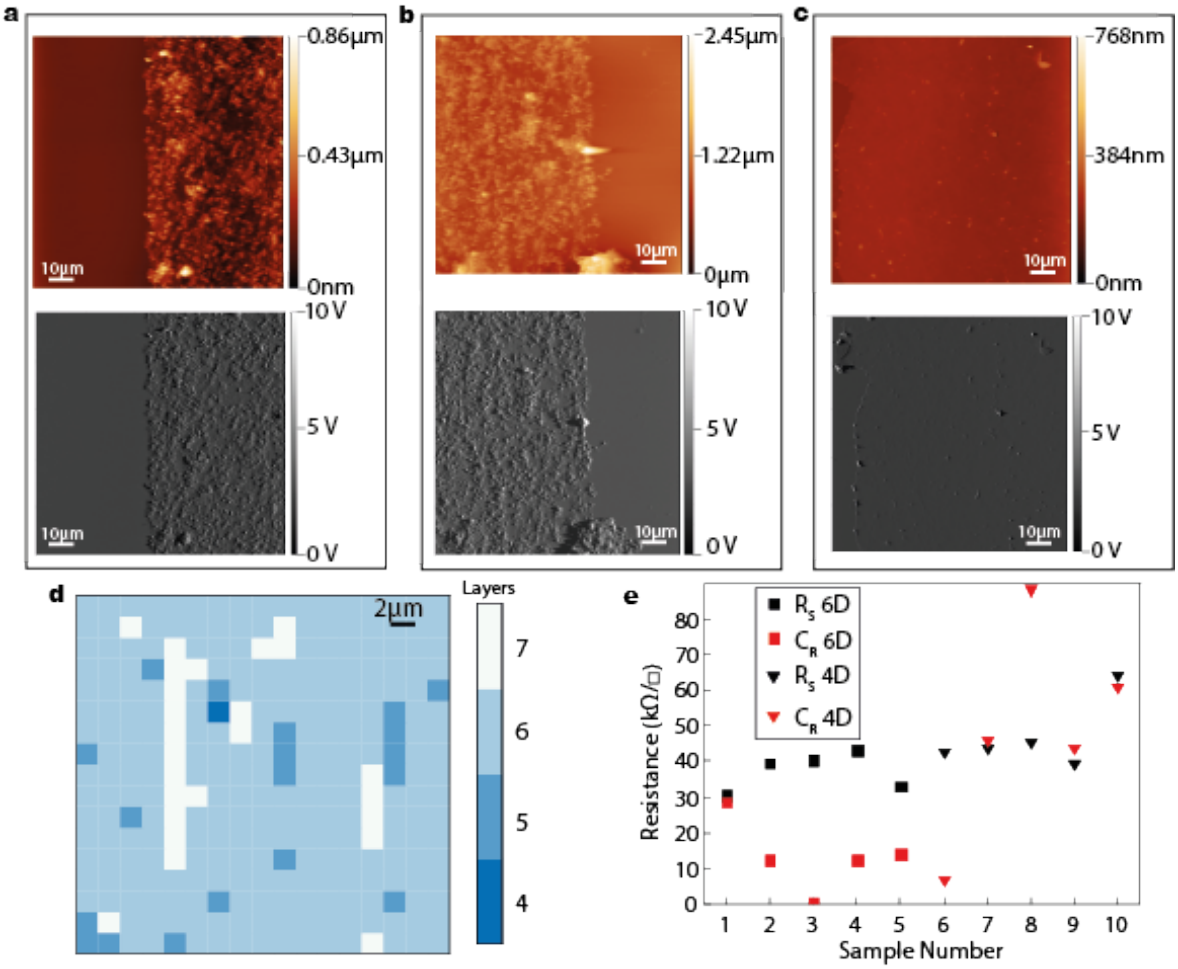

Figure 7.3: a) AFM topographic signal (top panel) and lateral signal (bottom panel) of a 4D line of LEG. b)AFM topographic signal (top panel) and lateral signal (bottom panel) of a 6D line of LEG. c) AFM topographic signal (top panel) and lateral signal (bottom panel) of a 4D film of GO. d) Raman map of a 6D line, with the number of layers. e) Electrical measurements showing sheet and contact resistance.

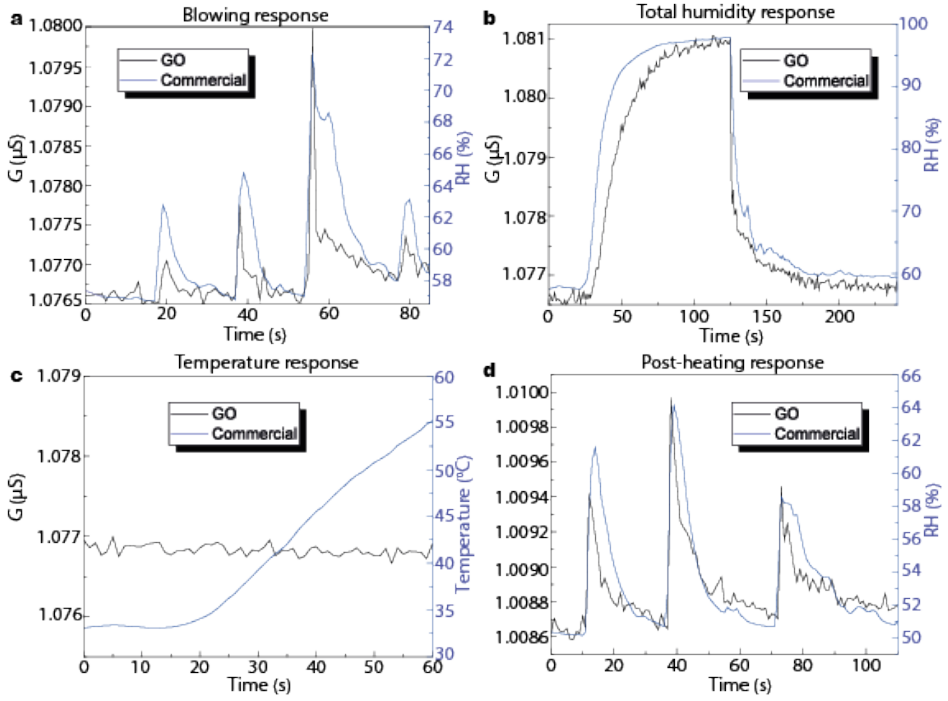

Figure 7.4: a) Device response to human exhaled respiration. b) Device response to a large change in humidity. c) Device response to a change in temperature. c) Device response after an annealing step.

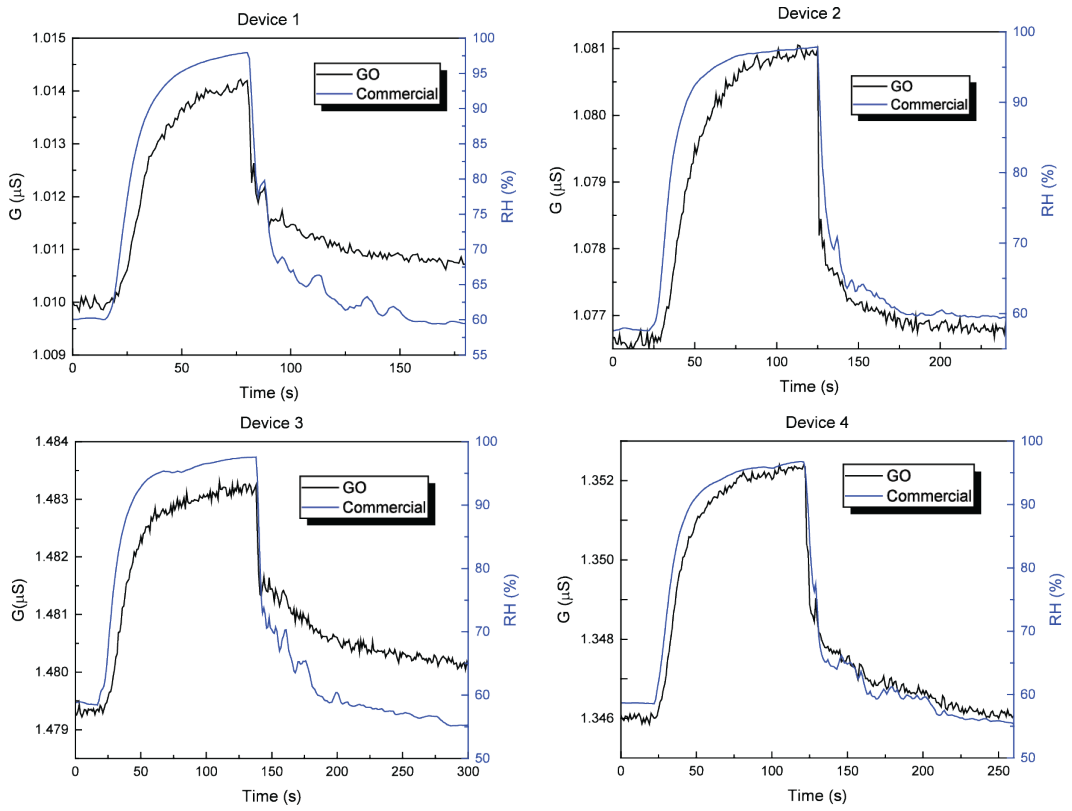

Figure 7.5: Performance of the 4 different devices built on Si/SiO_2 chips under high humidity conditions. Device 1 and Device 2 were built in a different chip than Device 3 and Device 4. Devices 1 and 2, and Devices 3 and 4 were built in the same chip.

would in fact reduce its sensing properties. To assess this, we evaluated the response of the device after heating up to 80 ^oC for 5 minutes; this, as shown in the Figure 7.4d, remains unaltered.

The reproducibility of the process is also assessed comparing four different devices, two processed on the same chip and two processed on a different chip. Their response to high humidity (Figure 7.5) and blowing (Figure 7.6) is found to be very similar, confirming the reliability of the technique for batch processing.

It is known that GO slowly changes properties when is not maintained within an inert atmosphere. To evaluate this effect, the devices were subsequently measured after being stored within normal ambient conditions from two days up to 90 days after the first measurement, three times longer previous reports.[16] As seen in the Figure 7.7, the

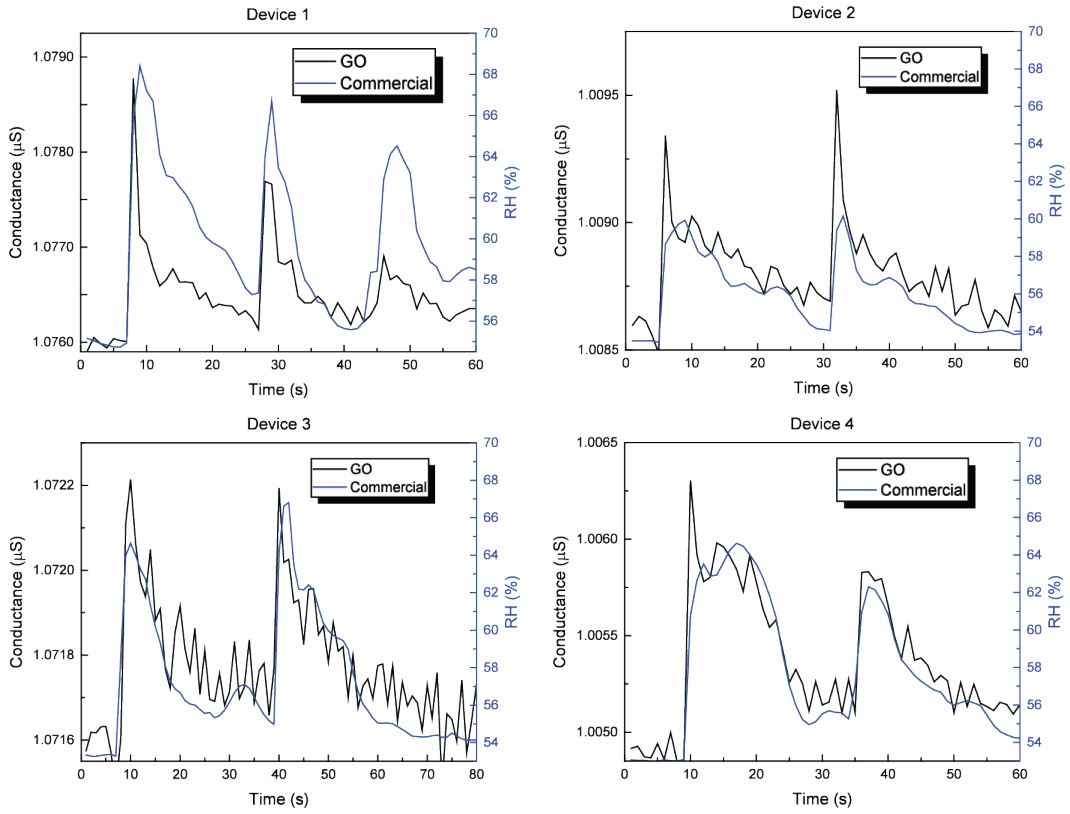

Figure 7.6: Performance of the 4 different devices built on Si/SiO_2 chips under human blowing conditions. Device 1 and Device 2 were built in a different chip than Device 3 and Device 4. Devices 1 and 2, and Devices 3 and 4 were built in the same chip.

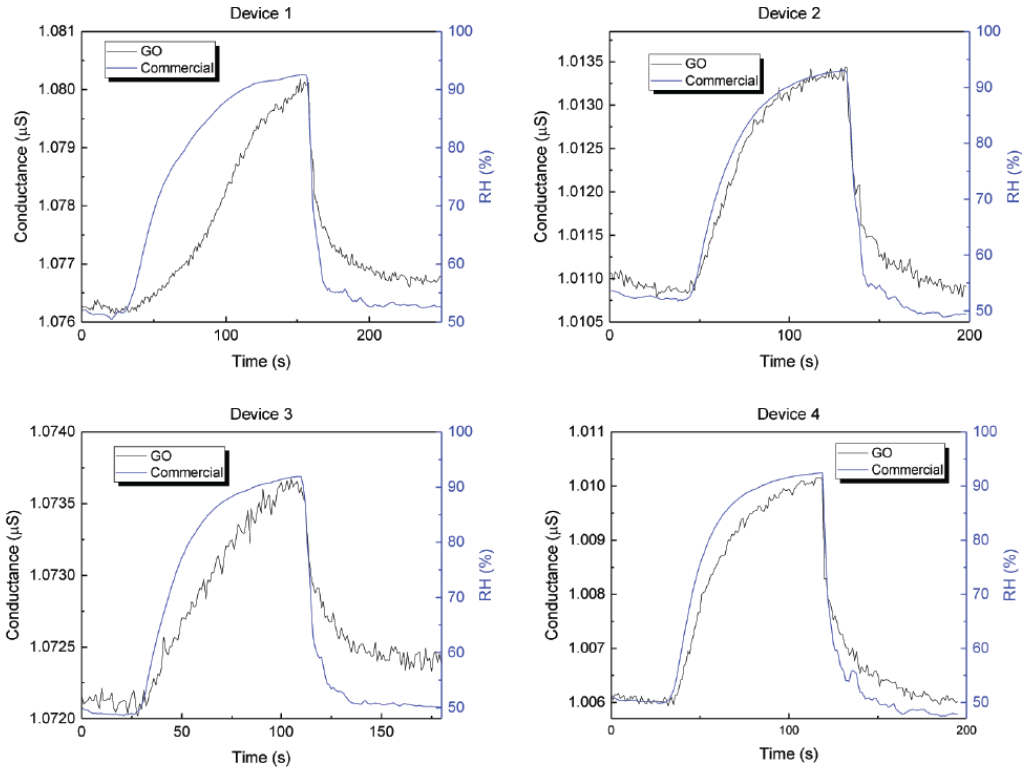

Figure 7.7: Performance of the 4 different devices built on Si/SiO_2 chips after 90 days of storage in ambient conditions. Device 1 and Device 2 were built in a different chip than Device 3 and Device 4. Devices 1 and 2, and Devices 3 and 4 were built in the same chip.

device is still responsive.

It was mentioned before that for the successful incorporation of the 2D materials into the electronic factories and foundries, the workflows need to be adapted to their requirements. All the processes carried out so far are compatible or have potential to be introduced into a CMOS back-end production line (BEPL). For this, we processed a 4' Si/SiO_2 wafer where we created devices of 1 cm^2 as shown in the Figure 7.8a. A typical device response from a device is shown in Figure 7.8b; the difference in time response can be again attributed to different position of the two different sensors. Contacts were made with 100 nm thick Al layer, since Au is not suitable for CMOS due to introduction of mid-gap states in Si.

Furthermore, due to the low-temperature processing, sensors on PET substrates

were successfully built, which have great transparency and flexibility as shown in the Figure 7.8c and the Figure 7.8d. In the Figure 7.8c, 1 cm^2 devices were created and contacted with commercial carbon paste, creating all-carbon based humidity sensors; in Figure 7.8d we created fully functional devices with a footprint of just 25 mm^2, contacted with a thin wetting layer of Cr (5 nm) and thick layer (100 nm) of Au. The performance of these devices before and after 2000 bendings (5 mm radius) is shown in Figure 7.8e; it remains identical, demonstrating the good mechanical properties of the devices.

7.5 CONCLUSIONS

In conclusion, we present here a novel combination of techniques that allowed to create patterns and accurately deposit solution-processed 2D materials such as LEG and GO, over a large area with high-resolution. Remarkably, after parameter optimization, this process should be compatible with any type of 2D materials, opening in up ways to construct functional yet cheap flexible electronics with these materials. This technique was used to create all-carbon humidity sensors; their performance correlates very well with that of a commercially available sensor.

Furthermore, the scalability of this process is demonstrated creating a whole 4' Si/SiO_2 wafer, in synergy with CMOS processes; we also employed this method to create all-carbon flexible, transparent devices on PET substrate, which are resilient to intense mechanical stresses. This technique may become a cornerstone when integrating solution-processed 2D materials into real-life electronic applications in the future.

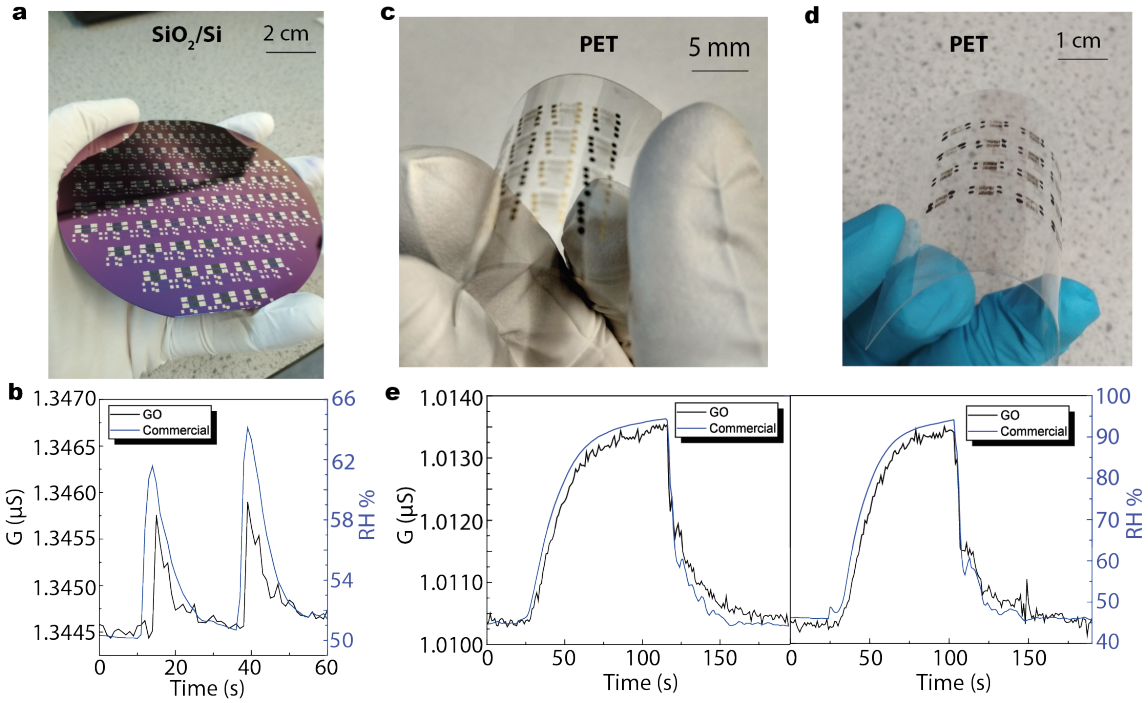

Figure 7.8: a) A processed 4' Si/SiO_2 wafer. b) Performance of a representative device processed on the 4' wafer. c) Devices processed on PET substrates and Au contacts. d) Devices processed on PET with carbon paste contacts. e) Device performance before (left panel) and after (right panel) 2000 bendings. The device bent was the one shown in c).

BIBLIOGRAPHY

[1] F. Schedin et al. Detection of individual gas molecules adsorbed on graphene. *Nature Materials*, 6, 2007.

[2] H. J. Yoon et al. Carbon dioxide gas sensor using a graphene sheet. *Sensors and Actuators B: Chemical*, 157, 2011.

[3] Y. Dan et al. Intrinsic response of graphene vapor sensors. *Nano Letters*, 9, 2009.

[4] T. Mueller et al. Graphene photodetectors for high-speed optical communications. *Nature Photonics*, 4, 2010.

[5] F. Xia et al. Ultrafast graphene photodetector. *Nature Nanotechnology*, 4, 2009.

[6] X. Gan et al. Chip-integrated ultrafast graphene photodetector with high responsivity. *Nature Photonics*, 7, 2013.

[7] E. W. E. W. Hill et al. Graphene sensors. *IEEE Sensors Journal*, 11, 2011.

[8] D. J. Late et al. Single-layer $MoSe_2$ based NH_3 gas sensor. *Applied Physics Letters*, 105, 2014.

[9] G. Huayang et al. Transparent, flexible, and stretchable WS_2 based humidity sensors for electronic skin. *Nanoscale*, 9, 2017.

[10] A. Shadman et al. Monolayer MoS_2 and WSe_2 double gate field effect transistor as super nernst pH sensor and nanobiosensor. *Sensing and Bio-Sensing Research*, 11, 2016.

[11] M-Y. Tsai et al. Flexible MoS_2 field-effect transistors for gate-tunable piezoresistive strain sensors. *ACS Applied Materials & Interfaces*, 7, 2015.

[12] D. Kufer et al. Highly sensitive, encapsulated MoS_2 photodetector with gate controllable gain and speed. *Nano Letters*, 15, 2015.

[13] J. T. Robinson et al. Reduced graphene oxide molecular sensors. *Nano Letters*, 8, 2008.

[14] G. Lu et al. Reduced graphene oxide for room-temperature gas sensors. *Nanotechnology*, 20, 2009.

[15] S. Borini et al. Ultrafast graphene oxide humidity sensors. *ACS Nano*, 7, 2013.

[16] H. Bi et al. Ultrahigh humidity sensitivity of graphene oxide. *Scientific Reports*, 2013, 2013.

[17] K. R.and others Paton. Scalable production of large quantities of defect-free few-layer graphene by shear exfoliation in liquids. *Nature Materials*, 13, 2014.

[18] F. Bonaccorso et al. Production and processing of graphene and 2d crystals. *Materials Today*, 15, 2012.

[19] J. N. Coleman et al. Two-dimensional nanosheets produced by liquid exfoliation of layered materials. *Science*, 331, 2011.

[20] Y. Wei et al. Liquid-phase exfoliation of graphite for mass production of pristine few-layer graphene. *Current Opinion in Colloid and Interface Science*, 20, 2015.

[21] V. Nicolosi et al. Liquid exfoliation of layered materials. *Science*, 340, 2013.

[22] World Health Organization. Guidelines on the international packaging and shipping of vaccines. 2005.

[23] F. Withers et al. Heterostructures produced from nanosheet-based inks. *Nano Letters*, 14, 2014.

[24] D. McManus et al. Water-based and biocompatible 2d crystal inks for all-inkjet-printed heterostructures. *Nature Nanotechnology*, 12, 2017.

[25] K-Y. Shin et al. Micropatterning of graphene sheets by inkjet printing and its wideband dipole-antenna application. *Advanced Materials*, 23, 2011.

[26] F. Torrisi et al. Inkjet-printed graphene electronics. *ACS Nano*, 6, 2012.

[27] L. Jiantong et al. Inkjet printing of 2d layered materials. *Chem. Phys. Chem.*, 15, 2014.

[28] L. Jiantong et al. Efficient inkjet printing of graphene. *Advanced Materials*, 25, 2013.

[29] A. Kamyshny et al. Conductive nanomaterials for printed electronics. *Small*, 10, 2014.

[30] E. B. Secor et al. Emerging carbon and post-carbon nanomaterial inks for printed electronics. *The Journal of Physical Chemistry Letters*, 6, 2015.

[31] D. J. Finn et al. Inkjet deposition of liquid-exfoliated graphene and mos2 nanosheets for printed device applications. *J. Mater. Chem. C*, 2, 2014.

[32] F. Withers et al. Light-emitting diodes by band-structure engineering in van der waals heterostructures. *Nature Materials*, 14, 2015.

[33] J. D. Mehew et al. Fast and highly sensitive ionic-polymer-gated ws2–graphene photodetectors. *Advanced Materials*, 29, 2017.

[34] A. Agmon. The grotthuss mechanism. *Chemical Physics Letters*, 244, 1995.

8

CONCLUSIONS

This thesis has presented methods to integrate two dimensional (2D) materials into workflows compatible with large-scale, mass-production processing. These methods have been characterise, and employed, to create several devices with real-life, consumer applications and usages.

In Chapter 4 the intercalation with iron chloride (III) ($FeCl_3$) has been shown as an effective and scalable technique to reduce the resistance of few-layer graphene (FLG). Achieving specifications which rival those of indium tin oxide (ITO) and surpass those of other flexible transparent conductive film (TCF), we used this iron-chloride intercalated few-layer graphene ($FeCl_3$-FLG) electrodes to build alternating-current electroluminescence (ACEL) and demonstrated a superior performance over pristine single-layer graphene (SLG), FLG and poly(3,4-ethylenedioxythiophene) polystyrene-sulfonate (PEDOT:PSS). Moreover, these devices where fully flexible and capable of sustaining large strains. The processing of these devices was straightforward and compatible with roll-to-roll (R2R) techniques. These findings would enable larger and more efficient ACEL screens and displays to be built.

In Chapter 5, building upon the previous work, ACEL devices on textile fibres were created using FLG TCF. Despite the fibre roughness which would virtually preclude any modern electronic device to be built, the fibres became conductive with the usage of FLG. This, together with the ACEL technology, enabled me to fabricate light-emitting devices that were truly embedded in the fibre. Two different processes for creating textile light-emitting arrays where demonstrated. These results would allow light-emitting devices to be embedded in clothes and other textiles, using established technologies for flexible light-illumination.

In Chapter 6, graphene-coated conductive fibres were employed to create touch-sensors. Implementing resistive and capacitive detection schemes, fully functional transparent and flexible devices were created, spanning from finger-like devices to position-sensitive arrays. A novel scheme for patterning and deposition which would enable these devices to be created by R2R processing is demonstrated. Moreover, by utilizing different graphene growth methods, from chemical vapour deposition (CVD)-grown to liquid-phase exfoliation (LPE), the functionality of such devices was tailored to meet the desired specifications. Immediate uses for these devices would be healthcare and military.

In Chapter 7, a novel processing technique was presented and used, together with LPE of 2D materials, to create wafer-scale patterns solely with solutions of liquid-exfoliated graphene (LEG) and graphene oxide (GO). All-carbon humidity sensors were created on flexible and transparent polyethylene terephthalate (PET) substrates and 4' SiO_2/Si wafers; this process is compatible with R2R and complementary metal oxide semiconductor (CMOS) processing. Due to the inherent scalability of the materials and processing, these results pave the way for solution-processed, low cost electronics built with 2D materials at the large scale.

9

FUTURE WORK

In this work, novel approaches and techniques to develop graphene-based devices and applications have been presented. The development of new methods of production and processing of two dimensional (2D) materials according to and compatible with industrial processes will surely keep happening. I forecast that the largest development of new technologies will occur regarding liquid exfoliation of materials, at least in the short span of time.

I had initiated a novel project right before I left which is being continued by people within the group. This project involves different areas of my expertise and is directly related with the work presented here. It takes advantage of the novel deposition and processing techniques introduced, specially regarding liquid-exfoliated graphene (LEG) on textile fibres, and the good sensing properties of graphene oxide (GO). The idea is to build humidity sensors on fibres, in the same way that they have been built in Chapter 7, using the processing explained in Chapter 6 and 7. The manufacture of these devices should be straightforward, low-cost and compatible with roll-to-roll (R2R) processes; they would have a profound impact in wearable technology and healthcare, where monitoring humidity plays a key role in drug delivery and sanitary conditions.

But not only. As mentioned, the vast range of materials available for exfoliation and their range of properties allow for many different electronic devices to be built in these textile fibres such as diodes and photodetectors, FETs and Tunnel Transistors, etc. This is a very promising research line. The combination of these basic electronic building blocks would expand the functionality of wearable devices. That this is a very interesting and promising research topic, and that the 2D materials community will see some great advances in this area.

BIBLIOGRAPHY

PUBLICATIONS

The ideas and data presented in this thesis are subject of the following publications:

- Homogeneously Bright, Flexible, and Foldable Lighting Devices with Functionalized Graphene Electrodes. E. Torres Alonso, G. Karkera, G. F. Jones, M. Craciun and S. Russo. ACS Appl. Mater. Interfaces, 2016.

- Towards Conductive Textiles: Coating Polymeric Fibres with Graphene. Ana I. S. Neves, Daniela P. Rodrigues, Adolfo de Sanctis, E. Torres Alonso, M. S. Pereira, V. S. Amaral, L. V. Melo, S. Russo, I. de Schrijver, H. Alves and M. Craciun. Scientific Reports, 2017.

- Fast and Highly Sensitive Ionic-Polymer-Gated WS_2-Graphene Photodetectors. J. D. Mehew, S. Unal, E. Torres Alonso, G. F. Jones, S. F. Ramadhan, M. F. Craciun and S. Russo. Advanced Materials, 2017.

- 2D Materials Integrated in Si_3N_4 Photonics Platform. J. Faneca, B.T. Hogan, E. Torres Alonso, M. Craciun and A. Baldycheva. SPIE Proceedings. 2018.

- Wafer-scale Integration of Water-based 2D Inks for All-carbon Humidity Sensors. E. Torres Alonso, S. Dong-Wook, S. Russo and M. Craciun. Submitted to Nature Communications.

- Graphene-based Light-emitting Devices and Touch-sensors on Textile Fibres. E. Torres Alonso, D. P. Rodrigues, M. Khetani, D-W. Shin, A. De Sanctis, H. Joulie, I. de Schrijver, A. Baldycheva, H. Alves, A. I. S. Neves, S. Russo and M. Craciun. Submitted to Advanced Materials.

- $FeCl_3$ Intercalated Few-layer Graphene For Terahertz Time-domain Spectroscopy Applications. M. Zhukova, Y. Grachev, A. Tcypkin, E. Kovalska, E. Torres Alonso, S. Russo, M. Craciun, A. Baldycheva and V. Bespalov. IEEE Proceedings 43^{rd} International Conference on Infrared, Millimeter, and Terahertz Waves. 2018.